

EDITORIAL

Is independent Interventional Radiology the future? (p. 69-71)

IN-DEPTH REVIEW

Artificial intelligence in radiology (p. 72-81)

FULL RESEARCH ARTICLES

Elastographic patterns of thyroid microcarcinomas:
a new proposal (p. 82-92)

Imaging and clinical features of breast cancer in young Mexican women:
long delay between self-detection and seeking medical attention (p. 93-104)

Coronary artery anomalies and normal anatomic variants in coronary computed
tomography angiography (CCTA): a pictorial essay (p. 105-114)

BRIEF RESEARCH ARTICLES

Intraobserver and interobserver agreement of US findings in suspected
lymph node metastasis in papillary thyroid carcinoma (p. 115-121)

Interobserver agreement between radiologists and artificial intelligence
in mammographic breast density classification (p. 122-127)

CASE REPORT

Fallopian tube decidualis with massive hemoperitoneum in a second-trimester
pregnancy: a case report of ultrasound findings (p. 128-131)

IMAGES IN RADIOLOGY

The transmante sign: a characteristic MRI finding
of focal cortical dysplasia type II (p. 132-133)



PERMANER
www.permayer.com

Official Journal of the



FEDERACIÓN MEXICANA DE RADIOLOGÍA E IMAGEN, A.C

A simple step to digital radiography



i550z

Digital Radiography Systems



+52 686-568-1904
WhatsApp - +520686-606-4076
www.laicoinfo.com
Mexicali, BC Mexico

The Synergy of Innovation and Health Imaging Solutions
Designed to help you see what matters most



DDR
DYNAMIC DIGITAL RADIOGRAPHY

Dynamic Digital Radiology (DDR) enables clinicians to observe the dynamic motion of anatomical structures over time, enhancing diagnostic capabilities. **DDR provides a view of anatomy in motion, with a large field of view and low radiation dose.**

DDR is a promising platform for AI (Artificial Intelligence) applications. DDR is not fluoroscopy;

DDR is X-ray that Moves!



xraythatmoves.com

exa

Scalable and customizable to the exact requirements of your practice, our leading IT solutions manage medical imaging and patient data right across the healthcare spectrum, including PACS, RIS, specialty viewers and Billing.

Our Healthcare IT software solutions are packed with the all the speed, security and flexibility you need, anytime/anywhere viewing and a single integrated database across all modules.



KONICA MINOLTA

contact us: kmhalatinoamerica@konicaminolta.com

Learn more about our solutions with Workflow Solutions, Insights and Consulting



Visit <https://radiologia.bayer.com/es> or contact your sales advisor

Clear Direction From Diagnosis to Care

PP-WS-MX-0005-1

MyLab™ OMEGAeXP

Advanced Imaging in Motion



esaote
esaote.com

MedRent
medrent.mx

Carestream

Meet the
NEW
member
of the family

DRX-Rise

It's amazing!



We have **EQUIPMENT** for all **YOUR NEEDS**



Right for **Today...** *Ready for Tomorrow.*



Scan the QR
and visit
the Virtual Hospital





Journal of the Mexican Federation of Radiology and Imaging

J Mex Fed Radiol Imaging

Volume 3. Number 2, April-June 2024

ISSN: 2938-1215

eISSN: 2696-8444

The *Journal of the Mexican Federation of Radiology and Imaging* (JMEXFRI) is the official journal of the Federación Mexicana de Radiología e Imagen. The aim of the journal is to disseminate scientific knowledge and technological developments for innovation in diagnostic and therapeutic radiology with original articles on basic and clinical aspects of modern radiology in an international context with global impact. JMEXFRI is published in American English with 4 issues per year (print and online) and the first issue was published in the first quarter of 2022. Articles undergo a rigorous, double-blind peer-review process. Publication of articles in JMEXFRI is free of charge and all published articles are open access.

The journal publishes the following types of manuscripts: *Full Research Article, Pictorial Essay, Brief Research Article, Technical Note, In-Depth Review, Case Report, Images in Radiology, and Editorial.*

EDITORIAL BOARD

EDITOR-IN-CHIEF

Mauricio Figueroa-Sanchez, M.D.

Department of Radiology, Antiguo Hospital Civil de Guadalajara "Fray Antonio Alcalde", Guadalajara, Jal., Mexico

ASSOCIATE EDITORS

Gerardo E. Ornelas-Cortinas, M.D.

Centro Universitario de Imagen Diagnostica, Hospital Universitario "Dr. Jose E. Gonzalez", Monterrey, N.L., Mexico

Araceli Cue-Castro, M.D.

Department of Computed Tomography, Hospital General "Dr. Enrique Cabrera" SEDESA, Mexico City, Mexico

Oscar A. Chavez-Barba, M.D.

Department of Radiology, Antiguo Hospital Civil de Guadalajara "Fray Antonio Alcalde", Guadalajara, Jal., Mexico

Ana M. Contreras-Navarro, M.D., M.Sc., Ph.D.

Scientific Writing Workshop, JMEXFRI, Zapopan, Jal., Mexico

David Garza-Cruz, M.D.

Department of Radiology, Hospital Angeles, Torreon, Coah., Mexico

J. Mario Bernal-Ramirez, M.D.

Department of Medical Clinics, Centro Universitario de Ciencias de la Salud, Universidad de Guadalajara, Guadalajara, Jal., Mexico

SCIENTIFIC TRANSLATOR EDITOR

Sergio Lozano-Rodriguez, M.D.

Research Office of the Vice Dean, Hospital Universitario "Dr. Jose E. Gonzalez", Monterrey, N.L., Mexico

BIOSTATISTICS ADVISER

Cesar N. Cristancho-Rojas, M.D., M.Sc.

School of Public Health, Oregon Health & Science University, Portland, OR., USA

DESIGN ADVISER

Jorge Mendez-Palacios, B.Sc.

Design Area, JMEXFRI. Zapopan, Jal., Mexico

NATIONAL EDITORIAL BOARD

HEAD AND NECK RADIOLOGY

Mario A. Campos-Coy, M.D.

*Centro Universitario de Imagen Diagnostica,
Hospital Universitario "Dr. Jose E. Gonzalez",
Monterrey, N.L., Mexico*

Eduardo D. Sarda-Inman, M.D.

*Diagnostico Especializado por Imagen,
Zapopan, Jal., Mexico*

GASTROINTESTINAL RADIOLOGY

Araceli Cue-Castro, M.D.

*Department of Computed Tomography,
Hospital General "Dr. Enrique Cabrera" SEDESA,
Mexico City, Mexico*

Adrian Negreros-Osuna, M.D., Ph.D.

*Departamento de Radiología,
Hospital Regional ISSSTE Monterrey,
Monterrey, N.L., Mexico*

Oscar A. Chavez-Barba, M.D.

*Department of Radiology,
Antiguo Hospital Civil de Guadalajara
"Fray Antonio Alcalde",
Guadalajara, Jal., Mexico*

OBSTETRIC AND GYNECOLOGIC RADIOLOGY

Dante R. Casale-Menier, M.D.

*Department of Radiology and Imaging,
Hospital Angeles,
Ciudad Juarez, Chih., Mexico*

Roberto J. Carrales-Cuellar, M.D.

*Department of Ecographic Diagnosis,
Radiología Especializada,
Guadalajara, Jal., Mexico*

BREAST RADIOLOGY

David F. Perez-Montemayor, M.D.

*General Direction,
Centro de Imagenología Integral IMAX,
Tampico, Tamps., Mexico*

Beatriz Gonzalez-Ulloa, M.D.

*Department of Breast Imaging,
Diagnostico Especializado por Imagen,
Guadalajara, Jal., Mexico*

Margarita L. Garza-Montemayor, M.D.

*Departamento de Imagen Diagnostica,
Centro de Cancer de Mama,
Hospital Zambrano Hellion, Tec Salud,
Monterrey, N.L., Mexico*

Karla M. Nuñez-Barragan, M.D.

*Women's Imaging Department,
Doctors Hospital East Auna
Monterrey, N. L., Mexico*

NUCLEAR AND MOLECULAR MEDICINE

Hugo E. Solis-Lara, M.D.

*Centro de Imagen Molecular,
Hospital Christus Muguerza Alta Especialidad,
Monterrey, N.L., Mexico*

NEURORADIOLOGY

Jorge Paz-Gutierrez, M.D.

*Department of Magnetic Resonance,
Centro Medico Puerta de Hierro,
Zapopan, Jal., Mexico*

Azalea Garza-Baez, M.D.

*Department of Radiology and Imaging,
Hospital Zambrano Hellion,
Tecnologico de Monterrey,
Monterrey, N.L., Mexico*

Perla M. Salgado-Lujambio, M.D.

*Direccion de Enseñanza,
Instituto Nacional de Neurología y
Neurocirugía "Manuel Velasco Suarez"
Mexico City, Mexico*

PEDIATRIC RADIOLOGY

Aida Perez-Lara, M.D.

*Department of Radiology, Hospital Español,
Mexico City, Mexico*

MUSCULOSKELETAL RADIOLOGY

Oscar A. Chavez-Barba, M.D.

*Department of Radiology, Antiguo Hospital Civil
de Guadalajara "Fray Antonio Alcalde",
Guadalajara, Jal., Mexico*

J. Francisco Diaz-Fernandez, M.D.

*Department of Radiology,
Hospital General "Agustin O'Horan",
Merida, Yuc., Mexico*

CHEST AND CARDIOVASCULAR RADIOLOGY

Sergio A. Criales-Vera, M.D.

*Department of Radiology and Imaging,
Instituto Nacional de Cardiología "Ignacio Chavez",
Mexico City, Mexico*

Harold Goerne, M.D.

*Department of Radiology, Hospital de Pediatría,
Instituto Mexicano del Seguro Social,
Guadalajara, Jal., Mexico*

Luis F. Alva-Lopez, M.D.

*Department of Radiology, Hospital Medica Sur,
Mexico City, Mexico*

GENITOURINARY RADIOLOGY

Sergio B. Peregrina-Gonzalez, M.D.

*Consultorio de Imagen,
Guadalajara, Jal., Mexico*

Araceli Cue-Castro, M.D.

*Department of Computed Tomography,
Hospital General "Dr. Enrique Cabrera" SEDESA,
Mexico City, Mexico*

Adrian Negreros-Osuna, M.D.

*Departamento de Radiología,
Hospital Regional ISSSTE Monterrey,
Monterrey, N.L., Mexico*

Benjamin Conde-Castro, M.D.

*Faculty of Medicine,
Universidad Nacional Autónoma de Mexico,
Mexico City, Mexico*

ULTRASOUND

Rosa M. Alanis-Salazar, M.D.

*Departamento de Radiología, UMF Guadalupe, ISSSTE,
Monterrey, NL., Mexico*

Victor M. Rodriguez-Peralta, M.D.

*Department of Radiology,
Fundacion de Cancer de Mama (FUCAM),
Oaxaca, Oax., Mexico*

David Garza-Cruz, M.D.

*Department of Radiology, Hospital Angeles,
Torreon, Coah., Mexico*

Manuel Hernandez-Cruz, M.D.

*Area de Ultrasonido,
Unidad de Ultrasonido Diagnostico,
Puebla, Pue. Mexico*

VASCULAR AND INTERVENTIONAL RADIOLOGY

Guillermo Elizondo-Riojas, M.D., Ph.D.

*Centro Universitario de Imagen Diagnostica,
Hospital Universitario "Dr. Jose E. Gonzalez",
Monterrey, N.L., Mexico*

Raul A. De Luna-Vega. M.D.

*Centro Universitario de Imagen Diagnostica,
Hospital Universitario "Dr. Jose E. Gonzalez",
Monterrey, N.L., Mexico*

ARTIFICIAL INTELLIGENCE

Guillermo Elizondo-Riojas, M.D., Ph.D.

*Centro Universitario de Imagen Diagnostica,
Hospital Universitario "Dr. Jose E. Gonzalez",
Monterrey, N.L., Mexico*

Adrian Negreros-Osuna, M.D.

*Departamento de Radiología,
Hospital Regional ISSSTE Monterrey,
Monterrey, N.L., Mexico*

J. Mario Bernal-Ramirez, M.D.

*Department of Medical Clinics,
Centro Universitario de Ciencias de la Salud,
Universidad de Guadalajara,
Guadalajara, Jal., Mexico*

Benjamin Conde-Castro, M.D.

*Faculty of Medicine,
Universidad Nacional Autónoma de México,
Mexico City, Mexico*

JUNIOR EDITORIAL BOARD

J. Mario Bernal-Ramirez, M.D.

*Department of Medical Clinics,
Centro Universitario de Ciencias de la Salud,
Universidad de Guadalajara,
Guadalajara, Jal., Mexico*

Ana K. Luna-Marroquin, M.D.

*Centro Universitario de Imagen Diagnostica,
Hospital Universitario "Dr. Jose E. Gonzalez",
Monterrey, N.L., Mexico*

M. Lourdes Garcia-Colmenero, M.D.

*Departamento de Radiología,
CID Centro de Imagen y Diagnostico
Guadalajara, Jal., Mexico*

Xavier A. Gonzalez-Ballesteros, M.D.

*Departamento de Radiología,
Hospital San Angel Inn Universidad,
Ciudad de Mexico, Mexico*

Adriana Parada-Gallardo, M.D.

*Department of Radiology,
Hospital General de Zapopan,
Zapopan, Jal., Mexico*

INTERNATIONAL EDITORIAL BOARD

HEAD AND NECK RADIOLOGY

Richard H. Wiggins, M.D.

*Department of Radiology and Imaging Sciences, School
of Medicine, University of Utah,
Salt Lake City, UT., USA*

Amy Juliano, M.D.

*Department of Radiology,
Massachusetts Eye and Ear,
Harvard Medical School,
Boston, MA., USA*

GASTROINTESTINAL RADIOLOGY

Jorge A. Soto, M.D.

*Department of Radiology, Boston Medical Center,
Boston, MA., USA*

Jorge Elias Jr. Ph.D.

*Departamento de Imagenes Medicas,
Oncologia e Hematologia,
Faculdade de Medicina Ribeirao Preto,
Universidade Sao Paulo Ribeirao Preto,
Sao Paulo, Brazil*

Valdair F. Muglia, M.D.

*Faculdade de Medicina de Ribeirão Preto,
Universidade de São Paulo, Ribeirão Preto,
Sao Paulo, Brazil*

Carlo Catalano, M.D.

*Department of Diagnostic Radiology
La Sapienza University of Rome
Rome, Italy*

OBSTETRIC AND GYNECOLOGIC RADIOLOGY

Luciana Pardini Chamie, M.D., Ph.D.

*Centro de Diagnostico Ultrasonografico
Especializado en Imagen de la Mujer,
Sao Paulo, Brazil*

BREAST RADIOLOGY

Javier Romero-Enciso, M.D.

*Department of Radiology,
Fundacion Santa Fe,
Bogota, Colombia*

NUCLEAR AND MOLECULAR MEDICINE

Begoña Martinez-Sanchis, M.D.

*Department of Nuclear Medicine,
Hospital Universitario y Politecnico La Fe,
Valencia, Spain*

Cesar N. Cristancho-Rojas, M.D., M.Sc.

*School of Public Health,
Oregon Health & Science University,
Portland, OR., USA*

NEURORADIOLOGY

Roy F. Riascos-Castaneda, M.D.

*Department of Radiology and Neurosurgery,
Memorial Hermann Hospital System,
Houston, TX., USA*

Rafael Rojas-Jasso, M.D.

*Department of Radiology, Beth Israel,
Deaconess Medical Center,
Boston, MA., USA*

Henrique Carrete Jr., M.D., Ph.D.

*Department of Diagnostic Imaging,
Universidade de Sao Paulo,
Sao Paulo, Brazil*

Carlos Torres, M.D.

*Department of Diagnostic Imaging,
The Ottawa Hospital,
Ottawa, Canada*

MUSCULOSKELETAL RADIOLOGY

Javier Fernandez-Jara, M.D.

*Department of Radiology,
Hospital Universitario Sanitas La Zarzuela,
Madrid, Spain*

Jose Luis del Cura, M.D.

*Radiodiagnosis Service,
Hospital Universitario Donostia,
San Sebastian-Donostia, Spain*

Diego F. Lemos, M.D.

*Department of Radiology,
University of Vermont Medical Center,
Burlington, VT, USA*

PEDIATRIC RADIOLOGY

George Bisset, M.D.

*Department of Radiology, Children's Hospital
Pennsylvania, PA., USA*

Sara Reis Teixeira, M.D., Ph.D.

*Department of Radiology, Children's Hospital
Pennsylvania, PA. USA*

CHEST AND CARDIOVASCULAR RADIOLOGY

Fernando R. Gutierrez, M.D.

*Department of Radiology and Cardiothoracic Imaging,
The Mallinckrodt Institute of Radiology,
St. Louis, MO., USA*

Jorge Carrillo-Bayona, M.D.

*Department of Radiology,
Hospital Universitario Mayor,
Bogota, Colombia*

Carlos S. Restrepo, M.D.

*Department of Cardiothoracic Radiology,
Texas University,
San Antonio, TX., USA*

Sebastian Rossini, M.D.

*Department of Radiology,
Instituto Radiologico Mater Dei,
Buenos Aires, Argentina*

Santiago Martinez-Jimenez, M.D.

*Department of Radiology,
Saint Luke's Hospital of Kansas City,
Kansas City, KS., USA*

L. Antonio Sosa-Lozano, M.D.

*Department of Cardiothoracic Radiology,
Medical College of Wisconsin,
Milwaukee, WI., USA*

GENITOURINARY RADIOLOGY

Daniela Stoisa, M.D.

*Department of Radiology, Diagnostico Medico Oroño,
Rosario, Santa Fe, Argentina*

Valdair F. Muglia, M.D.

*Faculdade de Medicina de Ribeirao Preto,
Universidade de Sao Paulo Ribeirao Preto,
Sao Paulo, Brazil*

ULTRASOUND

Edward G. Grant, M.D.

*Department of Radiology, USC Norris Cancer Center,
Los Angeles, CA., USA*

Juan P. Niedmann-Espinosa, M.D.

*Department of Ecotomography,
Clinica Alemana de Santiago,
Santiago de Chile, Chile*

VASCULAR AND INTERVENTIONAL RADIOLOGY

Manuel Cifrian-Perez, M.D., Ph.D.

*Imaging Clinic Department,
Hospital Universitario y Politecnico La Fe,
Valencia, Spain*

ARTIFICIAL INTELLIGENCE

Leonor Cerda-Alberich, Ph.D

*Imaging Clinic Department,
Hospital Universitario y Politecnico La Fe,
Valencia, Spain*

Felipe Campos Kitamura, M.D., Ph.D.

*Dasalnova, Dasa,
Sao Paulo, Brazil*

GRAPHICAL ABSTRACTS COMMITTEE

Oscar A. Chavez-Barba, M.D.

*Department of Radiology,
Antiguo Hospital Civil de Guadalajara
"Fray Antonio Alcalde",
Guadalajara, Jal., Mexico*

Adriana Parada-Gallardo, M.D.

*Department of Radiology,
Hospital General de Zapopan,
Zapopan, Jal., Mexico*

J.M. Ignacio Lopez-Mendez, M.D.

*Department of Radiology and Imaging,
Hospital de Especialidades, CMNO
Instituto Mexicano del Seguro Social,
Guadalajara, Jal., Mexico.*

Juan Pablo Lopez-Gutierrez, M.D.

*Department of Radiology and Imaging,
Hospital General de Zona 3,
Instituto Mexicano del Seguro Social
Aguascalientes, Ags., Mexico*

Gerardo Llamas-Linares, M.D.

*Centro Universitario de Imagen Diagnostica,
Hospital Universitario "Dr. Jose E. Gonzalez",
Monterrey, N.L., Mexico*

Alejandra I. Castillo-Cervantes, M.D.

*Centro Universitario de Imagen Diagnostica,
Hospital Universitario "Dr. Jose E. Gonzalez",
Monterrey, N.L., Mexico*

A. Sofia Sanchez-Gomez, M.D.

*Department of Radiology,
Grupo RIO Centro Integral de Diagnostico Medico.
Guadalajara, Jal., Mexico*

SOCIAL MEDIA COMMITTEE

Guillermo Elizondo-Riojas, M.D., Ph.D.

*Centro Universitario de Imagen Diagnostica,
Hospital Universitario "Dr. Jose E. Gonzalez",
Monterrey, N.L., Mexico*

Oscar A. Chavez-Barba, M.D.

*Department of Radiology,
Antiguo Hospital Civil de Guadalajara
"Fray Antonio Alcalde",
Guadalajara, Jal., Mexico*

J. Mario Bernal-Ramirez, M.D.

*Department of Medical Clinics,
Centro Universitario de Ciencias de la Salud,
Universidad de Guadalajara,
Guadalajara, Jal., Mexico*

Adriana Parada-Gallardo, M.D.

*Department of Radiology,
Hospital General de Zapopan,
Zapopan, Jal., Mexico*

RADIOLOGICAL AND CLINICAL CORRELATION BOARD

GASTROENTEROLOGY

Linda E. Muñoz-Espinosa, M.D., Ph.D.

*Liver Unit, Hospital Universitario
"Dr. Jose E. Gonzalez",
Monterrey, N.L., Mexico*

David Marti-Aguado, M.D., Ph.D.

*Servicio Medicina Digestiva,
Hospital Clinico Universitario,
Valencia, Spain*

GASTROINTESTINAL AND GENERAL SURGERY

Carlos Nuño-Guzman, M.D., M.Sc.

*Department of Surgery,
Antiguo Hospital Civil de Guadalajara
"Fray Antonio Alcalde",
Guadalajara, Jal., Mexico*

OBSTETRICS AND GINECOLOGY

Sergio Fajardo-Dueñas, M.D., M.Sc.

*Division of Obstetrics and Gynecology,
Nuevo Hospital Civil de Guadalajara,
Guadalajara, Jal., Mexico*

NEUROLOGY

Jose L. Ruiz-Sandoval, M.D., M.Sc.

*Department of Neurology,
Antiguo Hospital Civil de Guadalajara
"Fray Antonio Alcalde",
Guadalajara, Jal., Mexico*

RHEUMATOLOGY

Monica Vazquez del Mercado-Espinosa,
M.D., Ph.D.

*Division of Medicine,
Nuevo Hospital Civil de Guadalajara,
Guadalajara, Jal., Mexico.*

CARDIOLOGY-PNEUMOLOGY

Jose M. Hernandez, M.D.

*Department of Eocardiography, Doctors Hospital,
Monterrey, N.L., Mexico*

PATHOLOGICAL ANATOMY

Marco A. Ponce-Camacho, M.D., Ph.D.

*Department of Cytopathology, Doctors Hospital,
Monterrey, N.L., Mexico*

ENDOCRINOLOGY

Jesus Zacarias Villarreal-Perez, M.D.
Department of Endocrinology,
Hospital Universitario "Dr. Jose E. Gonzalez",
Monterrey, N.L., Mexico

HEMATOLOGY

Carlos R. Best-Aguilera, M.D.
Department of Hematology,
Hospital General de Occidente. Secretaria de Salud
Zapopan, Jal., Mexico

PEDIATRIC NEUROLOGY

Daniel Perez-Rulfo Ibarra, M.D., Ph.D.
Departamento de Pediatría,
Antiguo Hospital Civil de Guadalajara
"Fray Antonio Alcalde",
Guadalajara, Jal., Mexico

GYNECOLOGICAL UROLOGY

Patricia I. Velazquez-Castellanos, M.D., M.Sc.
Department of Gynecology and Obstetrics,
Antiguo Hospital Civil de Guadalajara
"Fray Antonio Alcalde",
Guadalajara. Jal., Mexico

Follow us



<https://linkedin.com/company/jmexfri>



<https://instagram.com/jmexfri>



<https://facebook.com/jmexfri>



<https://youtube.com/@jmexfri>



<https://x.com/jmexfri>



Original papers should be deposited in their electronic version through the following URL:

<https://publisher.jmexfri.permanyer.com>



PERMANYER
www.permanyer.com

Permanyer Mexico

Temistocles, 315
Col. Polanco, Del. Miguel Hidalgo
11560 Ciudad de Mexico
mexico@permnyer.com

Permanyer

Mallorca, 310 – Barcelona (Cataluña), España
permnyer@permnyer.com

ISSN: 2696-8444

Ref.: 10130AMEX242



www.permanyer.com

Reproductions for commercial purposes:

Without the prior written consent of the publisher, no part of this publication may be reproduced, stored in a retrievable medium or transmitted, in any form or by any means, electronic, mechanical, photocopying, recording or otherwise, for commercial purposes.

Journal of the Mexican Federation of Radiology and Imaging is an open access publication with the Creative Commons license CC BY-NC-ND (<http://creativecommons.org/licenses/by-nc-nd/4.0/>).

The opinions, findings, and conclusions are those of the authors. The editors and publisher are not responsible and shall not be liable for the contents published in the journal.

© 2024 Federacion Mexicana de Radiologia e Imagen, AC. Published by Permanyer.

Is independent Interventional Radiology the future?

Adrian Brady 

Board of Directors, European Society of Radiology; University College, Cork, Ireland

Interventional radiologists are special (or at least often believe ourselves to be). After all, while diagnostic radiologists look at images, and diagnose, we also actively *do* things to make patients better. Surely that justifies our being considered as a group apart, subject to different rules? However, neuroradiologists, paediatric radiologists, musculoskeletal radiologists and breast radiologists (and all other subspecialty groups) also consider themselves special, often using the same justifications. So, if we all want special treatment, stand-alone status for our special skills, what is the future of radiology as a whole? Is each subspecialty's special pleading for uniqueness (and, consequently, special treatment) ultimately harmful to radiology? Will this trend towards increased subspecialisation (or complete separation of specialties) lead to the development of silos, where individuals work without reference to the generality of patients and without the capacity to offer breadth of expertise to complement depth of knowledge?

The case for some form of independent status for interventional radiology (IR) is strong. It differs from most other radiology subspecialties in combining knowledge of and ability to deploy diagnostic skills with specific requirements for manual dexterity¹. It has many intersections with operative surgery, in that the work of an interventional radiologist often has therapeutic intent, in addition to the usual diagnostic goals underpinning most radiologists' work. Efficient and effective delivery of IR services often requires equipment in addition to diagnostic radiology department tools and dedicated staff (radiologists, radiographers and nurses) with specific training and expertise.

One key feature of successful IR practice is direct interaction with patients and direct responsibility for their care. Many radiologists encounter patients on a daily basis; for example, those who utilise ultrasound speak with their patients in virtually all cases and often have the valuable opportunity to examine the body part under scrutiny. Breast radiologists are frequently key participants in patient clinics. However, in IR, directly encountering one's patients only when performing procedures is really only part of the job. Full IR service provision must also include pre- and post-operative elements of care. The 'father' of IR, Charles Dotter, stated in 1968 that if interventional radiologists did not provide clinical care before and after their procedures, in addition to the procedural element of IR, they would be considered nothing more than 'high-priced plumbers' and seen only as technologists rather than true physicians². The complexity and range of the procedures we can offer are growing rapidly; it would be inappropriate not to ensure that patients have the opportunity to discuss with us in advance what will happen to them and be cared for afterwards by the person with the most knowledge of what has been done to them. Furthermore, as the operators performing invasive and complex procedures, it is our responsibility to offer full explanations and to obtain informed patient consent before intervening. Additionally, we know that patients increasingly expect to be able to interact directly with radiologists (even beyond the IR world) for explanations of their imaging³. This necessitates our conducting (and having the resources to operate) IR clinics and accessing in-patient and day-case beds in hospitals directly¹.

Corresponding author:

Adrian Brady

E-mail: adrianbrady@me.com

2696-8444 / © 2023 Federación Mexicana de Radiología e Imagen, A.C. Published by Permanyer. This is an open access article under the CC BY-NC-ND (<https://creativecommons.org/licenses/by-nc-nd/4.0/>).

Received for publication: 21-11-2023

Accepted for publication: 27-11-2023

DOI: 10.24875/JMEXFRI.M24000070

Available online: 10-07-2024

J Mex Fed Radiol Imaging. 2024;3(2):69-71

www.JMeXFRI.com

Another key element of both threat and opportunity for IR lies in referral patterns. If we remain entirely dependent on referrals of patients from other specialties, we risk having our scope of practice defined by these referrers and losing elements of that practice to other specialties that choose to 'cherry-pick' those procedures that are financially or otherwise attractive to them while leaving to us more difficult or less-attractive work. For this reason, many interventional radiologists believe that we must broaden the sources of our patients, offering referral opportunities to primary care physicians or, in some instances, patients referring themselves directly. Again, this would seem to suggest that existence as an independent specialty is a necessity if IR is to thrive and develop.

In many parts of the world, IR is currently at an inflexion point, as radiologists consider whether or not IR should operate as an entirely independent specialty, and as regulators evaluate the cases for and against a division between the diagnostic and interventional branches of our specialty. The parameters for how IR would function independently have long been established⁴. In some countries, independent status for IR as a subspecialty has been recognised (since 2010 in the UK and 2013 in Canada). In the USA, dual primary certification in IR and diagnostic radiology has been offered by the American Board of Medical Specialties (ABMS) since 2012, which confers recognition of IR as a distinct area of medical practice (without entirely separating it from diagnostic radiology). In many other countries, formal recognition of IR as a subspecialty is also now in place, but recognition as a fully independent specialty remains largely aspirational in most jurisdictions, despite support from many national IR societies and the Cardiovascular and Interventional Radiological Society of Europe (CIRSE)⁵.

There are arguments against full independence for IR. One relies on the fact that some IR has traditionally been part of daily work for many radiologists. Would independence mean those who perform procedures on a part-time or occasional basis would expect, or be expected to cease doing all intervention, leaving all procedures to those specifically trained in IR? This would be impractical, as well as detrimental to patient care. Procedural work is also part of other radiology subspecialties (breast, MSK, etc.). Simpler procedures fall within the remit of many general or subspecialty diagnostic radiologists (biopsies, drainages, etc.) and will need to continue to do so. In many smaller hospitals, there may not be sufficient IR work to employ

enough dedicated interventionalists to facilitate providing a full on-call service, or enough high-level or varied work to attract radiologists whose exclusive focus is based on intervention.

Other arguments against independence are sometimes heard from traditional referring specialties. Some of these may be grounded in uncertainty about the boundaries between their practices and that of interventional radiologists, but these arguments are usually biased by a traditional and outdated view of radiology as a 'non-clinical' specialty⁶. In addition, some colleagues from other specialties may fear competition from newly empowered interventional radiologists who run their own clinics, accept their own direct referrals and manage patients within beds and facilities they control directly.

It is likely that the future will involve some form of hybrid, merging a scenario whereby much simple IR work remains within the purview of predominantly diagnostic radiologists with more complex IR being undertaken by dedicated interventional radiologists acting as independent specialists, without additional responsibilities to cover diagnostic radiology services being expected of them. These dedicated interventionalists could provide services across a number of institutions, to ensure the availability of high-level skills wherever needed and the provision of sufficient personnel to maintain on-call services (where institutions are too small or have insufficient IR demands to provide these from within their own resources). It is unrealistic to demand or expect that all IR can or should migrate from its present home within the world of radiology to a new realm of a separate specialty of IR. However, the need for recognition of high-level IR as a dedicated specialty, with all the privileges, rights and tools required for the provision of proper holistic care to patients, should be supported, provided that continuance of simpler IR as an intrinsic skill and component of the work of most diagnostic radiologists is upheld.

The future is bright for both Diagnostic and Interventional Radiology. In many ways, and in many practice types, we will remain inextricably linked. In some circumstances, IR will function as an independent specialty, while remaining closely linked to our diagnostic brethren. Adapting the mix of these models to the specific environment of practice in a given location is a pragmatic and viable goal for the future.

Funding

Not applicable.

Conflicts of interest

The author discloses no potential conflicts of interest.

Ethical disclosures

Protection of Individuals. Not applicable.

Confidentiality of data. Not applicable.


Right to privacy and informed consent. The author declares no ethical responsibilities because confidential information was not presented.

Use of artificial intelligence for generating text. The author states that he did not use generative artificial intelligence in the preparation of this article.

REFERENCES

1. Brady AP, Uberoi R, Lee MJ, Müller-Hülsbeck S, Adam A. Leadership in Interventional Radiology - Fostering a Culture of Excellence. *Can Assoc Radiol J.* 2023;74(1):185-191. doi: 10.1177/08465371221089249.
2. Allen B Jr. Radiologists adding value through the clinical practice of interventional radiology. *J Am Coll Radiol.* 2015;12(4):319-320. doi: 10.1016/j.jacr.2015.02.023.
3. European Society of Radiology (ESR). Patient survey of value in relation to radiology: results from a survey of the European Society of Radiology (ESR) value-based radiology subcommittee. *Insights Imaging.* 2021;12(1):6. doi: 10.1186/s13244-020-00943-x.
4. Kaufman JA, Reekers JA, Burnes JP, Al-Kutoubi A, Lewis CA, Hardy BW, et al. Global statement defining interventional radiology. *J Vasc Interv Radiol.* 2010;21(8):1147-1149. doi: 10.1016/j.jvir.2010.05.006.
5. European Society of Radiology (ESR); Cardiovascular and Interventional Radiological Society of Europe (CIRSE). Interventional radiology in European radiology departments: a joint survey from the European Society of Radiology (ESR) and the Cardiovascular and Interventional Radiological Society of Europe (CIRSE). *Insights Imaging.* 2019;10(1):16. doi: 10.1186/s13244-019-0698-6.
6. Siskin GP, Englander MJ. It is time for radiologists to stop using the word "clinician". *J Am Coll Radiol.* 2015;12(5):510. doi: 10.1016/j.jacr.2014.09.037.

Artificial intelligence in radiology

Guillermo Elizondo-Riojas^{1,2*}, Adrian A. Negreros-Osuna^{2,3,4}, J. Mario Bernal-Ramirez^{2,5},
and Benjamin Conde-Castro^{2,6}

¹Departamento de Radiología e Imagen, Hospital Universitario "Dr. Jose E. Gonzalez", Facultad de Medicina, Universidad Autónoma de Nuevo Leon., Monterrey, N.L.; ²Artificial Intelligence Committee, Journal of the Mexican Federation of Radiology and Imaging (JMeXFRI); ³Hospital Regional ISSSTE, Monterrey, N.L.; ⁴Escuela de Medicina, Vicerrectoría de Ciencias de la Salud, Universidad de Monterrey, Monterrey, N.L.; ⁵Department of Medical Clinics, Centro Universitario de Ciencias de la Salud, Universidad de Guadalajara, Guadalajara, Jal.; ⁶Facultad de Medicina, Universidad Nacional Autónoma de México, Mexico City, Mexico

ABSTRACT

Artificial intelligence (AI) is revolutionizing clinical medicine, particularly radiology, by enhancing diagnostic accuracy and streamlining operational efficiency. Radiology benefits from AI's prowess in image pattern recognition, which not only augments radiologists' capabilities but also optimizes tasks such as scheduling and radiation monitoring. AI's applications span diagnostic and interventional radiology, enabling the interpretation of complex imaging data through advanced technologies such as convolutional neural networks and radiomics. These tools help detect subtle disease indicators often missed by the human eye. AI also improves radiology department management by automating routine tasks and prioritizing urgent cases to ensure timely medical interventions. Educational programs must evolve to prepare the next generation of radiologists for a future where AI is ubiquitous in their professional landscape. However, integrating AI into radiology brings challenges, including ethical and legal concerns about patient privacy, data security, and potential bias in algorithms. Ethical and legal concerns must be addressed by developing robust guidelines that keep pace with technological advancements. Addressing these issues requires rigorous validation of AI tools across various clinical settings and demographics. Undoubtedly, AI will empower radiologists, enhance their diagnostic capabilities and accuracy, and contribute to precision and personalized medicine.

Keywords: Artificial Intelligence. Radiologists. Radiology. Chatbot.

INTRODUCTION

Artificial intelligence (AI) is, without doubt, the most influential technology currently impacting clinical medicine in general and radiology in particular. AI is changing the way radiology performs medical diagnoses and patient care. Our specialty is particularly suited for AI because it relies on image pattern recognition, something AI excels at. Also, radiology will benefit from the integration of AI because it not only augments the capabilities of radiologists but also improves efficiency, for

example, in scheduling, programming sequences, radiation dose monitoring, segmentation, and many repetitive, time-consuming tasks¹.

As will be seen in this article, AI has many diagnostic and interventional radiology applications². For instance, one of the most important applications in diagnostic radiology is the use of convolutional neural networks for interpreting complex imaging data, i.e., radiomics. With these deep learning algorithms, it is now possible to recognize subtle patterns indicative of disease but undetected/recognized by the human eye/brain³.

*Corresponding author:

Guillermo Elizondo-Riojas
E-mail: guillermo.elizondorj@uanl.edu.mx

Received for publication: 15-04-2024

Accepted for publication: 23-04-2024

DOI: 10.24875/JMEXFRI.M24000073

Available online: 10-07-2024

J Mex Fed Radiol Imaging. 2024;3(2):72-81

www.JMeXFRI.com

2696-8444 / © 2024 Federación Mexicana de Radiología e Imagen, A.C. Published by Permanyer. This is an open access article under the CC BY-NC-ND (<https://creativecommons.org/licenses/by-nc-nd/4.0/>).

For example, for chest radiography, the most performed diagnostic imaging modality in the world, AI has been developed to detect pneumonia, pneumothorax, pulmonary nodules, SARS-COV-2 pneumonia, and the like.

In almost all studies performed so far, AI accuracy levels are comparable and, in many cases, better than radiologists' performance. As discussed further in this review, in addition to increasing diagnostic capabilities, it improves operational efficiency in radiology departments. We need to modify our educational paradigms for radiology professionals for good implementation. On the other hand, although the benefits of AI in radiology are evident, integrating this technology has many challenges. In another section of this review, we discuss the concerns regarding ethical implications, particularly patient privacy, algorithm bias, data security, and algorithm training and failures. Also, implementing these algorithms requires rigorous validation in each clinical setting, demographics, and population in which they will be applied⁴. As we will discuss in this review, there is a need for research in this field, the consideration of ethical aspects, educational adjustments, and time to evaluate the real clinical impact of this technology.

THE CURRENT STATE OF AI IN RADIOLOGY

Much has been written about the promising potential of AI in radiology, with the capacity to transform the field. Mun et al.⁵ and Liew⁶ emphasized the need for strategic positioning and the potential for AI to improve the performance and productivity of radiology services. Malamateniou et al.⁷ and Syed et al.⁸ highlighted the potential for AI to change the role of radiologists and the need for robust validation and interdisciplinary research. Lezzi et al.⁹ and Choy et al.¹⁰ discussed the potential of AI to improve lesion detection and interpretation and enhance various steps in the radiology workflow. Recht et al.¹¹ and Pakdemirli¹² viewed AI as a boon rather than a threat.

A systematic review of the scientific literature in meta-analysis-type publications was conducted to understand the state of the art in AI applications in radiology. These articles provide an important objective filter of publications that offer a more substantial consolidation of evidence, assessment of technology applicability, and identification of trends in a field of study. The systematic review was conducted using the following methodology (Figure 1): searches were performed in PubMed from January 1, 2019, to April 1, 2024, using the MeSH terms "Diagnostic Imaging" AND "Artificial Intelligence," with no language restrictions, excluding articles categorized as

"books and documents," and from the species filter, only "humans" were included while preprints were excluded, identifying 102 meta-analyses.

All titles and abstracts were examined to determine eligibility, excluding studies from other specialized branches of medicine where the radiologist is not directly responsible and articles from the biomedical branch where engineers are responsible for using these tools. A total of 45 publications¹³⁻⁵⁷ corresponding to clinical imaging were included. Each article was comprehensively reviewed to classify it into an imaging subspecialty category and to synthesize the clinical applications for each area.

AI applications according to the clinical area are synthesized in Table 1, indicating sufficient evidence to undergo meta-analysis-type evaluations. Six distinct clinical categories were identified: oncology, neuroradiology, breast, orthopedics, thorax, and abdomen. AI, with the most meta-analysis-type publications, was related to oncologic imaging (44.5%), neuroradiology (20.0%), and breast imaging (13.3%). These publications are categorized according to the process or stage at which they are used, from detecting an anomaly associated with a disease to providing diagnostic support for a specific disease. Results vary from dichotomous distinctions between benign and malignant outcomes to complex analyses such as radiomics, which are used for more precise diagnoses and even for predicting various outcomes, including disease survival and responses to chemotherapy in breast cancer.

As the application of AI in imaging continues to advance, the volume of evidence is expected to increase correspondingly. This expansion requires rigorous evaluation of data quality. One of the most effective strategies for ensuring this is to persistently document and analyze the findings using the highest quality of evidence, such as that provided by meta-analyses.

IMPACT OF AI IN RADIOLOGY DEPARTMENT AUTOMATIZATION

In radiology departments, AI can help automate routine tasks, preliminary analysis, filling structured reports, and the like. Moreover, AI is now being used to prioritize urgent cases for radiologists to review, ensuring timely attendance in life-threatening conditions, a crucial improvement in emergency care settings⁵⁸.

AI automates routine tasks—scheduling, programming imaging sequences, monitoring radiation doses, and segmenting images—which are traditionally time-consuming and prone to human error. By handling these tasks,

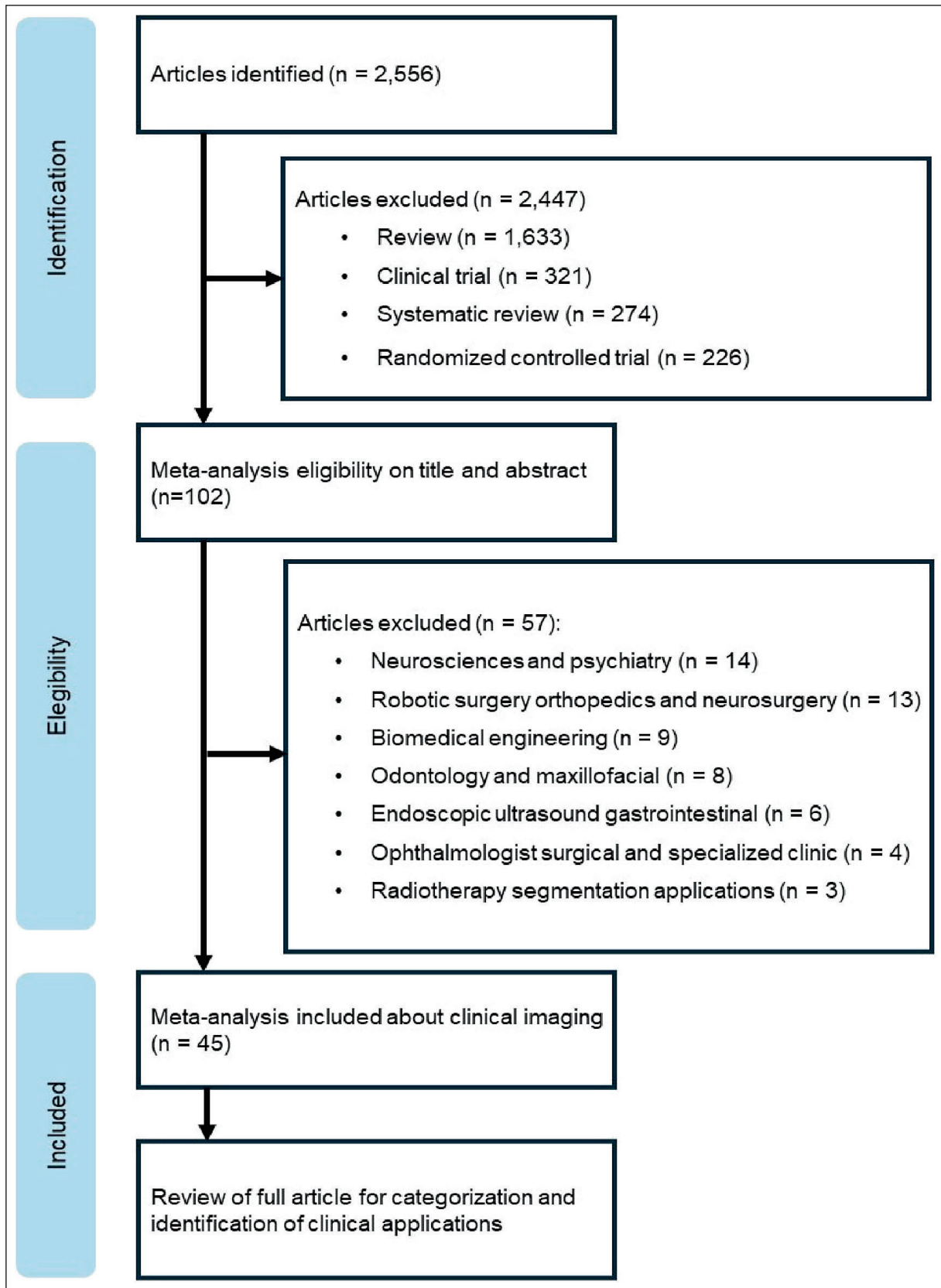


Figure 1. The flowchart of a systematic literature search performed in PubMed from January 1, 2019, to April 1, 2024, using the MeSH terms “Diagnostic Imaging” AND “Artificial Intelligence.” A total of 45 articles corresponding to clinical imaging were included. Each article was comprehensively reviewed to classify it into an imaging subspecialty category and to synthesize the clinical applications for each area.

Table 1. AI applications by clinical specialty of the 45 selected meta-analyses using the MeSH terms “Diagnostic Imaging” AND “Artificial Intelligence”

Clinical area	n (%)	Clinical applications	# References
Oncology	20 (44.5)	<ul style="list-style-type: none"> – Detection of lung cancer, brain metastases, prostate cancer, and head and neck cancer. – Preoperative lymph node staging for colorectal cancer. – Support in diagnosing glioma, lymph node metastasis in patients with abdominopelvic malignancy, and thyroid nodules by ultrasound. – Differentiation between malignant and benign focal liver lesions on ultrasound, treatment-related effects versus tumor progression in brain tumors. – Diagnosis and postoperative surveillance of malignant neoplasms of the upper gastrointestinal tract. – Radiomics in diagnosing and predicting esophageal cancer, medulloblastoma subgroups, differentiation of glioma types, HCC recurrence, and survival prediction in patients with gastric cancer. 	13–32
Neuroradiology	9 (20.0)	<ul style="list-style-type: none"> – Detection of middle cerebral artery occlusion, intracranial hemorrhage, subdural hematoma, intracranial aneurysm, and Alzheimer’s disease. – Detection of early changes in early stroke on non-contrast CT. – Predicting the risk of cerebral aneurysm rupture. – Radiomics in the diagnosis and prognosis of intracranial meningioma. 	33–41
Breast	6 (13.3)	<ul style="list-style-type: none"> – Mammography and digital tomosynthesis to aid diagnosis. – Prediction of lymph node metastases in breast cancer patients and response to neoadjuvant chemotherapy. 	42–47
Orthopedics	4 (8.9)	Diagnostic support for acute rib fracture, wrist fracture, bone age, and body composition.	48–51
Chest	4 (8.9)	Diagnostic support for pneumothorax, tuberculosis, coronavirus, and pulmonary thromboembolism.	52–55
Abdomen	2 (4.4)	Diagnostic support for hepatic fibrosis and nonalcoholic fatty liver disease	56–57

AI: artificial intelligence; HCC: hepatocellular carcinoma; CT: computed tomography; MeSH: Medical Subject Headings.

AI frees radiologists to concentrate on more complex and nuanced diagnostic challenges, thus optimizing departmental workflow and productivity.

AI can also support non-diagnostic tasks, such as result communication and integration into electronic health record systems to improve radiology report quality^{9,59}. AI can also facilitate rapid diagnosis and management in emergency radiology by reducing acquisition times and optimizing image quality⁵⁹.

EDUCATIONAL IMPLICATIONS OF AI IN RADIOLOGY

There is no doubt that AI will empower radiologists, enhancing our diagnostic capabilities and accuracy and contributing to precision and personalized medicine. Radiologists in general, but residents in particular, need to be trained not only in traditional radiology but also in the use of AI, knowing its applications and limitations, and leading the way to integrate AI into clinical practice to better care for our patients⁶⁰.

Education and training for radiology professionals are undergoing a fundamental shift to accommodate the

technological advancements brought about by AI. Traditional curricula must be expanded to include AI literacy, ensuring that radiologists are not only proficient in their conventional roles but also better equipped to handle the intricacies of AI tools. This dual expertise is crucial for the ethical deployment of AI, as it empowers radiologists to use these tools judiciously and effectively, recognizing their strengths and limitations.

Therefore, radiologists must undergo thorough training in the use and limitations of AI tools. This training ensures they can effectively integrate AI insights into their diagnostic processes while maintaining oversight and the capacity to intervene or disagree with AI-generated conclusions. In the context of training algorithms and models, understanding how these models get their conclusions is crucial for the early detection of potential errors. Such preparedness helps mitigate the risk of overreliance on these technologies and maintains the essential role of professional judgment in patient care.

Adopting AI requires significant educational adjustments for radiology professionals, equipping them with skills to use and understand AI effectively. Radiologists can address this by educating themselves and their

peers about AI. Training programs for radiologists must include AI education to ensure that it is always used in the patient's best interest.

ETHICAL ASPECTS OF AI IN RADIOLOGY

Any human activity falls within the scope of ethics, and AI in radiology is not an exception. When using machines to make decisions, important ethical considerations must be remembered. To acknowledge this, the European and North American Multisociety Statement emerged in 2019, where several ethical scenarios are discussed with direct questions posed to potential users of AI in radiology. Shortly later, Geis et al. published a summary of the most relevant points for further examination, implying ethical questions involving data acquisition and sharing, training algorithms/models, and integration into radiology practice⁶¹. When considering data, the primary concerns revolve around achieving a balance between obtaining appropriate patient consent for data usage and determining the extent to which data should be available without compromising privacy⁶².

Privacy concerns top the list, with AI systems handling vast amounts of sensitive patient data, necessitating stringent measures to safeguard this information against breaches. Additionally, there is the ever-present risk of bias in AI algorithms, which can arise from skewed training data or flawed design, potentially leading to discriminatory practices in patient care. As radiologists, our focus should be on gathering data for the common good rather than just for financial gain, emphasizing the importance of ethical practices and the responsible use of medical information to advance healthcare and improve patient outcomes.

Another concern is the growing need for accurately labeled data, potentially resulting in unethical data use. This lack of accuracy can result in skewed data that accurately represents the broader population, which may lead to misinformed conclusions and ineffective policies. This problem demands the implementation of rigorous data management guidelines.

A significant issue is the possibility of bias emerging due to the lack of a diverse sample encompassing various ethnic backgrounds. Furthermore, an imbalance in algorithm access could result in AI benefits being monopolized by a select few. This imbalance could lead to significant disparities in healthcare quality between countries, widening the gap between developed and developing nations and undermining the potential for global health advancement.

Understanding algorithms and models will be possible only if the transparency of the models is guaranteed,

enabling us to perform necessary adjustments to ensure accuracy and reliability. Moreover, transparent models allow for greater collaboration among researchers, facilitating improvements and innovations that can enhance the overall effectiveness of the algorithms. This collaborative environment is essential for fostering trust and confidence among users, who rely on these models for critical decision-making.

Incorporating AI into radiological practice requires a robust ethical infrastructure that prioritizes the common good and ensures the development of AI technologies that center on optimizing patient care rather than prioritizing financial gains. However, it also demands an acute awareness and mitigation of automation bias⁶³. This bias is critical, especially in fields such as radiology, where placing too much trust in AI decisions can harm patients. Ultimately, continuous monitoring and thoughtful consideration of the changing contexts where we can use AI in our field are essential. This approach involves regular reviews and updates of algorithms to adapt to new data and clinical realities, ensuring they remain reliable and accurate. This rigorous task will help us adhere to the foundational principle of medicine: *"First, do no harm."*

LEGAL ASPECTS OF AI IN RADIOLOGY

One of the commonly perceived challenges of AI is the possibility of replacing radiologists. There is only one thing more complicated than the technical complexity of replacing a radiologist, and that is the legal hurdle it represents. Moving to AI-driven diagnostics requires navigating a complex landscape of regulatory standards and liability concerns. These legal hurdles emphasize the need for a careful approach where AI supports rather than replaces human experts, ensuring compliance and safeguarding patient welfare.

The perfection of an AI algorithm is unattainable, and even if we could reach this utopian scenario, any algorithm would gradually lose its precision due to data drift⁶⁴. Regardless of the specific algorithm, it is certain that AI will eventually fail at some point. When it does, a crucial question arises: who is at fault? The legal system will likely target the supervising radiologist, while the engineers who designed the system might face only indirect legal involvement. This disparity in accountability raises significant concerns about fairness and the distribution of responsibility within the field. It underscores the need for clear guidelines and regulations that delineate the roles and responsibilities of all involved in developing and deploying AI technologies in healthcare. Establishing these standards to

fairly distribute responsibility, enhance system safety, and safeguard the interests of both patients and practitioners is crucial.

From a practical standpoint, AI algorithms are treated as medical devices⁵⁶, meaning they are not inherently liable in civil terms. The radiologist using them retains all responsibility and is entrusted with making the final judgment. Suppose a mistake occurs, and a patient intends to sue. In that case, four fundamental assertions must be proven that the radiologist assumed a contractual responsibility during the interpretation of their study, this duty was neglected, the neglect caused harm, and this harm resulted in detailed injuries⁶⁵.

In a few words, a radiologist–patient relationship must have been established. Nevertheless, what happens in the case of an AI algorithm? Is there such a thing as an algorithm–patient relationship? Some authors have proposed viewing the algorithm as a medical student during their clinical rotations: they have contact with patients, they may handle some procedures related to their management, and some tasks may be unsupervised because they do not have the decision-making power or final responsibility over the patient^{66,67}.

Therefore, while AI may assist in diagnostic processes and patient management, the supervising healthcare professionals, radiologists, ultimately hold the final decision-making power and legal responsibility. This distinction is crucial for legal purposes, and both patients and practitioners must understand it clearly to manage expectations and responsibilities effectively when using AI in medical settings.

We have only touched upon a few legal implications of using AI in radiology. However, replacing a radiologist with a complex AI model is far from achievable, especially from a legal perspective. Numerous legal challenges, including liability, consent, and oversight, must be thoroughly addressed before such a transition can occur. Additionally, regulatory frameworks are still evolving to remain up-to-date with the rapid growth in AI technology, creating a landscape of uncertainty. It is clear that while AI can augment and enhance the capabilities of radiologists, replacing them involves intricate legal considerations that are currently unresolved and require significant attention and development.

The legal implications of AI in radiology are complex and multifaceted. As AI systems increasingly take on more diagnostic and decision-making tasks, questions about liability and accountability in cases of errors become particularly significant. Current legal frameworks lag behind the rapid pace of AI development,

struggling to clearly define the responsibilities of AI developers, users, and healthcare providers. This lag not only poses a risk to patient safety but also impedes the potential for AI to be fully integrated into clinical practice. Legal structures need to be refined and adapted to protect patient welfare while supporting innovation.

THE FUTURE OF AI IN RADIOLOGY

It is imperative to delve into the past to contemplate potential trends in AI in radiology, to recall the development of emerging technologies described in Gartner's Hype Cycle⁶⁸, and to identify the obstacles and achievements thus far. Several years ago, the challenge lay in constructing systems capable of segmenting normal anatomical structures, followed by the ability to identify lesions or to discern whether a study was normal or abnormal. These initial systems formed the base for developing robust AI applications in radiology. A substantial number can be found in open-source repositories authorized for use in developing new systems or for research purposes.

The future of AI in radiology will impact all areas of radiology. While the essence remains the same, the methods may vary, e.g., in interventional radiology, there are potential applications in procedural planning, execution, vascular imaging, radiomics, touchless software interactions, robotics, natural language processing, post-procedural outcome prediction, device navigation, image acquisition execution, and follow-up. It can also enhance the efficiency and accuracy of radiological diagnoses and treatments⁶⁹. AI can improve lesion detection, segmentation, and interpretation, and it offers prognostic information⁹. Overall, AI, augmented reality, and virtual reality have the potential to revolutionize interventional radiology, but careful study, validation, and application are needed⁷⁰. The same occurs with pediatric⁷¹, cardiac⁷², and musculoskeletal radiology, where some discuss the role of AI and emphasize the need for collaboration between AI researchers and clinical radiologists to enhance the capabilities of radiologists^{54,73}.

AI has also shown significant potential in improving image acquisition^{59,74}. It can automate tasks such as image normalization, quality improvement, and noise reduction, leading to better visualization of anatomical structures and lesions⁷⁵. Despite these advancements, the implementation of AI in radiology faces challenges, including the need for AI-ready data structures. Chae et al.⁷⁶ proposed a standardized framework for step-by-step implementation of AI into radiology clinical practice,

focusing on three key components: problem identification, stakeholder alignment, and pipeline integration. They highlight the inherent challenges in this process due to the many factors and conditions that must be met for proper implementation, such as effective data acquisition, multidisciplinary work, user-centered metrics in real-world environments, and the use of existing software in clinical workflows. They conclude that with the assistance of these steps, the implementation of AI could be standardized. Furthermore, to accelerate innovation and bridge gaps, there must be data liberation and crowdsourcing in medical research with the establishment of large-scale and accessible repositories⁷⁷. Even with these challenges, AI in radiology is expected to revolutionize the field and improve patient care quality and depth.

On the other hand, AI is being applied in conjunction with natural language processing (NLP) to create and refine chatbots. A chatbot is essentially a software application that mimics human conversation, whether it is in written or spoken form. These emerging technologies can be utilized to improve the capacity of chatbots to simulate a more natural and free-flowing conversation, enabling individuals to engage with electronic devices as if they were having a conversation with a real person. In the medical field, this application is increasingly common and promising. In this regard, medical chatbots can assist in various tasks, from providing basic information about diseases and symptoms to offering personalized medical advice and medication reminders. These systems can be especially useful in providing basic healthcare in remote areas or addressing common patient queries, freeing healthcare professionals' time for more complex tasks. Medical chatbots can offer valuable healthcare information to the right people in a timely manner and enhance doctors' workflow. Sowmya et al.⁷⁸ pointed out the advantages of chatbots in making accurate diagnoses and easing the burden on medical professionals. Nimal et al.⁷⁹ and Kaladevi et al.⁸⁰ emphasized the importance of chatbots in managing patient flow and cutting healthcare expenses. Others have provided insights into current chatbot solutions and how they can facilitate better connections between patients and doctors. These studies collectively suggest that chatbots have the potential to significantly improve doctors' workflow by streamlining processes, enhancing patient care, and reducing costs. However, it is important to note that medical chatbots must be developed with utmost care and precision as they deal with delicate and potentially sensitive information. The security and privacy of patient data are critical considerations in designing and implementing these systems.

Many may wonder whether there will be mobile or computer applications in AI that perform disease diagnostics with AI. The answer is that it is very likely. Numerous AI applications are in development with potential benefits throughout the imaging chain. The initial questions are: How accessible will these applications be, and who will bear responsibility for the outcomes? When discussing the future of AI in radiology, an inevitable question emerges about the potential replacement of radiologists by AI. *The simple response is: No.* Nevertheless, the roles of radiologists will undoubtedly change, with AI becoming an integral part of their daily practice. It will seamlessly merge, much like smartphones do, without you realizing it. While AI algorithms will enhance efficiency in certain tasks within their workflow, the essence of a radiologist's job remains intricate, centered on resolving complex clinical issues. Augmented radiology is a field that integrates AI and advanced technologies such as virtual and augmented reality. The transition to this discipline, where radiologists play a key role, is seen as a strategy for success⁶. The impending challenge for radiologists is to acclimate to the forthcoming changes generated by AI integration.

As we look to the future, the role of AI in radiology is poised to expand dramatically. As AI technologies evolve, they will increasingly influence all aspects of radiological practice, from diagnostic accuracy and treatment planning to patient interaction and follow-up care. The ongoing development of AI promises not only more sophisticated diagnostic tools but also platforms for personalized medicine, where AI's data-processing capabilities can be leveraged to tailor treatments to individual patient profiles.

CONCLUSION

The integration of AI into the field of radiology marks a transformative era, revolutionizing the methodology and philosophy of diagnostics and patient care. While the integration of AI into radiology significantly improves diagnostic and operational efficiencies, it also poses ethical, legal, and educational challenges. The path forward involves a balanced approach that considers these aspects, ensuring that AI's integration into radiology not only enhances technical capabilities but also adheres to the highest standards of patient care and safety.

As we navigate this complex terrain, we must focus on leveraging AI to benefit patients, supported by ongoing research, thoughtful policy-making, and comprehensive educational reforms. This approach will ensure that AI serves as a beneficial tool in the quest to

advance radiology, ultimately improving patient outcomes and streamlining processes in healthcare settings. AI's integration into radiology practice means a paradigm shift in how imaging data is used and interpreted for patient care. AI profoundly challenges and reshapes ethical norms, legal frameworks, and educational paradigms in radiology.

Acknowledgments

The authors thank Professor Ana M. Contreras-Navarro for her guidance in preparing and writing this scientific article.

Funding

The authors declare that they received no funding or support for this article.

Conflicts of interest

The authors declare no conflicts of interest.

Ethical disclosures

Protection of individuals. The author declares that no experiments were performed on humans or animals.

Confidentiality of data. The author declares that no patient data are included in this article.

Right to privacy and informed consent. The authors declare that no patient data appear in this article.

Use of artificial intelligence. The authors state that they did not use generative artificial intelligence to prepare this manuscript and/or create tables, figures, or figure legends.


REFERENCES

1. Yasaka K, Abe O. Deep learning and artificial intelligence in radiology: Current applications and future directions. *PLoS Med.* 2018;15(11):e1002707. doi:10.1371/journal.pmed.1002707.
2. O'Brien AJ, Vrazas JI, Clements W. Current applications of algorithmic artificial intelligence in interventional radiology: A review of the literature. *J Med Imaging Radiat Oncol.* 2024;68(2):194-207. doi:10.1111/1754-9485.13609.
3. Tariq A, Purkayastha S, Padmanaban GP, Krupinski E, Trivedi H, Banerjee I, et al. Current Clinical Applications of Artificial Intelligence in Radiology and Their Best Supporting Evidence. *J Am Coll Radiol* 2020;17(11):1371-1381. doi:10.1016/j.jacr.2020.08.018.
4. Koohi-Moghadam M, Bae KT. Generative AI in Medical Imaging: Applications, Challenges, and Ethics. *J Med Syst.* 2023;47(1):94. doi:10.1007/s10916-023-01987-4.
5. Mun SK, Wong KH, Lo SCB, Li Y, Bayarsaikhan S. Artificial Intelligence for the Future Radiology Diagnostic Service. *Front Mol Biosci.* 2021;7:614258 doi:10.3389/fmolb.2020.614258.
6. Liew C. The future of radiology augmented with Artificial Intelligence: A strategy for success. *Eur J Radiol.* 2018;102:152-156. doi:10.1016/j.ejrad.2018.03.019.
7. Malamateniou C, Knapp KM, Pergola M, Woznitza N, Hardy M. Artificial intelligence in radiography: Where are we now and what does the future hold? *Radiography.* 2021;27(S1):S58-62. doi:10.1016/j.radi.2021.07.015.
8. Syed AB, Zoga AC. Artificial Intelligence in Radiology: Current Technology and Future Directions. *Semin Musculoskelet Radiol.* 2018;22(5):540-545. doi:10.1055/s-0038-16733.
9. Lezzi R, Goldberg SN, Merlino B, Posa A, Valentini V, Manfredi R. Artificial Intelligence in Interventional Radiology: A Literature Review and Future Perspectives. *J Oncol.* 2019;2019:6153041. doi:10.1155/2019/6153041.
10. Choy G, Khalilzadeh O, Michalski M, Do S, Samir AE, Panykh OS, et al. Current applications and future impact of machine learning in radiology. *Radiology.* 2018;288(2):318-328. doi:10.1148/radiol.2018171820.
11. Recht M, Bryan RN. Artificial Intelligence: Threat or Boon to Radiologists? *J Am Coll Radiol* 2017;14(11):1476-1480. doi:10.1016/j.jacr.2017.07.007.
12. Pakdemirli E. Artificial intelligence in radiology: friend or foe? Where are we now and where are we heading? *Acta Radiol Open.* 2019;8(2):205846011983022. doi:10.1177/2058460119830222.
13. Bedrikovetski S, Dudi-Venkata NN, Kroon HM, Seow W, Vather R, Carneiro G, et al. Artificial intelligence for pre-operative lymph node staging in colorectal cancer: a systematic review and meta-analysis. *BMC Cancer.* 2021;21(1):1058. doi:10.1186/s12885-021-08773-w.
14. Thong LT, Chou HS, Chew HSJ, Lau Y. Diagnostic test accuracy of artificial intelligence-based imaging for lung cancer screening: A systematic review and meta-analysis. *Lung Cancer.* 2023;176:4-13. doi:10.1016/j.lungcan.2022.12.002.
15. Chidambaram S, Sounderajah V, Maynard N, Markar SR. Diagnostic Performance of Artificial Intelligence-Centred Systems in the Diagnosis and Postoperative Surveillance of Upper Gastrointestinal Malignancies Using Computed Tomography Imaging: A Systematic Review and Meta-Analysis of Diagnostic Accuracy. *Ann Surg Oncol.* 2022;29(3):1977-1990. doi:10.1245/s10434-021-10882-6.
16. Bedrikovetski S, Dudi-Venkata NN, Maicas G, Kroon HM, Seow W, Carneiro G, et al. Artificial intelligence for the diagnosis of lymph node metastases in patients with abdominopelvic malignancy: A systematic review and meta-analysis. *Artif Intell Med.* 2021;113:102022. doi:10.1016/j.artmed.2021.102022.
17. Potipimpanon P, Charakom N, Hirunwiwatkul PA comparison of artificial intelligence versus radiologists in the diagnosis of thyroid nodules using ultrasonography: a systematic review and meta-analysis. *Eur Arch Otorhinolaryngol.* 2022;279(11):5363-5373. doi:10.1007/s00405-022-07436-1.
18. Menon N, Guidozzi N, Chidambaram S, Markar SR. Performance of radiomics-based artificial intelligence systems in the diagnosis and prediction of treatment response and survival in esophageal cancer: a systematic review and meta-analysis of diagnostic accuracy. *Dis Esophagus.* 2023;36(6):doad034. doi:10.1093/dote/doad034.
19. Zhao J, Huang Y, Song Y, Xie D, Hu M, Qiu H, et al. Diagnostic accuracy and potential covariates for machine learning to identify IDH mutations in glioma patients: evidence from a meta-analysis. *Eur Radiol.* 2020;30(8):4664-4674. doi:10.1007/s00330-020-06717-9.
20. Karabacak M, Ozkara BB, Ozturk A, Kaya B, Cirak Z, Orak E, et al. Radiomics-based machine learning models for prediction of medulloblastoma subgroups: a systematic review and meta-analysis of the diagnostic test performance. *Acta Radiol.* 2023;64(5):1994-2003. doi:10.1177/02841851221143496.
21. Bhandari A, Marwah R, Smith J, Nguyen D, Bhatti A, Lim CP, et al. Machine learning imaging applications in the differentiation of true tumour progression from treatment-related effects in brain tumours: A systematic review and meta-analysis. *J Med Imaging Radiat Oncol.* 2022;66(6):781-797. doi:10.1111/1754-9485.13436.
22. Campello CA, Castanha EB, Vilardo M, Staziaki P V, Francisco MZ, Mohajer B, et al. Machine learning for malignant versus benign focal liver lesions on US and CEUS: a meta-analysis. *Abdom Radiol.* 2023;48(10):3114-3126. doi:10.1007/s00261-023-03984-0.
23. Cho SJ, Sunwoo L, Baik SH, Bae YJ, Choi BS, Kim JH. Brain metastasis detection using machine learning: a systematic review and meta-analysis. *Neuro Oncol.* 2021;23(2):214-225. doi:10.1093/neuonc/noaa232.
24. Lee JH, Choi Y, Hong H, Kim YT, Goo JM, Kim H. Prognostic value of CT-defined ground-glass opacity in early-stage lung adenocarcinomas: a single-center study and meta-analysis. *Eur Radiol.* 2023;34(3):1905-1920. doi:10.1007/s00330-023-10160-x.
25. Jian A, Jang K, Manuguerra M, Liu S, Magnussen J, Di Ieva A. Machine Learning for the Prediction of Molecular Markers in Glioma on Magnetic Resonance Imaging: A Systematic Review and Meta-Analysis. *Neurosurgery.* 2021;89(1):31-44. doi:10.1093/neuros/nyab103.
26. Sohn CK, Bisdas S. Diagnostic Accuracy of Machine Learning-Based Radiomics in Grading Gliomas: Systematic Review and Meta-Analysis. *Contrast Media Mol Imaging.* 2020;2020:2127062. doi:10.1155/2020/2127062.
27. van Kempen EJ, Post M, Mannil M, Witkam RL, ter Laan M, Patel A, et al. Performance of machine learning algorithms for glioma segmentation of brain MRI: a systematic literature review and meta-analysis. *Eur Radiol.* 2021;31(12):9638-9653. doi:10.1007/s00330-021-08035-0.
28. Rokhshad R, Salehi SN, Yavari A, Shobeiri P, Esmaeili M, Manila N, et al. Deep learning for diagnosis of head and neck cancers through radiographic data: a systematic review and meta-analysis. *Oral Radiol.* 2024;40(1):1-20. doi:10.1007/s11282-023-00715-5.

29. Jin J, Jiang Y, Zhao YL, Huang PT. Radiomics-based Machine Learning to Predict the Recurrence of Hepatocellular Carcinoma: A Systematic Review and Meta-analysis. *Acad Radiol.* 2024;31(2):467-479. doi:10.1016/j.acra.2023.09.008.
30. Zhao WJ, Fu LR, Huang ZM, Zhu JQ, Ma BY. Effectiveness evaluation of computer-aided diagnosis system for the diagnosis of thyroid nodules on ultrasound. *Medicine.* 2019;98(32):e16379. doi:10.1097/MD.00000000000016379.
31. Adili D, Mohetaer A, Zhang W. Diagnostic accuracy of radiomics-based machine learning for neoadjuvant chemotherapy response and survival prediction in gastric cancer patients: A systematic review and meta-analysis. *Eur J Radiol.* 2024;173:111249. doi:10.1016/j.ejrad.2023.111249.
32. Cuocolo R, Cipullo MB, Stanzione A, Romeo V, Green R, Cantoni V, et al. Machine learning for the identification of clinically significant prostate cancer on MRI: a meta-analysis. *Eur Radiol.* 2020;30(12):6877-6887. doi:10.1007/s00330-020-07027-w.
33. Ghozy S, Azzam AY, Kallmes KM, Matsoukas S, Fifi JT, Luijten SPR, et al. The diagnostic performance of artificial intelligence algorithms for identifying M2 segment middle cerebral artery occlusions: A systematic review and meta-analysis. *J Neuroradiol.* 2023;50(4):449-454. doi:10.1016/j.neurad.2023.02.001.
34. Agarwal S, Wood D, Grzedka M, Suresh C, Din M, Cole J, et al. Systematic Review of Artificial Intelligence for Abnormality Detection in High-volume Neuroimaging and Subgroup Meta-analysis for Intracranial Hemorrhage Detection. *Clin Neuroradiol.* 2023;33(4):943-956. doi:10.1007/s00062-023-01291-1.
35. Adamou A, Beltsios ET, Bania A, Gkana A, Kastrop A, Chatziioannou A, et al. Artificial intelligence-driven ASPECTS for the detection of early stroke changes in non-contrast CT: a systematic review and meta-analysis. *J Neurointerv Surg.* 2023;15(e2):e298-e304. doi:10.1136/jnis-2022-019447.
36. Hu J, Wang Y, Guo D, Qu Z, Sui C, He G, et al. Diagnostic performance of magnetic resonance imaging-based machine learning in Alzheimer's disease detection: a meta-analysis. *Neuroradiology.* 2023;65(3):513-527. doi:10.1007/s00234-022-03098-2.
37. Abdollahifard S, Farrokhi A, Kheshti F, Jalali M, Mowla A. Application of convolutional network models in detection of intracranial aneurysms: A systematic review and meta-analysis. *Interv Neuroradiol.* 2023;29(6):738-747. doi:10.1177/15910199221097475.
38. Habibi MA, Fakhouri A, Mirjani MS, Razavi A, Mortezaei A, Soleimani Y, et al. Prediction of cerebral aneurysm rupture risk by machine learning algorithms: a systematic review and meta-analysis of 18,670 participants. *Neurosurg Rev.* 2024;47(1):34. doi:10.1007/s10143-023-02271-2.
39. Daugaard Jørgensen M, Antulov R, Hess S, Lysdahlgaard S. Convolutional neural network performance compared to radiologists in detecting intracranial hemorrhage from brain computed tomography: A systematic review and meta-analysis. *Eur J Radiol.* 2022;146:110073. doi:10.1016/j.ejrad.2021.110073.
40. Abdollahifard S, Farrokhi A, Mowla A. Application of deep learning models for detection of subdural hematoma: a systematic review and meta-analysis. *J Neurointerv Surg.* 2023;15(10):995-1000. doi:10.1136/jnis-2022-019627.
41. Ugga L, Perillo T, Cuocolo R, Stanzione A, Romeo V, Green R, et al. Meningioma MRI radiomics and machine learning: systematic review, quality score assessment, and meta-analysis. *Neuroradiology.* 2021;63(8):1293-1304. doi:10.1007/s00234-021-02668-0.
42. Yoon JH, Strand F, Baltzer PAT, Conant EF, Gilbert FJ, Lehman CD, et al. Standalone AI for Breast Cancer Detection at Screening Digital Mammography and Digital Breast Tomosynthesis: A Systematic Review and Meta-Analysis. *Radiology.* 2023;307(5):e222639 doi:10.1148/radiol.222639.
43. Liu C-J, Zhang L, Sun Y, Geng L, Wang R, Shi K-M, et al. Application of CT and MRI images based on an artificial intelligence algorithm for predicting lymph node metastasis in breast cancer patients: a meta-analysis. *BMC Cancer.* 2023;23(1):1134. doi:10.1186/s12885-023-11638-z.
44. Wang M, Liu Z, Ma L. Application of artificial intelligence in ultrasound imaging for predicting lymph node metastasis in breast cancer: A meta-analysis. *Clin Imaging.* 2024;106:110048. doi:10.1016/j.clinimag.2023.110048.
45. Hickman SE, Woitek R, Le EPV, Im YR, Mouritsen Luxhøj C, Aviles-Rivero AI, et al. Machine Learning for Workflow Applications in Screening Mammography: Systematic Review and Meta-Analysis. *Radiology.* 2022;302(1):88-104. doi:10.1148/radiol.2021210391.
46. Liu J, Lei J, Ou Y, Zhao Y, Tuo X, Zhang B, et al. Mammography diagnosis of breast cancer screening through machine learning: a systematic review and meta-analysis. *Clin Exp Med.* 2023;23(6):2341-2356. doi:10.1007/s10238-022-00895-0.
47. Liang X, Yu X, Gao T. Machine learning with magnetic resonance imaging for prediction of response to neoadjuvant chemotherapy in breast cancer: A systematic review and meta-analysis. *Eur J Radiol.* 2022;150:110247. doi:10.1016/j.ejrad.2022.110247.
48. Bedrikovetski S, Seow W, Kroon HM, Traeger L, Moore JW, Sammour T. Artificial intelligence for body composition and sarcopenia evaluation on computed tomography: A systematic review and meta-analysis. *Eur J Radiol.* 2022;149:110218. doi:10.1016/j.ejrad.2022.110218.
49. Dallora AL, Anderberg P, Kvist O, Mendes E, Diaz Ruiz S, Sanmartin Berglund J. Bone age assessment with various machine learning techniques: A systematic literature review and meta-analysis. *PLoS One.* 2019;14(7):e0220242. doi:10.1371/journal.pone.0220242.
50. Hansen V, Jensen J, Kusk MW, Gerke O, Tromborg HB, Lysdahlgaard S. Deep learning performance compared to healthcare experts in detecting wrist fractures from radiographs: A systematic review and meta-analysis. *Eur J Radiol.* 2024;174:111399. doi:10.1016/j.ejrad.2024.111399.
51. Lopez-Melia M, Magnin V, Marchand-Maillet S, Grabherr S. Deep learning for acute rib fracture detection in CT data: a systematic review and meta-analysis. *Br J Radiol.* 2024;97(1155):535-543. doi:10.1093/bjrt/qae014.
52. Sugibayashi T, Walston SL, Matsumoto T, Mitsuyama Y, Miki Y, Ueda D. Deep learning for pneumothorax diagnosis: a systematic review and meta-analysis. *Eur Respir Rev.* 2023;32(168):220259. doi:10.1183/16000617.0259-2022.
53. Hansun S, Argha A, Liaw ST, Celler BG, Marks GB. Machine and Deep Learning for Tuberculosis Detection on Chest X-Rays: Systematic Literature Review. *J Med Internet Res.* 2023;25:e43154. doi:10.2196/43154.
54. Wang Q, Ma J, Zhang L, Xie L. Diagnostic performance of corona virus disease 2019 chest computer tomography image recognition based on deep learning: Systematic review and meta-analysis. *Medicine (Baltimore).* 2022;101(42):e31346. doi:10.1097/MD.00000000000031346.
55. Soffer S, Klang E, Shimon O, Barash Y, Cahan N, Greenspan H, et al. Deep learning for pulmonary embolism detection on computed tomography pulmonary angiogram: a systematic review and meta-analysis. *Sci Rep.* 2021;11(1):15814. doi:10.1038/s41598-021-95249-3.
56. Decharatanachart P, Chaiteerakij R, Tiyaattanachai T, Treeprasertsuk S. Application of artificial intelligence in chronic liver diseases: a systematic review and meta-analysis. *BMC Gastroenterol.* 2021;21(1):10. doi:10.1186/s12876-020-01585-5.
57. Zhao Q, Lan Y, Yin X, Wang K. Image-based AI diagnostic performance for fatty liver: a systematic review and meta-analysis. *BMC Med Imaging.* 2023;23(1):208. doi:10.1186/s12880-023-01172-6.
58. Al-Dasuqi K, Johnson MH, Cavallo JJ. Use of artificial intelligence in emergency radiology: An overview of current applications, challenges, and opportunities. *Clin Imaging.* 2022;89:61-67. doi:10.1016/j.clinimag.2022.05.010.
59. Kapoor N, Lacson R, Khorasani R. Workflow Applications of Artificial Intelligence in Radiology and an Overview of Available Tools. *J Am Coll Radiol.* 2020;17(11):1363-1370. doi:10.1016/j.jacr.2020.08.016.
60. Tadavarthi Y, Makeeva V, Wagstaff W, Zhan H, Podlasek A, Bhatia N, et al. Overview of Noninterpretive Artificial Intelligence Models for Safety, Quality, Workflow, and Education Applications in Radiology Practice. *Radiol Artif Intell.* 2022;4(2): e210114. doi:10.1148/ryai.210114.
61. Geis JR, Brady AP, Wu CC, Spencer J, Ranschaert E, Jaremko JL, et al. Ethics of Artificial Intelligence in Radiology: Summary of the Joint European and North American Multisociety Statement. *Radiology.* 2019;293(2):436-440. doi:10.1148/radiol.2019191586.
62. Jaremko JL, Azar M, Bromwich R, Lum A, Alicia Cheong LH, Gilbert M, et al. Canadian Association of Radiologists (CAR) Artificial Intelligence Working Group. Canadian Association of Radiologists White Paper on Ethical and Legal Issues Related to Artificial Intelligence in Radiology. *Can Assoc Radiol J.* 2019;70(2):107-118. doi:10.1016/j.carj.2019.03.001
63. Baltzer PAT. Automation Bias in Breast AI. *Radiology.* 2023;307(4):e230770. doi:10.1148/radiol.230770.
64. Mezrich JL. Is Artificial Intelligence (AI) a Pipe Dream? Why Legal Issues Present Significant Hurdles to AI Autonomy. *AJR Am J Roentgenol.* 2022;219(1):152-156. doi:10.2214/AJR.21.27224.
65. Pesapane F, Volonté C, Codari M, Sardaneli F. Artificial intelligence as a medical device in radiology: ethical and regulatory issues in Europe and the United States. *Insights Imaging.* 2018;9(5):745-753. doi:10.1007/s13244-018-0645-y.
66. Sullivan HR, Schweikart SJ. Are Current Tort Liability Doctrines Adequate for Addressing Injury Caused by AI? *AMA J Ethics.* 2019;21(2):E160-166. doi:10.1001/amajethics.2019.160.
67. Chung J, Zink A. Hey Watson, Can I Sue You for Malpractice? Examining the Liability of Artificial Intelligence in Medicine. *Asia-Pac J Health Law and Ethics.* 2018. 51-80.
68. Oosterhoff JHF, Doornberg JN; Machine Learning Consortium. Artificial intelligence in orthopaedics: false hope or not? A narrative review along the line of Gartner's hype cycle. *EFORT Open Rev.* 2020;5(10):593-603. doi:10.1302/2058-5241.5.190092.
69. von Ende E, Ryan S, Crain MA, Makary MS. Artificial Intelligence, Augmented Reality, and Virtual Reality Advances and Applications in Interventional Radiology. *Diagnostics (Basel).* 2023;13(5):892. doi:10.3390/diagnostics13050892.
70. Lecler A, Duron L, Soyler P. Revolutionizing radiology with GPT-based models: Current applications, future possibilities and limitations of ChatGPT. *Diagn Interv Imaging.* 2023;104(6):269-274. doi:10.1016/j.diii.2023.02.003.
71. Desai SB, Pareek A, Lungren MP. Current and emerging artificial intelligence applications for pediatric interventional radiology. *Pediatr Radiol.* 2022;52(11):2173-2177. doi:10.1007/s00247-021-05013-y.
72. Morales MA, Manning WJ, Nezafat R. Present and Future Innovations in AI and Cardiac MRI. *Radiology.* 2024;310(1):e231269. doi:10.1148/radiol.231269.

73. Guerhazi A, Omoumi P, Tordjman M, Fritz J, Kijowski R, Regnard NE, et al. How AI May Transform Musculoskeletal Imaging. *Radiology*. 2024;310(1):e249002. doi:10.1148/radiol.230764. Erratum for: *Radiology*. 2024 Jan;310(1):e230764.
74. Pierre K, Haneberg AG, Kwak S, Peters KR, Hochegger B, Sananmuang T, et al. Applications of Artificial Intelligence in the Radiology Roundtrip: Process Streamlining, Workflow Optimization, and Beyond. *Semin Roentgenol*. 2023;58(2):158-169. doi:10.1053/j.ro.2023.02.003.
75. Ismail D, Gunawan E. Study of the Use of AI (Artificial Intelligence) in the Field of Radiology and Imaging. *Sriwijaya J Radiol Imaging Res*. 2023;1(2):34-38. doi:10.59345/sjrir.v1i2.72.
76. Chae A, Yao MS, Sagreiya H, Goldberg AD, Chatterjee N, MacLean MT, et al. Strategies for Implementing Machine Learning Algorithms in the Clinical Practice of Radiology. *Radiology*. 2024;310(1):e223170. doi:10.1148/radiol.223170.
77. Wilson JR, Prevedello LM, Witiw CD, Flanders AE, Colak E. Data Liberation and Crowdsourcing in Medical Research: The Intersection of Collective and Artificial Intelligence. *Radiol Artif Intell*. 2024;6(1):e230006. doi:10.1148/ryai.230006.
78. Sowmya D, Debbata K, Vignesh GS, Sagar DSN, Bavanthula AR, Pallavi L. Emerging Role of Healthcare Chatbots in Improving Medical Assistance. 2023 3rd Asian Conference on Innovation in Technology (ASIANCON), IEEE; 2023:1-6. doi:10.1109/ASIANCON58793.2023.10270725.
79. Nimal KA, Nair VV, Jegdeep R, Nehru JA. Artificial Intelligence Based Chatbot for Healthcare Applications. *Adv Sci Technol*, 2023;124:370-377. doi:10.4028/p-atr6jg.
80. Kaladevi R, Saidineesha S, Keerthi Priya P, Nithiya KM, Sai Gayatri S. Chatbot For Healthcare Using Machine Learning. 2023 International Conference on Computer Communication and Informatics (ICCCI), IEEE; 2023:1-4. doi:10.1109/ICCCI56745.2023.10128261.

Elastographic patterns of thyroid microcarcinomas: a new proposal

Eduardo R. Cuvertino^{1,2}, Liliana Gelman¹, Mirta Miras-Miartus³, Alejandra Geres⁴,
and Maria L. Cuvertino^{2,5}

¹Departamento de Diagnostico por Imagen, Hospital Nacional de Clinicas de la Facultad de Ciencias Medicas, Universidad Nacional; ²Centro de Estudios Ecograficos; ³Servicio de Endocrinologia, Hospital de Niños de la Santísima Trinidad; ⁴Servicio de Endocrinologia, Hospital Nacional de Clinicas de la Facultad de Ciencias Medicas, Universidad Nacional; ⁵Servicio de Radiologia y Diagnostico por Imagenes, Hospital de Niños de la Santísima Trinidad. Cordoba, Argentina

ABSTRACT

Introduction: Ultrasound (US) elastography for thyroid microcarcinomas has variable diagnostic performance. This study aimed to (1) define the elastographic features of thyroid nodules using two-dimensional shear-wave elastography (2D-SWE) and (2) evaluate the utility of combining conventional US, elastography-strain (E-strain), and 2D-SWE for improving diagnostic performance in thyroid micronodules. **Materials and Methods:** Patients with thyroid nodules were evaluated in a cross-sectional study with conventional US, E-strain, and 2D-SWE. Nodule stiffness, the presence of a perinodular halo, and the halo/nodule A/B index were evaluated using 2D-SWE. Three elastographic patterns were defined based on conventional US, E-strain, and 2D-SWE features. The pathological diagnosis was made by fine needle aspiration biopsy and confirmed by surgery. **Results:** We included 158 patients with 158 thyroid nodules: 64 micronodules ≤ 10 mm and 94 macronodules > 10 mm. Malignancy was confirmed in 58 (36.7%) of 158 nodules, of which 29 were thyroid microcarcinomas. Stiffness at a cutoff value of 23.5 kPa predicted malignancy. Notably, 21 (72.4%) of 29 microcarcinomas with a perinodular halo had a stiffness value of < 23.5 kPa. All microcarcinomas with a perinodular halo ($n = 21$, 100%) had an elastographic stiffness A/B index ≥ 1.3 . A congruent elastographic pattern was defined as thyroid imaging reporting and data system (TI-RADS) 4 or 5, E-strain pattern 4 or 5, with a stiffness ≥ 23.5 kPa without a perinodular halo, and an A/B index < 1.3 by 2D-SWE. An incongruent elastographic pattern was defined as TI-RADS 4 or 5, E-strain pattern 4 or 5, and discordant findings on 2D-SWE with intrinsic thyroid nodule laxity (< 23.5 kPa), a rigid perinodular halo, and an A/B index ≥ 1.3 . An atypical congruent elastographic pattern was defined as TI-RADS 4 or 5 with atypical findings on E-strain (pattern 1, 2, or 3), and 2D-SWE with intrinsic thyroid nodule laxity (< 23.5 kPa), a rigid perinodular halo, and an A/B index ≥ 1.3 . **Conclusion:** Three elastographic patterns of thyroid microcarcinomas are proposed based on 2D-SWE features such as nodule stiffness, a perinodular halo, and an A/B index in combination with conventional US and E-strain. These elastographic patterns have not been described in the literature.

Keywords: Thyroid. Elastography. Thyroid microcarcinoma. Thyroid nodule. Ultrasound. TI-RADS.

*Corresponding author:

Eduardo R. Cuvertino
E-mail: ercuvertino@gmail.com

Received for publication: 01-10-2023

Accepted for publication: 12-01-2024

DOI: 10.24875/JMEXFRI.M24000072

Available online: 10-07-2024

J Mex Fed Radiol Imaging. 2024;3(2):82-92

www.JMeXFRI.com

2696-8444 / © 2024 Federación Mexicana de Radiología e Imagen, A.C. Published by Permanyer. This is an open access article under the CC BY-NC-ND (<https://creativecommons.org/licenses/by-nc-nd/4.0/>).

INTRODUCTION

Ultrasound (US) elastography is an additional tool of conventional US examination and fine needle aspiration biopsy (FNAB) that differentiates benign and malignant thyroid nodules, especially the Bethesda III or IV category cytology cases (malignancy risk rates of 5% and 30%, respectively)¹⁻⁴. Two main thyroid elastography methods are used in clinical practice: real-time elastography strain (E-strain), a qualitative technique of manual compression to assess tissue deformity, and shear wave elastography (SWE), a quantitative estimate of tissue stiffness in kilopascals (kPa) or meters/second that shows a color matrix related to tissue stiffness presented as a two-dimensional SWE (2D-SWE)^{1,2}.

Morphological findings of benign and malignant thyroid nodules are related to the pathological type of the tumor and the size of the lesion¹. Many malignant thyroid micronodules (≤ 10 mm) have no obvious morphological changes, which is a problem when conventional ultrasound is used for diagnosis. On the other hand, 2D-SWE has improved the characterization of thyroid nodules with high specificity of tissue stiffness, which positively correlates with nodule malignancy. A malignant thyroid nodule is stiffer than a benign nodule⁵. However, US elastography has variable diagnostic performance in thyroid microcarcinomas.

A few reports have evaluated the diagnostic value of 2D-SWE in thyroid microcarcinomas. Their intrinsic structure may affect stiffness, as measured by elastography, and there is evidence that tissue stiffness is lower in micronodules than in large nodules^{5,6}. It has been suggested that elastographic assessment of perinodular tissue can contribute to the differential diagnosis⁶. Therefore, this study aimed to (1) define the elastographic features of thyroid nodules using 2D-SWE and (2) evaluate the utility of combining the findings of conventional US, E-strain, and 2D-SWE for improving diagnostic performance in thyroid micronodules.

MATERIALS AND METHODS

This retrospective cross-sectional study was conducted from May to November 2021 at the Diagnostic Imaging Department of the National Hospital of Clinics, Faculty of Medical Sciences of the National University and Center of Ultrasound Studies, in Córdoba, Argentina. Patients of both sexes with thyroid nodules detected by conventional US were included. The study was

approved by the institutional research committee, and written informed consent was obtained from all patients.

Development and study variables

Patients with thyroid nodules were evaluated by grayscale US, color Doppler US, E-strain, and 2D-SWE. The variables were age, sex, Thyroid Imaging Reporting and Data System (TI-RADS) category, and thyroid nodule volume.

Definitions

Micronodule: ≤ 10 mm in diameter on US grayscale.

Macronodule: > 10 mm in diameter on US grayscale.

E-strain pattern: Rago score⁸ was used: 1 point indicates the elasticity of the entire examined area of the thyroid nodule; 2 points, the elasticity of a large portion; 3 points, the elasticity only in the periphery; 4 points, the lack of elasticity of the nodule; and 5 points, the lack of elasticity of the nodule and the perinodular area. The green color of the map indicates low stiffness, while the red color indicates non-deformable hard tissue.

Tissue stiffness (kPa): This is the unit of measure of pixel density obtained by 2D-SWE that quantifies stiffness. Stiffness is expressed in a color matrix from blue (soft) to red (hard).

Halo/nodule stiffness index (A/B index): a quantitative measure proposed by the authors (EC and MC) which evaluates the 2D-SWE color matrix. (A) corresponds to the stiffness of an extended region of interest (ROI) that includes the thyroid nodule + a perinodular halo (up to 2 mm outside the nodule boundary). (B) corresponds to the stiffness of the nodule ROI.

Image acquisition and analysis protocol

Thyroid nodule examinations were performed with a Resona 7 ultrasound (Mindray Medical International, Shenzhen, China) and an L14-5 linear transducer with the recent real-time SWE version. This system has a single-layer analysis function that measures stiffness and the margin surrounding the lesion with 0.5 mm increments.

After conventional US examination, elastographic images were acquired in the same section for approximately 4–6 s. The nodule and adjacent thyroid tissue were examined, and thyroid nodules were aspirated. Elastographic acquisitions were performed with E-strain and 2D-SWE five-sequence images. The ROIs (extranodular, intranodular, and perinodular) were selected,

Table 1. Thyroid micronodule and macronodule characteristics by TI-RADS, E-strain, and Bethesda System

Description	Total (n = 158)	Thyroid micronodules ^a (n = 64)	Thyroid macronodules ^b (n = 94)
Women, n (%)	131 (82.9)	54 (84.4)	77 (81.9)
Men, n (%)	27 (17.1)	10 (15.6)	17 (18.1)
TI-RADS, n (%)			
2	19 (12.0)	2 (3.1)	17 (18.0)
3	50 (31.6)	15 (23.4)	35 (37.2)
4	63 (39.9)	35 (54.7)	28 (29.8)
5	26 (16.5)	12 (18.8)	14 (15.0)
E-strain pattern, n (%)			
2	52 (32.9)	16 (25.0)	36 (38.4)
3	34 (21.5)	8 (12.5)	26 (27.6)
4	60 (38.0)	34 (53.1)	26 (27.6)
5	12 (7.6)	6 (9.4)	6 (6.4)
Bethesda System, n (%)			
II	92 (58.2)	28 (43.8)	64 (68.1)
III	12 (7.6)	11 (17.2)	1 (1.0)
IV	7 (4.4)	2 (3.1)	5 (5.3)
V	44 (27.9)	21 (32.8)	23 (24.5)
VI	3 (1.9)	2 (3.1)	1 (1.1)
Pathological diagnosis ^c			
Benign thyroid nodule, n (%)	100 (63.3)	35 (54.7)	65 (69.1)
Malignant thyroid nodule, n (%)	58 (36.7)	29 (45.3)	29 (30.9)

^aThyroid micronodule volume on ultrasound was ≤ 10 mm.

^bThyroid macronodule volume on ultrasound was > 10 mm.

^cConfirmed by surgical specimens.

E-strain: elastography strain; TI-RADS: Thyroid Imaging Reporting and Data System.

Table 2. Association between 2D-SWE thyroid nodule stiffness and the cytopathological Bethesda category

Nodule stiffness	Bethesda category				
	II	III	IV	V	VI
n = 158	92	12	7	44	3
kPa, median	18.0	21.5	24.0	27.5	33.0
kPa, mean	18.9	27.5	28.1	29.6	28.00
kPa, SD	6.3	20.4	14.4	11.5	10.4
kPa, minimum	7.0	9.0	14.0	5.0	16.0
kPa, maximum	35.0	80.0	59.0	64.0	35.0
kPa, IQ range	9.0	19.2	8.0	12.7	-

2D-SWE: two-dimensional shear wave elastography; kPa: kilopascals.

Table 3. 2D-SWE nodule stiffness of thyroid microcarcinomas with and without perinodular halo

Nodule stiffness	Nodule stiffness with a perinodular halo (n = 21)	Nodule stiffness without a perinodular halo (n = 8)
kPa, median	21.0	24.5
kPa, mean	21.3	23.8
kPa, minimum	16.0	22.0
kPa, maximum	30.0	25.0
kPa, lower limit 95% CI	17.4	19.8
kPa, upper limit 95% CI	25.3	27.8

2D-SWE: two-dimensional shear wave elastography; kPa: kilopascals; CI: confidence interval.

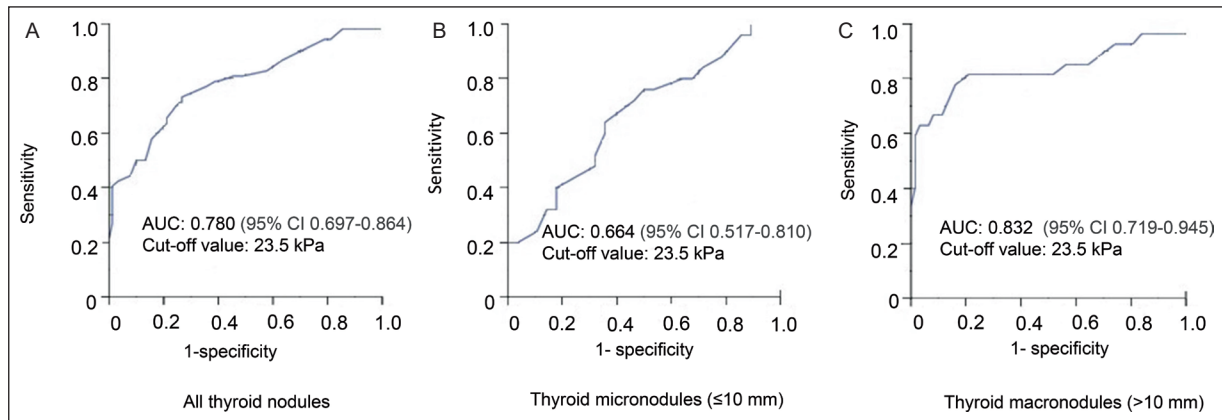


Figure 1. Diagnostic performance of the nodule stiffness cutoff values with 2D-SWE. ROC analyses show a comparison of the 23.5 kPa cutoff value in three groups. **A:** all thyroid nodules. **B:** thyroid micronodules (≤ 10 mm). **C:** thyroid macronodules (> 10 mm). The best performance of the nodule stiffness cutoff value (≥ 23.5 kPa) for predicting malignancy was found in thyroid macronodules (AUC: 0.832). In contrast, the 23.5 kPa cutoff value for thyroid micronodules had an AUC of 0.664.

AUC: area under the curve; CI: confidence interval; kPa: kilopascals; mm: millimeters; 2D-SWE: two-dimensional shear wave elastography; ROC: receiving operating characteristics.

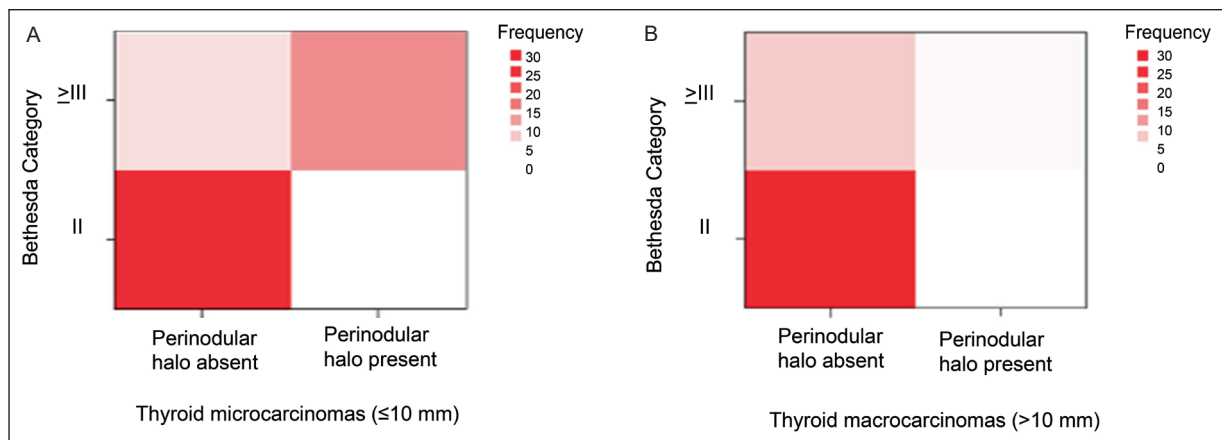


Figure 2. Heatmaps comparing the presence of a perinodular halo between thyroid microcarcinomas and macrocarcinomas using 2D-SWE. **A:** a perinodular halo was observed in microcarcinomas with Bethesda category $\geq III$ ($p < 0.001$). **B:** no association with perinodular halo was observed in thyroid macrocarcinomas.

2D-SWE: two-dimensional shear wave elastography.

and images were stored in the Picture Archiving and Communication System (PACS) (Carestream™, Health Inc., Rochester, NY, USA). The 2D-SWE color matrix was analyzed in two areas as defined by the authors (EC and MC). One area was obtained by placing the ROI in the intranodular parenchyma to determine the pure intrinsic stiffness of the nodule and the other was an extended area where the expanded ROI included intranodular tissue, capsule, and perinodular tissue of up to 2 mm outside the nodule boundary.

The size and location of the ROI were standardized. Before stabilizing and recording the image, we tried to

obtain the best image to recognize all the characteristics of conventional grayscale US. The immediate elastographic acquisition with the map and color matrix included the entire nodule and the greatest amount of thyroid tissue surrounding it and away from its edges. In 2D-SWE acquisitions, the ROI was manipulated to include the nodule and at least 2 mm of surrounding tissue. A second ROI was located exclusively within the nodule. The reliability of elastography measurements was assessed using quality and propagation maps. Two radiologists (EC and MLC) with 35 and 6 years of experience performed the evaluations in double reading.

Thyroid biopsy

The thyroid nodule pathological diagnoses were categorized by FNAB according to the Bethesda System for Reporting Thyroid Cytopathology⁷. The material obtained was interpreted by a cytopathologist (LG) with 35 years of experience. The pathological diagnosis was confirmed by surgery.

Statistical analysis

The mean, standard deviation, minimum, maximum, and median were calculated for quantitative variables. The chi-square test or Fisher's exact test was used for categorical variables. Thyroid nodule size and its association with malignancy were analyzed using the Student's t-test and the Mann-Whitney U-test. The association between thyroid nodule stiffness by 2D-SWE and cytopathological Bethesda category was evaluated with the Shapiro-Wilk normality test. Receiving operating characteristics (ROC) curves with the area under the curve (AUC) defined the cutoff value for predicting malignancy of micronodules and macronodules. A p-value of < 0.05 was considered significant. The SPSS software version 25 (IBM Corp., Armonk, NY, USA) was used.

RESULTS

A total of 172 patients with thyroid nodules were evaluated, of whom 14 cases were excluded because FNAB samples were insufficient (n = 9) or surgical pathology results were unavailable (n = 5). Thus, 158 patients with 158 thyroid nodules were included. There were 131 women (82.9%) and 27 men (17.1%) with a mean age of 47.04 ± 14 years (range 13-85). A comparison of 64 micronodules and 94 macronodules with the TI-RADS, E-strain, and Bethesda system is shown in Table 1. Malignancy was confirmed in 58 (36.7%) of 158 nodules, of which 29 were thyroid microcarcinomas. The mean diameter of the microcarcinomas in US was $4.5 \text{ mm} \pm 0.9 \text{ mm}$. An E-strain pattern of 4 or 5 was found in 26 (89.6%) of the 29 microcarcinomas.

Thyroid nodule stiffness by 2D-SWE and cytopathological Bethesda category

The relationship between nodule stiffness by 2D-SWE and cytopathological findings is shown in Table 2. Bethesda II thyroid nodules had a median value of 18.0 kPa, Bethesda IV had 24.0 kPa, Bethesda V had 27.5 kPa, and Bethesda VI had 33.0 kPa ($p < 0.001$).

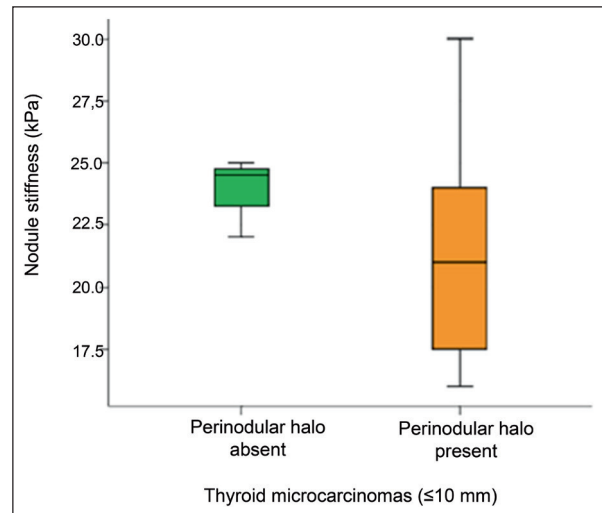


Figure 3. Boxplot showing the relationship between perinodular halo and nodular stiffness of thyroid microcarcinomas quantified by 2D-SWE. A perinodular halo was related to lower nodule stiffness values (softer micronodules).

2D-SWE: two-dimensional shear wave elastography.

Elastographic analysis showed higher stiffness values directly related to Bethesda categories III, IV, and V. Benign thyroid nodules had a median value of 12 ± 9.8 kPa. Malignant micronodules showed a median value of 25 ± 6.2 kPa compared to 32.9 ± 13.8 kPa for macronodules. 2D-SWE showed a wide range of values (5-64 kPa) for malignant macronodules. In contrast, a narrow range (18-35 kPa) was observed in benign nodules.

Diagnostic performance of the nodule stiffness cutoff value with 2D-SWE

ROC analyses for predicting malignancy based on thyroid nodule stiffness are shown in a three-group comparison: all thyroid nodules, micronodules, and macronodules (Figure 1). The cutoff value for nodule stiffness was 23.5 kPa to predict malignancy. Thyroid macronodules showed an AUC of 0.832 (95% CI 0.719-0.945), a sensitivity of 81.5%, and a specificity of 79.4%. In contrast, a cutoff value of 23.5 kPa for thyroid micronodules had an AUC of 0.664 (95% CI 0.517-0.810) with a sensitivity of 60.0% and a specificity of 35.7%.

Perinodular halo by 2D-SWE

The heatmaps in Figure 2 show the strong association between a rigid perinodular halo in thyroid microcarcinomas and Bethesda category III, IV, or V ($p < 0.001$).

Table 4. Comparison of the elastographic A/B index^a by 2D-SWE in thyroid microcarcinomas with and without a perinodular halo

Thyroid microcarcinomas with perinodular halo, A/B index (n = 21)	Case 1	Case 2	Case 3	Case 4	Case 5	Case 6	Case 7	Case 8	Case 9	Case 10	Case 11
	1.35	1.33	1.40	1.33	1.34	1.55	1.70	1.73	1.80	1.40	1.95
	Case 12	Case 13	Case 14	Case 15	Case 16	Case 17	Case 18	Case 19	Case 20	Case 21	
	2.20	1.50	1.44	1.30	1.73	1.58	1.45	1.87	1.64	1.33	
Thyroid microcarcinomas without a perinodular halo, A/B index ^b (n = 8)	Case 1	Case 2	Case 3	Case 4	Case 5	Case 6	Case 7	Case 8			
	0.04	0.9	1.1	0.05	0.8	1.08	0.88	0.75			

^aA/B index: (A) corresponds to the stiffness of an expanded ROI that includes the nodule + perinodular halo (up to 2 mm outside the limit of the nodule). (B) corresponds to the region of interest (ROI) of nodule stiffness; ^bThe A/B index was only defined with the ROI of nodule stiffness. 2D-SWE: two-dimensional shear wave elastography.

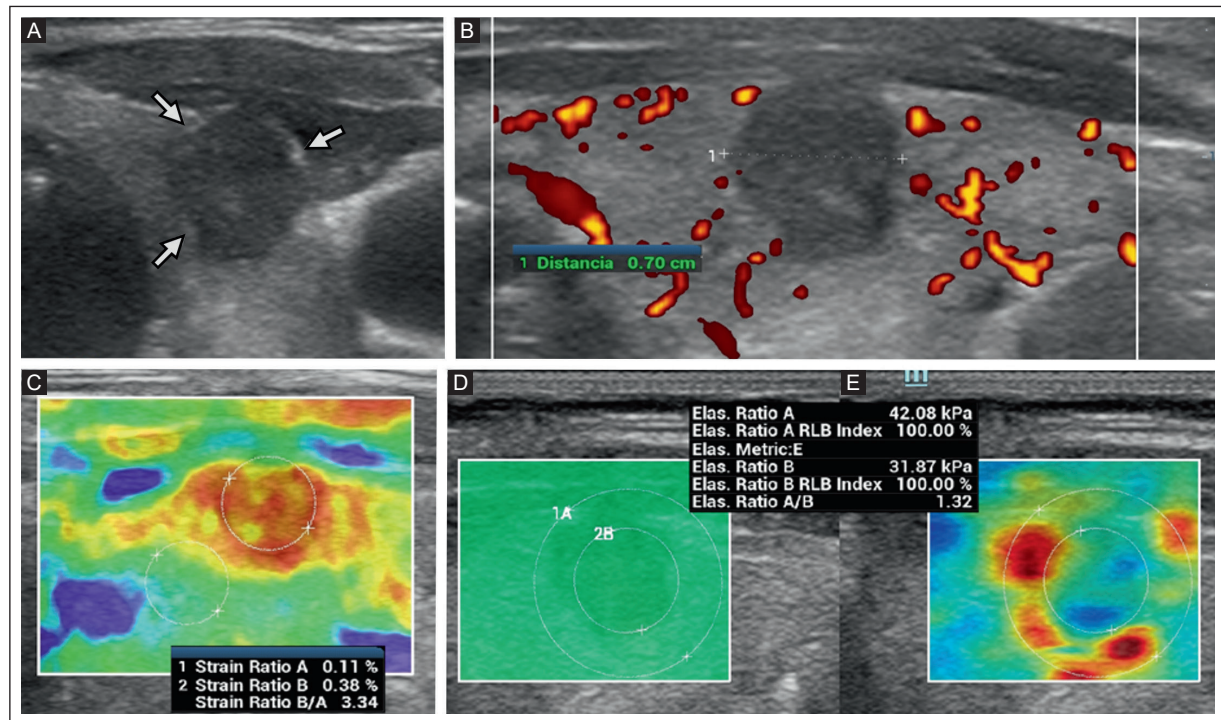


Figure 4. A 30-year-old woman with clinical symptoms of hypothyroidism and neck pain. **A:** grayscale US shows a 7-mm solid, hypoechoic micronodule, taller than wide, with a lobulated margin and peripheral microcalcifications (arrows). TI-RADS 5. **B:** color Doppler US with an absent intrinsic vascular signal and isolated, short, irregular peripheral vascular poles. **C:** E-strain without deformation (red map) and an area extending beyond the edge of the nodule (pattern 5). **D:** 2D-SWE quality map with a homogeneous green box confirming good acquisition. **E:** 2D-SWE color matrix showing a nodule with relative central nodular laxity (31 kPa) and a rigid perinodular halo (42 kPa). The A/B index was 1.32. The FNAB was the Bethesda V category. The histopathological diagnosis was papillary thyroid microcarcinoma.

E-strain: elastography strain; FNAB: fine needle aspiration biopsy; kPa: kilopascals; TI-RADS: Thyroid Imaging Reporting and Data System; US: ultrasound; 2D-SWE: two-dimensional shear wave elastography.

in contrast to the absence of a perinodular halo in macrocarcinomas. Table 3 shows the association of nodule stiffness and perinodular halo in thyroid microcarcinomas using 2D-SWE. Notably, 21 (72.4%) of the

29 microcarcinomas with a perinodular halo had a median nodule stiffness of 21.0 kPa. In contrast, the median of 8 microcarcinomas without a perinodular halo was 24.5 kPa ($p < 0.001$) (Figure 3).

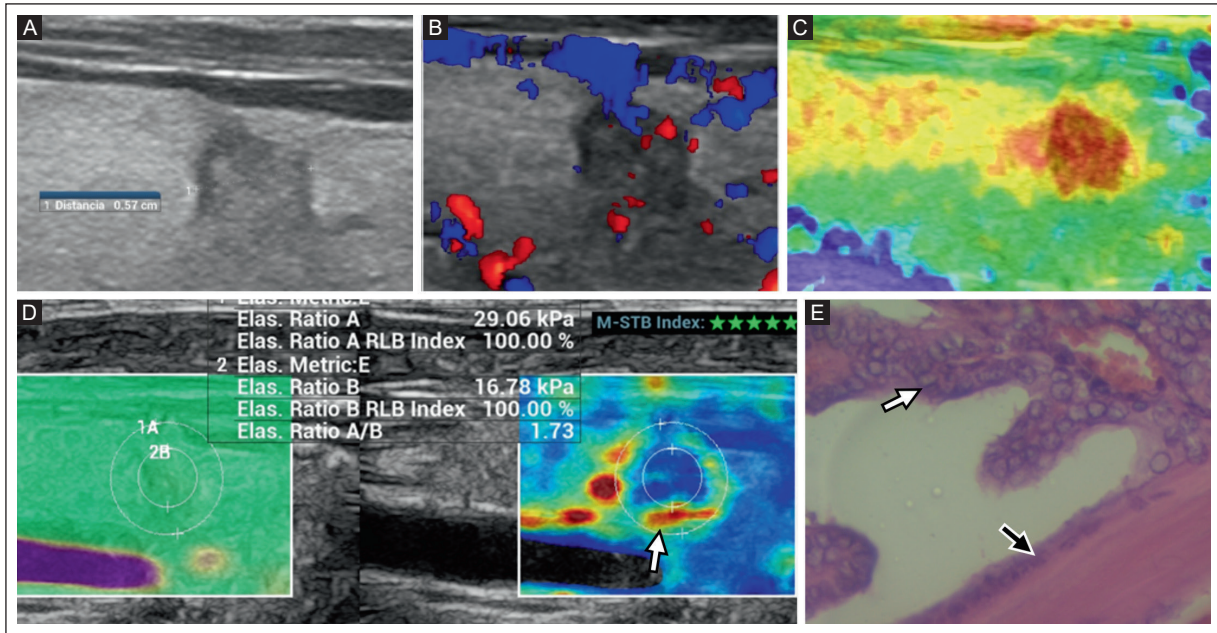


Figure 5. A 27-year-old woman with diabetes and a thyroid micronodule. **A:** grayscale US shows a 5-mm solid, hypoechoic, rounded micronodule with an angular margin. TI-RADS 4. **B:** a color Doppler US shows irregular vascular poles. **C:** E-strain shows pattern 4 (red) without compression deformation. **D:** 2D-SWE color matrix where nodular laxity is observed with a rigid perinodular halo (arrow). The relationship between A (29.1 kPa), configured by halo and nodule, and B (16.8 kPa), corresponding to the intrinsic stiffness of the nodule, results in an A/B index of 1.73. The FNAB was the Bethesda V category. **E:** surgical specimen (40× H&E) shows a thick capsule of scleral hyaline fibrous connective tissue (black arrow), accompanied by papillary protrusions (white arrow), lined by follicular cells, with overlapping and stacked nuclei, nuclear clefts, pseudo-inclusions, and nuclear folds (grooves). The histopathological diagnosis was papillary thyroid microcarcinoma.

E-strain: elastography-strain; FNAB: fine needle aspiration biopsy; H&E: hematoxylin-eosin; kPa: kilopascals; TI-RADS: Thyroid Imaging Reporting and Data System; US: ultrasound; 2D-SWE: two-dimensional shear wave elastography.

Elastographic stiffness by A/B index

A comparison of the elastographic stiffness index using 2D-SWE in thyroid microcarcinomas with and without a perinodular halo is shown in Table 4. The A/B index of microcarcinomas with a perinodular halo was 1.56 ± 0.23 , compared to those without a halo (0.7 ± 0.39). A stiffness A/B index ≥ 1.3 was found in all microcarcinomas with a perinodular halo ($n = 21$, 100%). Figures 4–7 are examples of 2D-SWE features, E-strain, and conventional US with TI-RADS 4 or 5, respectively.

Elastographic patterns of thyroid microcarcinomas

Although the study's sample size was small, we consider it feasible to propose the integration of 2D-SWE features, E-strain, and conventional US with TI-RADS 4 or 5 to define three elastographic patterns of thyroid microcarcinomas (Table 5; Figure 8).

Congruent elastographic pattern: concordance of conventional US with TI-RADS 4 or 5, E-strain with pattern 4 or 5, and 2D-SWE with nodule stiffness ≥ 23.5 kPa without a perinodular halo and an A/B index < 1.3 .

Incongruent elastographic pattern: conventional US with TI-RADS 4 or 5, E-strain with pattern 4 or 5, and discordant findings on 2D-SWE with intrinsic thyroid nodule laxity (< 23.5 kPa), the presence of a rigid perinodular halo, and an A/B index ≥ 1.3 .

Atypical congruent elastographic pattern: conventional US with TI-RADS 4 or 5, atypical findings on E-strain with patterns 1, 2, or 3, and 2D-SWE with intrinsic nodular laxity (< 23.5 kPa), the presence of a rigid perinodular halo, and an A/B index ≥ 1.3 .

These three patterns highlight the importance of assessing the nodular and perinodular stiffness of the tissue using the 2D-SWE color matrix, which may have a different expression depending on the size of the nodule, its intrinsic structural composition, and desmoplastic changes.

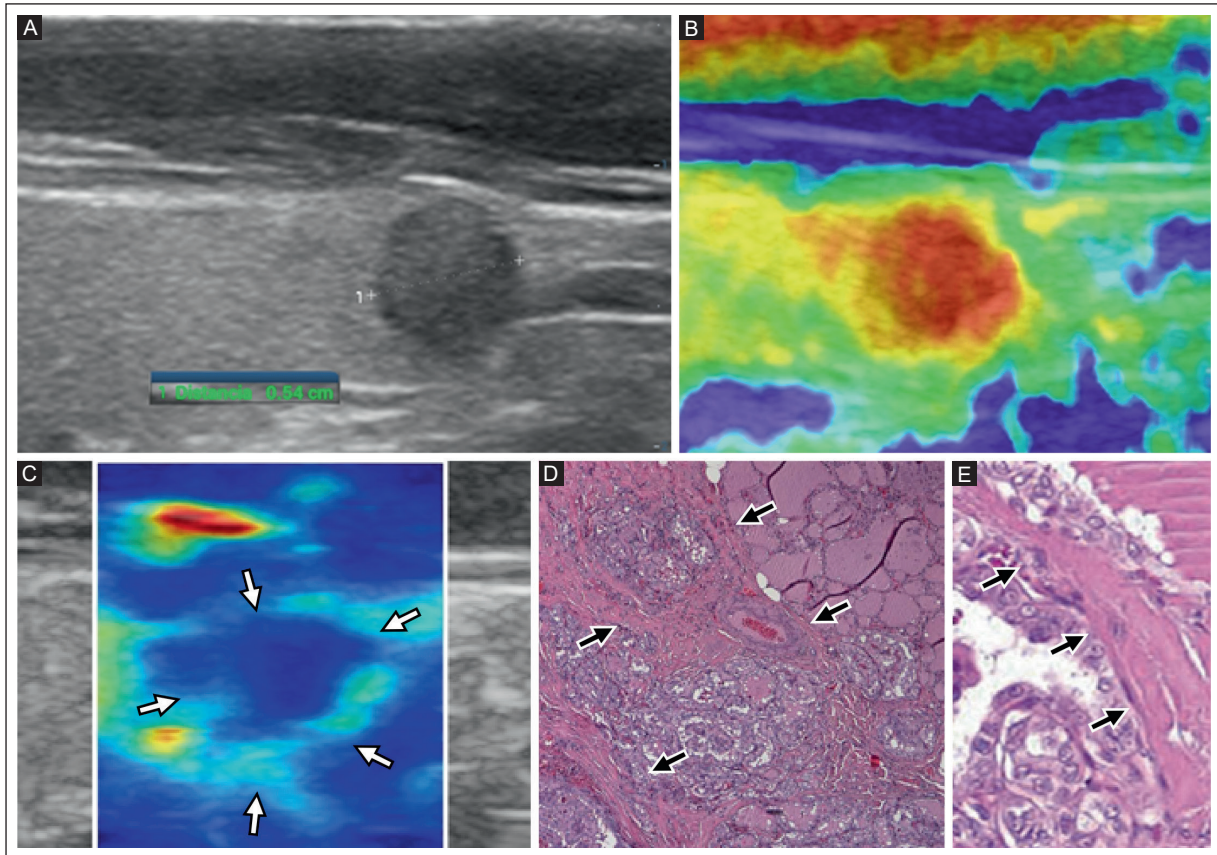


Figure 6. A 35-year-old asymptomatic man with an incidental thyroid nodule. **A:** grayscale US shows a 5-mm solid, hypoechoic, round, homogeneous micronodule with a lobulated margin. TI-RADS 4. **B:** E-strain shows the nodule without deformation (red), pattern 4. **C:** the 2D-SWE color matrix shows a nodule stiffness of 12 kPa (blue color) bordered by a perinodular stiffness halo of 18 kPa (arrows). The A/B index was 1.5. The FNAB was the Bethesda V category. **D:** surgical specimen (40× H&E) with a significant reaction of the desmoplastic stroma (arrows) surrounding the nests of intratumoral cells. **E:** peritumoral desmoplastic reaction (arrows). The histopathological diagnosis was papillary thyroid microcarcinoma.

E-strain: elastography-strain; FNAB: fine needle aspiration biopsy; kPa: kilopascals; H&E: hematoxylin-eosin; TI-RADS: Thyroid Imaging Reporting and Data System; US: ultrasound; 2D-SWE: two-dimensional shear wave elastography.

DISCUSSION

This study showed that the combination of 2D-SWE features such as nodule stiffness, perinodular halo, A/B index, and matrix color has a differential expression in thyroid microcarcinomas. Three elastographic patterns, namely, congruent, incongruent, and atypical congruent, are based on the thyroid microcarcinoma findings by conventional US, E-strain, and 2D-SWE. These elastographic patterns have not been described in the literature.

Thyroid nodule stiffness has been related to cell density, colloid content, and intrinsic and perinodular fibrosis. Therefore, the tissue stiffness variability measured by 2D-SWE may reflect the heterogeneous architecture and density of fibrillar collagen in thyroid nodules. Duan et al.⁹ recommended the quantitative

2D-SWE assessment for diagnosing thyroid microcarcinoma, but their study did not include 2D-SWE color matrix assessment or conventional US findings. On the other hand, Zhang et al.¹⁰ and Hu et al.¹¹ evaluated the 2D-SWE color matrix to quantify nodule stiffness and emphasized the relevance of elastographic characteristics of the tissue at the edge of the nodule. We propose three elastographic patterns that optimize the use of elastographic features of thyroid microcarcinomas with different biological behaviors. The congruent elastographic pattern is characterized by the concordance of conventional US with TI-RADS 4 or 5, E-strain without deformation (pattern 4 or 5), and 2D-SWE with a nodule stiffness ≥ 23.5 kPa without a perinodular halo, and an A/B index < 1.3 . Intrinsic nodule stiffness can predict malignant thyroid microcarcinoma.

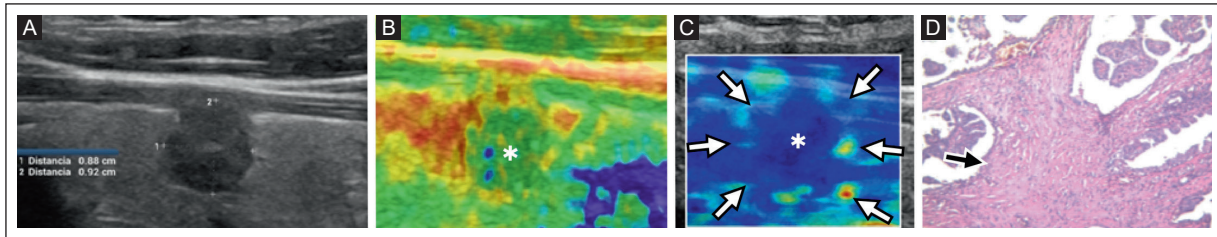


Figure 7. A 28-year-old woman with a family history of thyroid cancer. **A:** grayscale US examination shows a 8-mm solid, hypoechoic, taller than wide, micronodule with an irregular and lobulated margin. TI-RADS 5. **B:** E-strain shows a discrete reverberation (red) surrounding the micronodule (asterisk), which has a color map pattern 1 (green) with a non-deformable perimeter ring (yellow). **C:** 2D-SWE color matrix with nodule stiffness of 9 kPa (asterisk) and a rigid perinodular halo (arrows), with 13 kPa and an A/B index of 1.44. The FNAB was the Bethesda V category. **D:** surgical specimen (400× H&E) shows the tumor matrix with papillary protrusions lined by follicular cells with abundant acellular fibrosclerosis (arrow). The histopathological diagnosis was papillary thyroid microcarcinoma.

E-strain: elastography strain; FNAB: fine needle aspiration biopsy; H&E: hematoxylin-eosin; kPa: kilopascals; TI-RADS: Thyroid Imaging Reporting and Data System; US: ultrasound; 2D-SWE: two-dimensional shear wave elastography.

Table 5. Thyroid microcarcinoma elastographic patterns according to conventional US with TI-RADS 4 or 5, E-strain, and 2D-SWE

Description	TI-RADS category	E-strain pattern	2D-SWE		
			Thyroid nodule stiffness (kPa)	Perinodular halo	A/B index ^a
Congruent elastographic pattern	4 or 5	4 or 5	≥ 23.5	Absent	< 1.3
Incongruent elastographic pattern	4 or 5	4 or 5	< 23.5	Present	≥ 1.3
Atypical congruent elastographic pattern	4 or 5	1, 2 or 3	< 23.5	Present	≥ 1.3

^aA/B index: (A) corresponds to the stiffness of an expanded region of interest (ROI) that includes the nodule + perinodular halo (up to 2 mm outside the limit of the nodule), and (B) corresponds to the ROI of nodule stiffness; TI-RADS: Thyroid Imaging Reporting and Data System; kPa: kilopascals; E-Strain: elastography strain; 2D-SWE: two-dimensional shear wave elastography; US: ultrasound.

In contrast, the incongruent elastographic pattern was found in fibrosclerotic lesions with a perimetral desmoplastic reaction associated with apparent intrinsic softness of the nodule and a rigid perinodular halo, with an A/B index ≥ 1.3 , and E-strain without deformation (pattern 4 or 5). The apparent laxity of thyroid microcarcinomas may suggest benignity if only tissue stiffness is assessed. In contrast, microcarcinomas with an atypical congruent elastographic pattern were visualized with E-strain “mirrored with 2D-SWE color matrix,” i.e., apparent intrinsic nodular laxity with a rigid perinodular halo in both elastographic modalities and conventional US with TI-RADS 4 or 5. The histopathological features of this elastographic pattern showed infiltrative behavior of adjacent tissue and angiolymphatic invasion with peripheral desmoplasia that restricts the elastogram. 2D-SWE features such as thyroid nodule stiffness quantification, the presence of a perinodular halo, and color matrix features to determine the halo/nodule A/B index can be evaluated in patients with thyroid micronodules and may be useful for diagnosing thyroid microcarcinoma.

There is no defined cutoff value for tissue stiffness measured by 2D-SWE to differentiate between benign and malignant thyroid nodules¹¹. It has been suggested that stiffness is lower in thyroid micronodules than macronodules¹. Published studies report a wide range of stiffness values between 19 and 85 kPa.^{1,2,11-16} This wide range may be related to differences in the equipment, volume, and histological type of the thyroid nodule. In our study, the accuracy of the ≥ 23.5 kPa cutoff value of nodule stiffness was higher in macrocarcinomas (AUC 0.832) than in microcarcinomas (AUC 0.664). 2D-SWE appears to have lower diagnostic accuracy in microcarcinomas, especially those with apparent intrinsic softness (< 23.5 kPa) that have a rigid perinodular halo. Based on our results, we believe that in the assessment of thyroid micronodules, nodule stiffness quantification using 2D-SWE should be combined with other elastographic features such as perinodular halo, A/B index, and color matrix to increase the accuracy of thyroid microcarcinoma diagnosis.

Few published studies analyze the diagnostic relevance of the rigidity of the perinodular halo for the

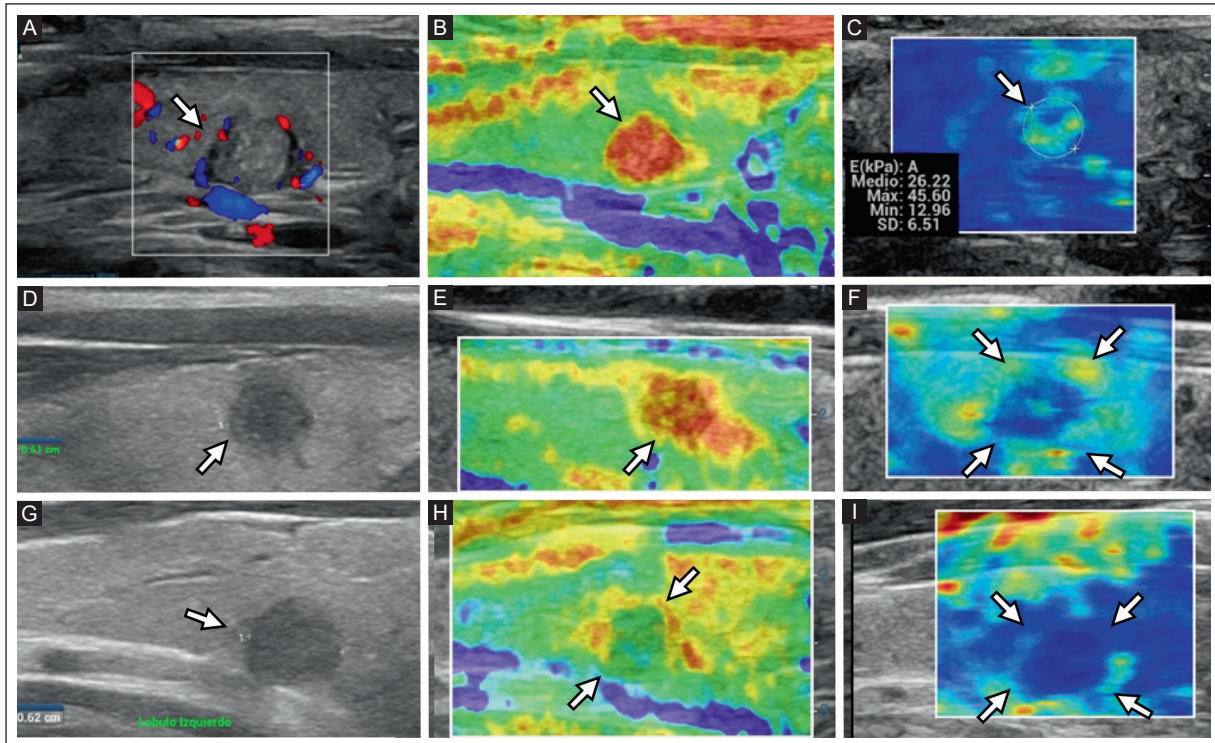


Figure 8. Three proposed elastographic patterns based on combined grayscale US, E-strain, and 2D-SWE features. *Congruent elastographic pattern (upper panel)* **A:** grayscale US showing a 6-mm solid, hypoechoic (arrow), rounded micronodule with an irregular margin and calcifications with peripheral vessels. TI-RADS 5. **B:** E-strain without deformation (pattern 4). The color map shows an intense red nodule (arrow). **C:** 2D-SWE color matrix shows ROI (arrow) with a nodular stiffness of 26.2 kPa. A perinodular halo is not present. The FNAB was the Bethesda V category. The histopathological diagnosis was papillary thyroid microcarcinoma. *Incongruent elastographic pattern (middle panel)* **D:** grayscale US shows a 6-mm solid, hypoechoic, rounded micronodule with an irregular margin (arrow). TI-RADS 5. **E:** E-strain without deformation (pattern 4) shows a red nodule (arrow). **F:** 2D-SWE color matrix shows a blue nodule with a stiffness of 15 kPa and a rigid ring represented by a light blue halo with orange-red spots (27 kPa) (arrows). The A/B index was 1.8. The FNAB was the Bethesda III category. The histopathological diagnosis was papillary thyroid microcarcinoma. *Atypical congruent elastographic pattern (lower panel)* **G:** grayscale US shows a 6-mm solid, hypoechoic, rounded micronodule with an irregular margin (arrow) with extrathyroidal extension with border abutment, contour bulging, or loss of the echogenic thyroid border, TI-RADS 5. **H:** E-strain pattern 1 of the micronodule (green core) with a thin, non-deformable (red) perinodular halo (arrows). The strong stiffness of the halo restricts the intrinsic expression of nodule stiffness. **I:** 2D-SWE with a nodule stiffness of 12.0 kPa, color matrix with a blue nodule (apparent intrinsic laxity), and a light blue perinodular halo (arrows). The A/B index was 1.33. The FNAB was the Bethesda V category. The histopathological diagnosis was papillary thyroid microcarcinoma.

E-strain: elastography strain; FNAB: fine needle aspiration biopsy; kPa: kilopascals; ROI: region of interest; TI-RADS: Thyroid Imaging Reporting and Data System; US: ultrasound; 2D-SWE: two-dimensional shear wave elastography.

differential diagnosis of benign and malignant thyroid nodules^{1,6}. In our study, perinodular halo stiffness was significantly higher in malignant nodules than in benign nodules. We hypothesize that a rigid perinodular halo modifies elastographic behavior and can dissemble or reduce the intrinsic rigidity of microcarcinomas. In several malignant thyroid micronodules, maximum stiffness was observed in the perinodular region and not in the lesion. Microcarcinomas, in which there was a halo, appeared intrinsically softer. The inaccuracy of 2D-SWE in microcarcinomas with apparent intrinsic softness is compensated by analyzing the 2D-SWE color matrix to quantify intra- and perinodular stiffness,

with the determination of the halo/nodule elastographic index (A/B index). In this context, it is possible that the degree of perinodular fibrosis disturbs the real intrinsic plasticity of the nodule and consequently modifies the expression of the 2D-SWE color matrix, and the quantitative value of stiffness.

The strengths of this study include the fact that all benign and malignant thyroid nodules were targeted using FNAB, which is the reference standard, and were evaluated with conventional US and two complementary elastographic modalities by experienced neck radiologists. Study limitations include the retrospective, single-center design, and a small sample

size. The follow-up to determine the clinical behavior associated with the proposed elastographic patterns has not been included. On the other hand, no comparisons of elastographic patterns with macronodules have been made. Although the quantification data are objective, interobserver and intraobserver agreement was not determined, which is important considering that elastography has operator-dependent variability. Although 2D-SWE depends less on the operator, some factors can affect the spread through the tissue, so it is recommended to apply objective parameters and quality indicators and seek good training and experience in order to issue ultrasound elastography reports.

CONCLUSION

The three elastographic patterns are based on the combination of conventional US, E-strain patterns, and data provided by 2D-SWE by quantifying nodule stiffness, the presence of a perinodular halo, and characteristics of the color matrix to determine the A/B index (halo/nodule). The three elastographic patterns can be useful for diagnosing thyroid microcarcinoma, especially in cases with TI-RADS 4 or 5 and indeterminate cytopathology. US elastography is painless and requires only a few additional minutes without special preparation for patients. Further research is needed to confirm the results of this study and evaluate the diagnostic performance of elastographic patterns in large multi-center prospective cohort studies.

Acknowledgments

The authors thank Professor Ana M. Contreras-Navarro for her guidance in preparing and writing this scientific paper. We also appreciate the support of the Endocrinology Service of the National Hospital of Clinics – Faculty of Medical Sciences of the National University of Cordoba and the Society of Endocrinology and Metabolism of the Province of Cordoba, Argentina.

Funding

This research received no external funding.

Conflicts of interest

The authors declare no conflicts of interest.

Ethical disclosures

Protection of individuals. This study complies with the Declaration of Helsinki (1964) and its amendments.

Confidentiality of data. The authors declared that they followed their center's protocol for sharing patient data.


Right to privacy and informed consent. Informed consent was not required for this observational study of information collected during routine clinical care.

Use of artificial intelligence. The authors state that they did not use generative artificial intelligence to prepare this manuscript and/or create tables, figures, or figure legends.

REFERENCES

1. Tan S, Sun PF, Xue H, Fu S, Zhang ZP, Mei F, et al. Evaluation of thyroid micro-carcinoma using shear wave elastography: Initial experience with qualitative and quantitative analysis. *Eur J Radiol.* 2021;137:109571. doi:10.1016/j.ejrad.2021.109571.
2. Zhao CK, Xu HX. Ultrasound elastography of the thyroid: principles and current status. *Ultrasonography.* 2019;38(2):106-124. doi: 10.1016/j.ultras.2014.04.027.
3. Faquin WC, Baloch ZW. Fine-needle aspiration of follicular patterned lesions of the thyroid: Diagnosis, management, and follow-up according to National Cancer Institute (NCI) recommendations. *Diagn Cytopathol.* 2010; 38(10):731–739. doi: 10.1002/dc.21292.
4. Mehrotra P, McQueen A, Kolla S, Johnson SJ, Richardson DL. Does elastography reduce the need for thyroid FNAs? *Clin Endocrinol (Oxf).* 2013; 78(6):942–949. doi: 10.1111/cen.12077.
5. Wang Y, Dan HJ, Dan HY, Li T, Hu B. Differential diagnosis of small single solid thyroid nodules using real-time ultrasound elastography. *J Int Med Res.* 2010;38(2):466-72. doi: 10.1177/147323001003800210.
6. Hu L, He NA, Xie L, Ye X, Liu X, Pei C, et al. Evaluation of the Perinodular Stiffness Potentially Predicts the Malignancy of Thyroid Nodules. *J Ultrasound Med.* 2020; 39(11):2183-2193. doi: 10.1002/jum.15329.
7. Civas ES, Ali SZ. The Bethesda System for Reporting Thyroid Cytopathology. *Am J Clin Pathol.* 2009;132:658-665. doi: 10.1309/AJCPPLW-MI3JV4LA.
8. Rago T, Vitti P. Role of thyroid ultrasound in the diagnostic evaluation of thyroid nodules. *Best Pract Res Clin Endocrinol Metab.* 2008; 22(6):913-928. doi:10.1016/j.beem.2008.09.016.
9. Duan SB, Yu J, Li X, Han ZY, Zhai HY, Liang P. Diagnostic value of two-dimensional shear wave elastography in papillary thyroid microcarcinoma. *Oncol Targets Ther.* 2016;9(9):1311-1317. doi: 10.2147/OTT.S98583.
10. Zhang YX, Xue JP, Li HZ, Miao JW, Kang CS. Clinical Value of Shear Wave Elastography Color Scores in Classifying Thyroid Nodules. *Int J Gen Med.* 2021;14:8007-8018. doi: 10.2147/IJGM.S331406.
11. Hu L, He N, Ye L, Zhou H, Zhong W, Zhang X. Evaluation of the Stiffness of Tissues Surrounding Thyroid Nodules with Shear Wave Elastography. *J Ultrasound Med.* 2018; 37(9):2251-2261. doi: 10.1002/jum.14578.
12. Liang XW, Cai YY, Yu JS, Liao JY, Chen ZY. Update on thyroid ultrasound: a narrative review from diagnostic criteria to artificial intelligence techniques. *Chin Med J (Engl).* 2019;132(16):1974-1982. doi: 10.1097/CM9.0000000000000346.
13. Kim H, Kim JA, Son EJ, Youk JH. Quantitative assessment of shear-wave ultrasound elastography in thyroid nodules: diagnostic performance for predicting malignancy. *Eur Radiol.* 2013;23(9):2532–2537. doi: 10.1007/s00330-013-2847-5.
14. Moon HJ, Kim EK, Yoon JH, Kwak JY. Clinical implication of elastography as a prognostic factor of papillary thyroid microcarcinoma. *Ann Surg Oncol.* 2012;19(7):2279–2287. doi: 10.1245/s10434-011-2212-3.
15. Fukuhara T, Matsuda E, Fujiwara K, Tanimura C, Izawa S, Kataoka H, et al. Phantom experiment and clinical utility of quantitative shear wave elastography for differentiating thyroid nodules. *Endocr J.* 2014;61(6):615-621. doi:10.1507/endocrj.ej14-0061.
16. Zhang YX, Xue JP, Li HZ, Miao JW, Kang CS. Clinical Value of Shear Wave Elastography Color Scores in Classifying Thyroid Nodules. *Int J Gen Med.* 2021;14:8007-8018. doi: 10.2147/IJGM.S331406.

Imaging and clinical features of breast cancer in young Mexican women: long delay between self-detection and seeking medical attention

Karen A. Rojas-Galeana^{1*}, Benjamin Conde-Castro², Nancy B. Guzman-Martinez¹,
Anallely Moctezuma-Oropeza³, and Beatriz Alvarez-Alonso³

¹Department of Mastography, ABC Medical Center; ²School of Medicine, Universidad Nacional Autonoma de Mexico; ³Department of Mastography, Hospital Juarez de Mexico. Mexico City, Mexico

ABSTRACT

Introduction: The interval between self-detection of clinical signs during breast self-examination and seeking medical attention in young women (< 40 years old) with breast cancer has not been evaluated in the Mexican population. There are also limited data on specific imaging findings. This study aimed (1) to determine the interval between self-detection of clinical signs and seeking medical attention in young Mexican women (< 40 years old) with breast cancer and (2) to describe the imaging ultrasound (US) and mammographic findings and clinical characteristics. **Materials and Methods:** A cross-sectional study included young women (< 40 years old) who self-detected clinical signs of histologically confirmed breast cancer and were examined with US grayscale and Doppler color, and mammography. Clinical signs such as a palpable lump, bloody discharge from the nipple or nipple retraction, and enlarged breast volume were recorded. The BI-RADS categories were used for evaluation. The interval between self-detection of clinical signs and seeking medical attention was also recorded. **Results:** A total of 43 patients aged 33.8 ± 4.5 years (range 21-39 years) were included. Most patients ($n = 30, 69.8\%$) had more than 90 days between self-detection of a breast sign and seeking medical attention, with a mean of 300 ± 7.8 days (range 30-1080 days). A palpable lump was the most common self-detected clinical sign in 37 (86.0%) patients. US and mammography showed BI-RADS 4 and 5 lesions suspicious of malignancy in all patients. Invasive ductal carcinoma was the most common ($n = 37, 86.0\%$). **Conclusion:** This is the first study in young Mexican women (< 40 years old) with breast cancer that showed a long delay between self-detection of clinical signs and seeking medical attention. US and mammography findings of breast cancer were comparable with other older populations.

Keywords: Breast cancer. Young women. Breast US. Mammography. Delayed diagnosis.

INTRODUCTION

A delayed breast cancer diagnosis in young women (< 40 years old) is associated with a more advanced clinical stage and a poor prognosis¹⁻³. A delay of more than 90 days between self-detection and seeking medical attention is associated with a more advanced

stage¹⁻³. Ultrasound (US) is the recommended imaging modality in women < 40 years of age when breast abnormalities are detected during breast self-examination. Other imaging modalities, such as mammography and magnetic resonance imaging (MRI), are used as complementary diagnostic evaluations for suspected malignancy⁴.

*Corresponding author:

Karen A. Rojas-Galeana
E-mail: dra.karenandream@gmail.com

Received for publication: 13-01-2024
Accepted for publication: 18-03-2024
DOI: 10.24875/JMEXFRI.M24000076

Available online: 10-07-2024
J Mex Fed Radiol Imaging. 2024;3(2):93-104
www.JMeXFRI.com

2696-8444 / © 2024 Federación Mexicana de Radiología e Imagen, A.C. Published by Permanyer. This is an open access article under the CC BY-NC-ND (<https://creativecommons.org/licenses/by-nc-nd/4.0/>).

Table 1. Characteristics of 43 young Mexican women (< 40 years old) with breast cancer

Description	Parameters
Age, years, mean ± SD (min, median, max)	33.8 ± 4.5 (21, 34, 39)
School education	
Illiterate, n (%)	1 (2.3)
Basic education, n (%)	22 (51.1)
High education, n (%)	15 (35.0)
Bachelor's degree, n (%)	5 (11.6)
Lactation, yes, n (%)	27 (63.0)
Family history of breast cancer, yes, n (%)	12 (28.0)
Smoking, yes, n (%)	11 (26.2)
Alcoholism, yes, n (%)	10 (23.4)
The delay between self-detection of clinical signs and seeking medical attention ^a , mean ± SD (min, median, max)	300 ± 7.8 (30, 240, 1080)
More than 90 ^a days, n (%)	30 (69.8)
Less than 90 days, n (%)	13 (30.2)
Self-detected clinical signs ^a	
Lump and blood discharge from the nipple, n (%)	19 (44.2)
Lump, n (%)	18 (41.8)
Enlarged breast volume, n (%)	4 (9.4)
Blood discharge from the nipple, n (%)	1 (2.3)
Nipple retraction, n (%)	1 (2.3)
Clinical stage ^b , n (%)	
0	3 (6.9)
IIA	6 (14.0)
IIB	14 (32.5)
IIIA	12 (28.0)
IIIB	3 (6.9)
IIIC	1 (2.3)
IV	4 (9.4)

^aBreast abnormalities detected during breast self-examination; ^bAmerican Joint Committee of Cancer.

Table 2. US findings (n = 43) according to BI-RADS in young Mexican women (< 40 years old) with breast cancer

Descriptor	n (%)
Shape	
Oval	8 (18.6)
Round	0
Irregular	35 (81.4)
Orientation	
Parallel	24 (55.9)
Not parallel	19 (44.1)
Margin	
Circumscribed	8 (18.6)
Not circumscribed	
Spiculated	16 (37.2)
Angular	11 (25.6)
Microlobulated	7 (16.3)
Indistinct	1 (2.3)
Echo pattern	
Anechoic	0
Hyperechoic	0
Complex cystic and solid	7 (16.3)
Hypoechoic	33 (76.7)
Isoechoic	0
Heterogeneous	3 (7)
Posterior features	
No posterior features	13 (30.2)
Enhancement	7 (16.3)
Shadowing	23 (53.5)
Ductal changes	
Solitary dilated duct	7 (16.2)
Ductal extension	18 (41.9)
No ductal involvement	18 (41.9)

BI-RADS: Breast Imaging-Reporting and Data System, 5th Edition; US: ultrasound.

Villarreal et al.⁵ reported that the incidence and mortality rates for breast cancer in young Latin American women were higher than in developed countries (20.0% versus 12.0% and 14.0% versus 7.0%, respectively). The prognosis in young women (< 40 years old) with breast cancer is particularly unfavorable in developing countries such as Mexico, with limited access to medical care and early treatment. As the standard recommendation for breast cancer screening starts at the age

of 40 years, breast abnormalities are usually detected by breast self-examination in young women < 40 years old. However, there is evidence that a long interval occurs between self-detection of clinical signs during breast self-examination and seeking medical attention³. This study aimed (1) to determine the interval between self-detection of clinical signs and seeking medical

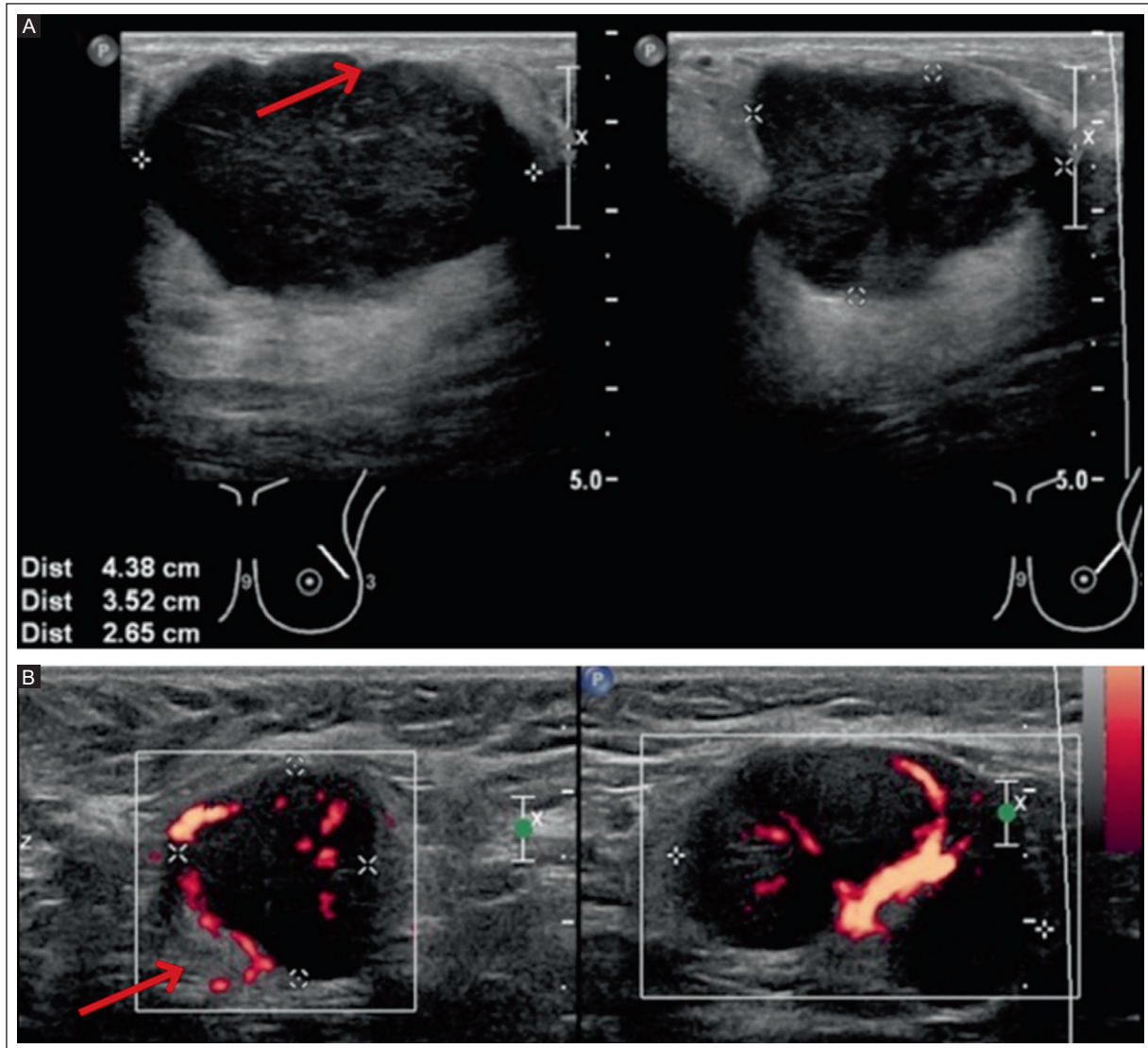


Figure 1. A 36-year-old woman with a palpable lump in the left breast and axilla for 3 months. **A:** US grayscale shows an irregular, parallel, microlobulated mass (arrow), radial and antiradial, hypoechoic with enhancement in the left breast at 2 o'clock. **B:** US Power Doppler shows an enlarged lymph node in the axillary region, with loss of morphology, cortical thickening displacing the fatty hilum, and transcapsular vascularity (arrow), BI-RADS 5. The histopathologic diagnosis was invasive ductal carcinoma with a triple-negative immunohistochemical profile. MRI with metastases in the central nervous system (not shown).

BI-RADS: Breast Imaging-Reporting and Data System; MRI: magnetic resonance imaging; US: ultrasound.

attention in young Mexican women aged < 40 years with breast cancer and (2) to describe the US and mammography findings and clinical characteristics.

MATERIALS AND METHODS

This cross-sectional study was conducted from January 2019 to December 2021 in the Department of Radiology and Imaging of the Hospital Juárez de México in Mexico City. Young Mexican women aged < 40 years who self-detected any clinical signs on breast self-examination and with histologically confirmed breast

cancer were included. Patients without complete breast imaging examinations or who had undergone breast surgery were excluded. Informed consent was not required for this retrospective analysis of data obtained during routine medical care. The Institutional Research Ethics Committee and the Research Committee approved the study.

Study and variable development

Histologically confirmed breast cancer cases of patients who had undergone grayscale and Doppler

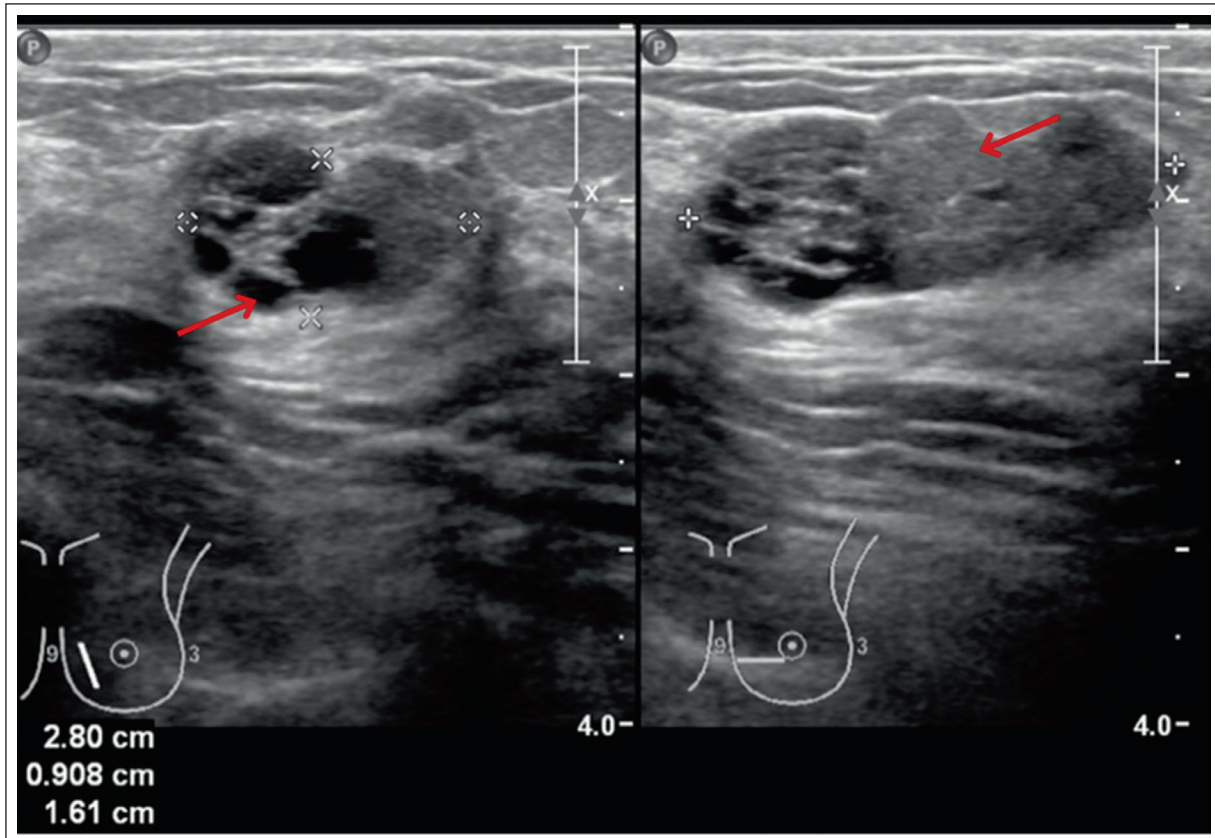


Figure 2. A 27-year-old woman with a palpable lump in the left breast that has been present for 1 month. US grayscale with a mass in the left breast at 8 o'clock, radial and antiradial, irregular, parallel, microlobulated, complex (arrows) with enhancement, BI-RADS 4B. The histopathologic diagnosis was an invasive ductal carcinoma with a luminal A immunohistochemical profile.

US: ultrasound; BI-RADS: Breast Imaging-Reporting and Data System.

color US examination and mammography were selected from the institutional data. The variables were age, education, breastfeeding, family history of breast cancer, smoking, alcoholism, and clinical stage of the breast cancer diagnosis.

Clinical signs such as self-detection of a lump, a bloody discharge from the nipple or nipple retraction, and enlarged breast volume were recorded. The interval between self-detection of clinical signs and seeking medical attention was divided into more or less than 90 days. The US distribution patterns of breast masses were also recorded.

Protocol and image analysis

Ultrasound

US was performed with Phillips HD7XE equipment (Phillips Co, Amsterdam, The Netherlands) with a linear multifrequency transducer (7–14 MHz). Images were stored in the Picture Archiving and Communication

System (PACS) (Carestream, Rochester, NY, USA) and were analyzed with BI-RADS, 5th Edition⁶ by a breast radiologist (BAA) with 20 years of experience.

Mammography

A digital 2D and 3D full-field Selenia Dimensions Mammography System (Hologic Inc., Marlborough, MA, USA) was used, and medial-lateral oblique (MLO) and caudal-cranial (CC) projections were obtained. Images were stored in PACS and evaluated according to the BI-RADS, 5th Edition⁷ by a breast radiologist (BAA) with 20 years of experience.

Histologic evaluation

Percutaneous needle biopsies were performed in young women (< 40 years old) with a suspected breast malignancy with BI-RADS 4 or 5. Histologic features were classified using the Scarf-Bloom-Richardson system.

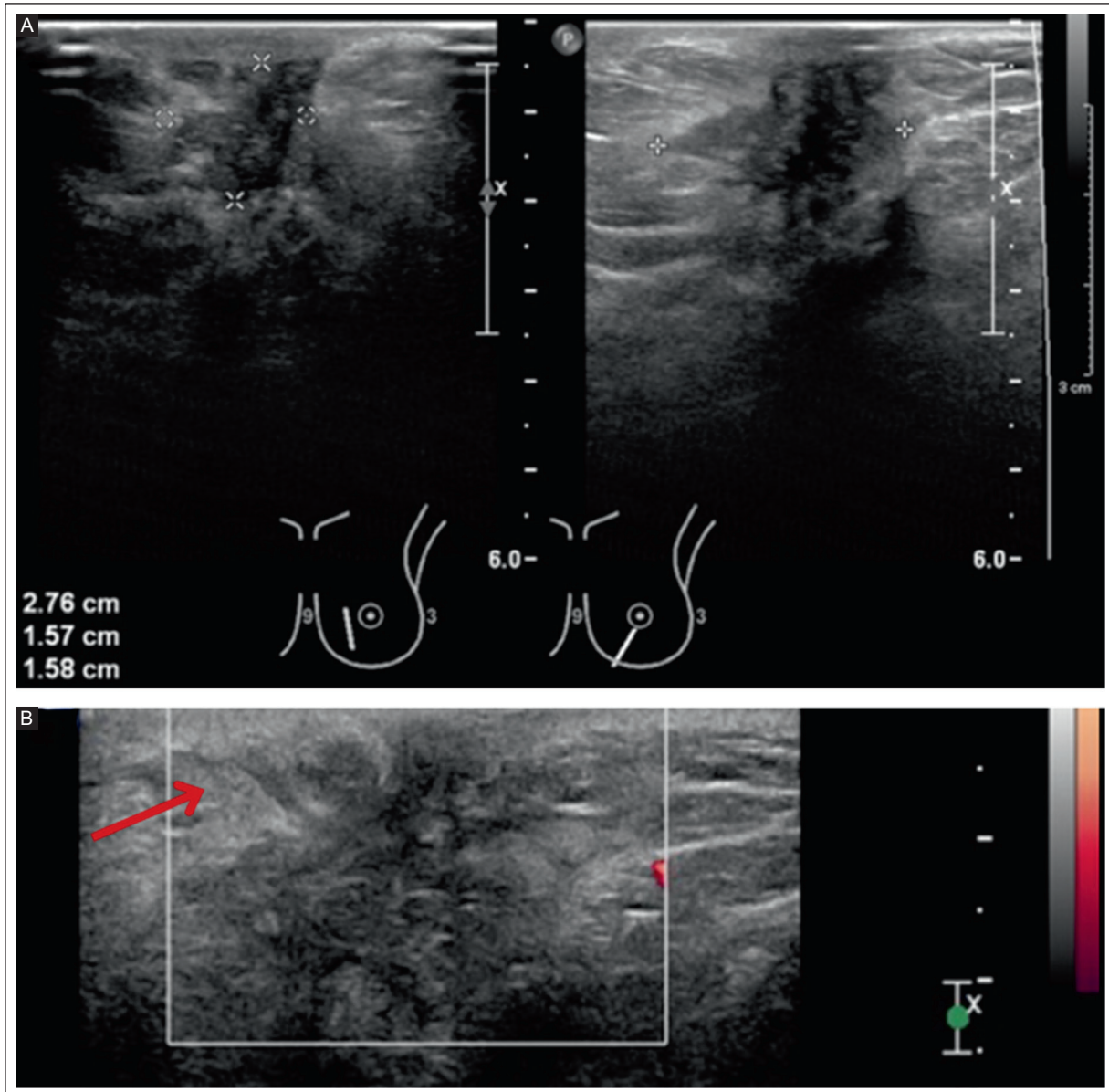


Figure 3. A 36-year-old woman with a palpable lump in the left breast and axillary region for 2 months. **A:** US grayscale with a mass in the left breast at 7 o'clock, radial and antiradial, irregular, not parallel, spiculated, hypoechoic, with shadowing. **B:** US Doppler power with absent vascularity (arrow), BI-RADS 5. The histopathologic diagnosis was an invasive ductal carcinoma with a triple-negative immunohistochemical profile. BI-RADS: Breast Imaging-Reporting and Data System; US: ultrasound.

Immunohistochemical profile

Estrogen receptor (ER) expression was determined with a primary monoclonal anti-ER antibody, and progesterone receptor (PR) expression was determined with a primary anti-progesterone receptor monoclonal antibody. The immunohistochemical classification was luminal A (ER-positive, PR-positive, and Ki-67 > 14%), luminal B (ER-positive, PR-positive, human epidermal

growth factor receptor-2, HER2), luminal B with HER2+ overexpression (ER-positive, PR-positive, HER2 positive), and triple-negative (ER-negative, PR-negative, and HER2-negative).

Statistical analysis

Frequencies and percentages were determined for qualitative variables, and means, standard deviations

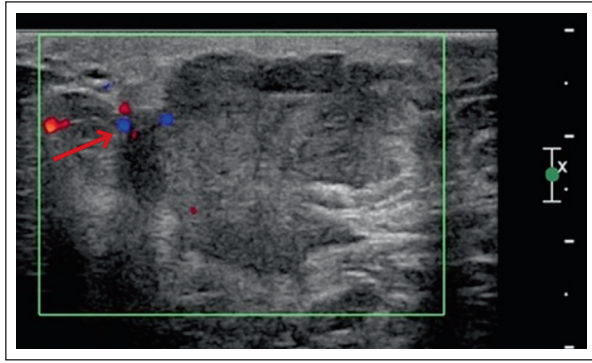


Figure 4. A 35-year-old woman with a palpable lump in the right breast for 4 months. US color Doppler with a mass in the right breast at 10 o'clock, irregular, not parallel, angular, hypoechoic, with enhancement and rim vascularity (arrow), BI-RADS 5. The histopathologic diagnosis was an invasive ductal carcinoma with a luminal B immunohistochemical profile.

BI-RADS: Breast Imaging-Reporting and Data System; US: ultrasound.

(SD), medians, minimums, and maximums were determined for quantitative variables. The analysis was performed in Excel v.16 (Microsoft, Albuquerque, NM, USA).

RESULTS

A total of 43 young women (<40 years old) with a histopathologically confirmed diagnosis of breast cancer were included. The mean age was 33.8 ± 4.5 years (range 21–39 years) (Table 1). Basic education (n = 22, 51.1%) was more common. The majority of women had breastfed at least once (n = 27, 63.0%). Twelve (28.0%) women reported a family history of breast cancer. The mean between self-detection of clinical signs and seeking medical attention was 300 ± 7.8 days (range 30–1080 days). In most patients, more than 90 days (n = 30, 69.8%) elapsed between self-detection of breast signs and seeking medical attention. A palpable lump was the most common self-detected sign in 37 (86.0%), and a blood discharge from the nipple was detected in 19 of these cases. The most common clinical stage was IIB (n = 14, 32.5%), followed by IIIA (n = 12, 28.0%).

US findings

US breast examination showed masses in all women (n = 43, 100%) (Table 2). Irregularly shaped masses (n = 35, 81.4%) and a spiculated margin (n = 16, 37.2%) were the most common, followed by an angular margin (n = 11, 25.6%), while a microlobulated or indistinct margin was less common (n = 7, 16.3% and n = 1, 2.3%, respectively). Hypoechoic masses were the most

Table 3. Mammography findings (n = 31) according to BI-RADS in young Mexican women (< 40 years old) with breast cancer

Descriptor	Parameter
Mass	n = 26
Shape	
Oval, n (%)	4 (15.4)
Round, n (%)	0
Irregular, n (%)	22 (84.6)
Margin	
Circumscribed, n (%)	4 (15.4)
Not circumscribed	
Microlobulated, n (%)	4 (15.4)
Indistinct, n (%)	9 (34.6)
Spiculated, n (%)	9 (34.6)
Density	
High density, n (%)	18 (69.2)
Equal density, n (%)	8 (30.8)
Suspicious calcifications	n = 5
Morphology	
Amorphous, n (%)	2 (40.0)
Coarse heterogeneous, n (%)	2 (40.0)
Fine pleomorphic, n (%)	1 (20.0)
Architectural distortion	n = 31
Si, n (%)	25 (80.6)
No, n (%)	6 (19.4)

^aNo mammography was performed in 12 (27.9%) of 43 patients because the US findings were suspicious of malignancy. A biopsy was performed that confirmed breast cancer. BI-RADS: Breast Imaging-Reporting and Data System, 5th Edition.

common finding (n = 33, 76.7%), followed by a complex solid-cystic pattern (n = 7, 16.3%). Among posterior findings, an acoustic shadow was more common (n = 23, 53.5%). Ductal dilation was observed (n = 18, 41.9%) and associated with a dilated single duct (n = 7, 16.2%).

Figure 1 shows the breast US of a 36-year-old woman with a self-detected palpable lump. An irregular, microlobulated, hypoechoic mass with acoustic enhancement is seen. In the homolateral axilla, an enlarged lymph node with loss of its morphology, BI-RADS 5, was found. The histopathologic diagnosis was invasive breast carcinoma. Figure 2 shows the breast US of a 27-year-old woman with a palpable lump in the left breast that had been developing for 1 month. A microlobulated, solid-cystic, BI-RADS 4B mass is seen. The histopathologic diagnosis was invasive ductal carcinoma. Figure 3 shows

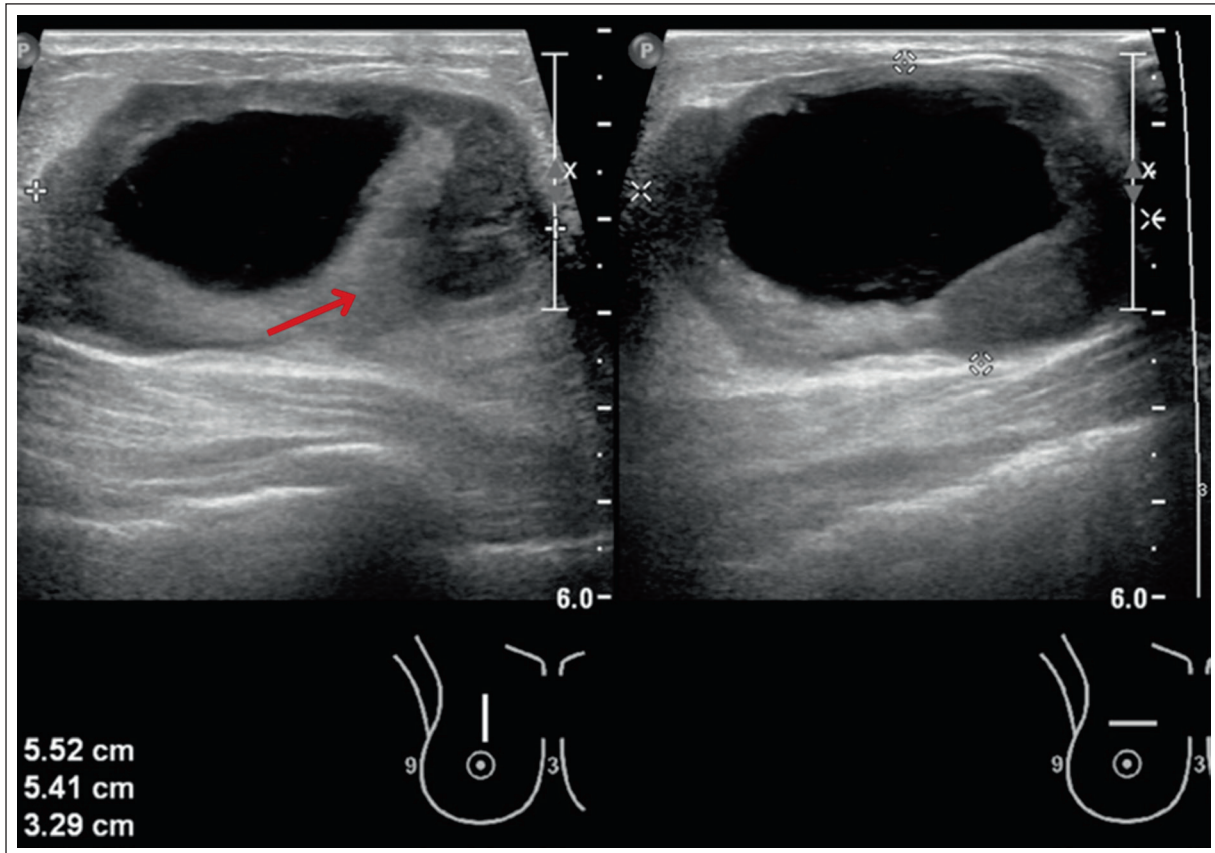


Figure 5. A 38-year-old woman with an enlarged right breast volume for 9 months. US grayscale with a mass in the right breast at 12 o'clock, radial and antiradial, oval, parallel, circumscribed, complex (arrow), with enhancement, BI-RADS 4A. The histopathologic diagnosis was an invasive ductal carcinoma with a triple-negative immunohistochemical profile. CT with metastases in the liver and chest (not shown). BI-RADS: Breast Imaging-Reporting and Data System; CT: computed tomography; US: ultrasound.

Table 4. US distribution patterns of breast masses (n = 43) in young Mexican women (< 40 years old) with breast cancer and suspected local extension

Description	n (%)
Unifocal pattern	32 (74.4)
Multifocal pattern	8 (18.7)
Multicentric pattern	2 (4.6)
Bilateral pattern	1 (2.3)
Suspicious axillary lymph nodes	
Si	26 (60.4)
No	17 (39.6)

US: ultrasound.

breast the US examination of a 36-year-old woman with a palpable lump in the left breast and axillary region that has been present for 2 months. An irregular, anti-parallel, hypoechoic, BI-RADS 5 mass with a spiculated

margin and an acoustic shadow without vascularity was found. The histopathologic diagnosis was infiltrating ductal breast carcinoma.

Figure 4 shows the US of a 35-year-old woman with a palpable lump in the right breast that has been present for 8 months. An irregular mass with an angular margin, hypoechoic, and peripheral saturation and acoustic enhancement on Doppler US, BI-RADS 5, was seen. The histopathologic diagnosis was invasive ductal carcinoma. Figure 5 shows the US of a 38-year-old woman with an enlarged right breast volume of 9 months. An oval, circumscribed, solid-cystic BI-RADS 4 mass with acoustic enhancement was seen. The histopathologic diagnosis was an infiltrating ductal carcinoma.

Mammography findings

Supplemental mammography was performed in 31 patients; 12 (27.9%) of 43 did not undergo mammography because the US examination showed suspicious

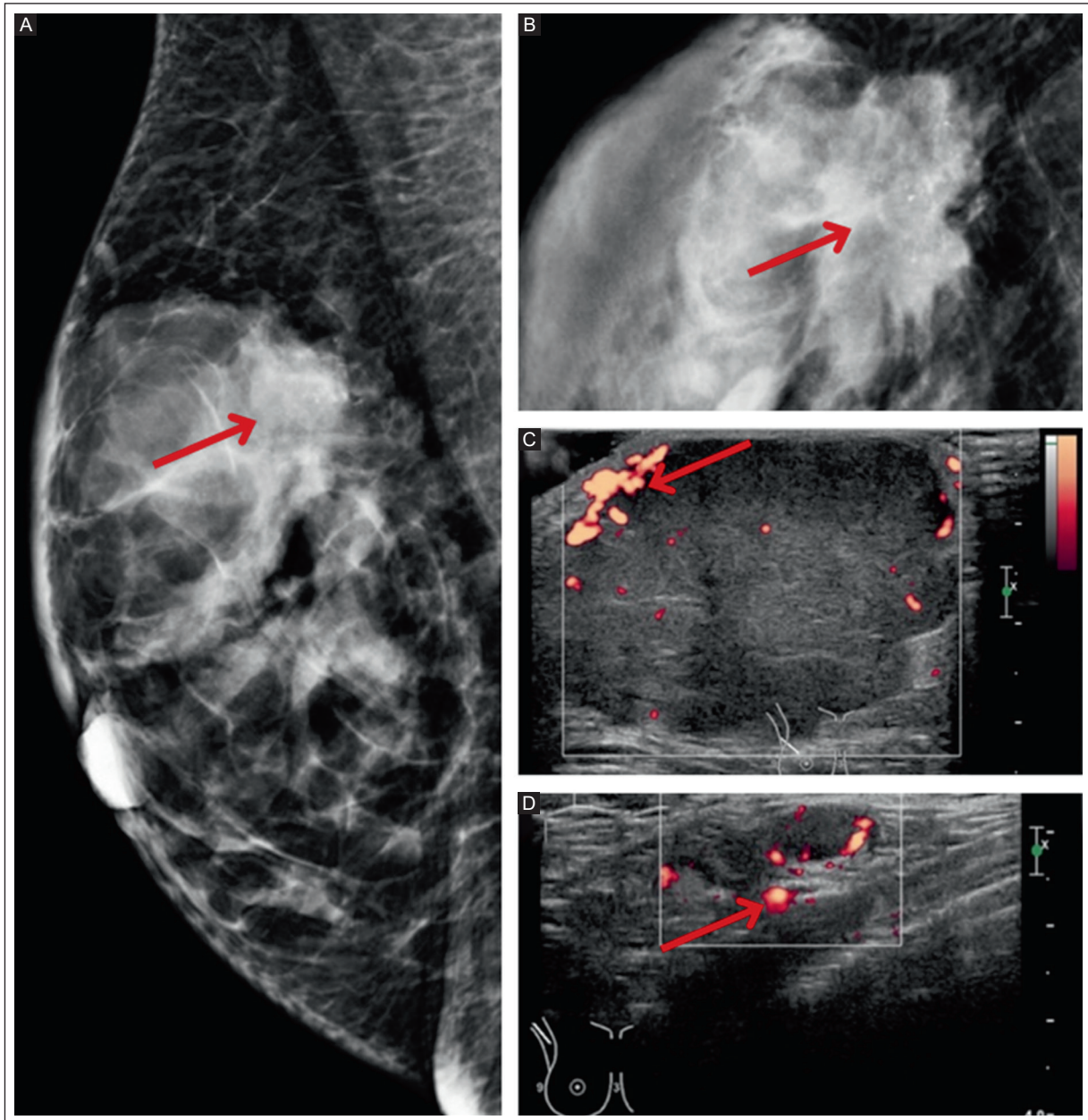


Figure 6. A 36-year-old woman with a palpable mass and an enlarged right breast volume for 36 months. **A:** mammography in projection MLO. **B:** CC view in the upper outer quadrant, with an obscured, irregular, high-density mass, with amorphous (arrows) calcifications and skin thickening. **C:** US Power Doppler of a mass in the right breast at 10 o'clock, irregular, parallel, microlobulated, hypoechoic, with rim vascularity (arrow). **D:** US Power Doppler of a right axillary, enlarged lymph node, with cortical thickening and transcapsular vascularity (arrow), BI-RADS 5. The histopathologic diagnosis was an invasive ductal carcinoma with a luminal B immunohistochemical profile. CT with metastases in the chest and bone (not shown).

BI-RADS: Breast Imaging-Reporting and Data System; CC: craniocaudal; CT: computed tomography; MLO: medial-lateral oblique; US: ultrasound.

findings of malignancy, and a biopsy confirmed the diagnosis. The most common finding was a mass (n = 26, 83.9%) and calcifications with suspicious morphology (n = 5, 16.0%) (Table 3). An irregular shape (n = 22, 84.6%) and a spiculated (n = 9, 34.6%), indistinct margin (n = 9, 34.6%), and hyperdense masses

(n = 18, 69.2%) were the most common. Calcifications with suspicious morphology were present in 5 (16.0%) of 31 patients; of these, amorphous (n = 2, 40.0%), coarse heterogeneous (n = 2, 40.0%), and fine pleomorphic (n = 1, 20.0%) calcifications were identified. Architectural distortion was a common finding (n = 25, 80.6%).

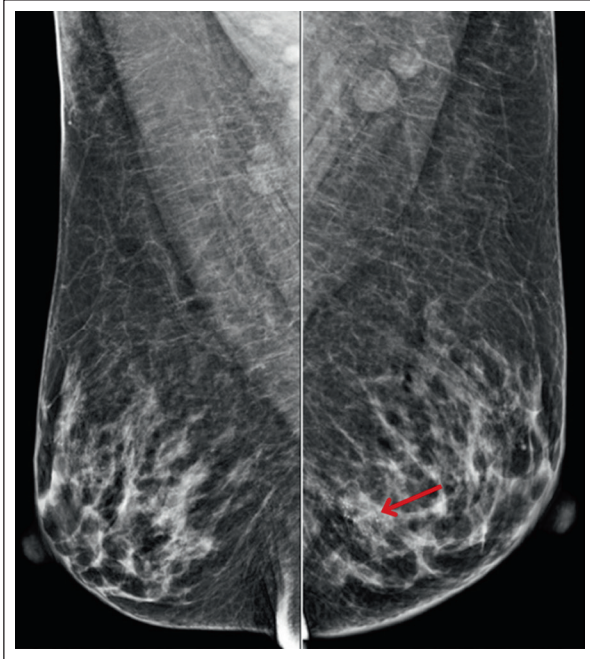


Figure 7. A 31-year-old woman with an enlarged left breast for 3 months. Mammography in MLO projection of the left breast and lower quadrants shows fine pleomorphic grouped calcifications (arrow). The histopathologic diagnosis was an invasive ductal carcinoma with a HER2 immunohistochemical profile.

BI-RADS: Breast Imaging-Reporting and Data System; HER 2: human epidermal growth factor receptor 2; MLO: medial-lateral oblique.

Figure 6 shows the US and mammography of a 36-year-old woman with a palpable lump and volume increase in the right breast over 36 months. The US shows an irregular, microlobulated, hypoechoic BI-RADS 5 mass with peripheral vascularity. The MLO and CC mammogram projections showed an irregular hyperdense mass with a darkened margin associated with amorphous microcalcifications. Figure 7 shows the mammography of a 31-year-old woman with a volume increase in the left breast over 3 months. The MLO projection shows grouped, finely pleomorphic calcifications. The histopathologic diagnosis was an infiltrating ductal carcinoma with an *in situ* component.

Local spread of the disease

The US distribution patterns of breast masses are shown in Table 4. Unifocal masses were the most common ($n = 32$, 74.4%); multifocality was observed in 8 (18.7%) patients, multicentric masses in 2 (4.6%), and bilateral masses in 1 (2.3%). A total of 26 axillary lymph nodes (60.4%) had suspicious malignant morphology

on US. Figure 8 shows the US of a 39-year-old woman in the first trimester of pregnancy with a palpable lump in the right breast. She was evaluated at the end of her pregnancy because of an enlarged volume of the left breast. There was a mass in the right breast at 12 o'clock, irregular, parallel, angular, complex, with rim vascularity and a mass in the left breast at 3 o'clock, irregular, parallel, spiculated, hypoechoic with calcifications, and rim vascularity, BI-RADS 5. The histopathology diagnosis was a bilateral invasive ductal carcinoma with a triple-negative immunohistochemical profile.

Histopathology and molecular subtypes

Invasive ductal carcinoma was the most common subtype ($n = 37$, 86.0%), followed by ductal carcinoma *in situ* ($n = 3$, 7.0%) in young women aged < 40 years with breast cancer. The immunohistochemical profiles are shown in Table 5. Six (14.0%) cases were not evaluated by immunohistochemistry (three ductal carcinomas *in situ*, two malignant phyllodes tumors, and one sarcoma).

DISCUSSION

This is the first study in young Mexican women (< 40 years old) with breast cancer that showed the long delay between detection of clinical signs during breast self-examination and seeking medical attention. The main self-detected clinical sign was a palpable lump. US and mammographic findings of breast cancer were comparable with those of older populations. Awareness and education strategies must be improved in this age group for early medical care of any breast abnormality detected during breast self-examination, and a targeted US breast examination is recommended.

There have been concerns regarding delayed diagnosis in young women (< 40 years old) because it is associated with an advanced clinical stage and poor prognosis³. In a systematic review of 87 studies with 101,954 patients, Hanna et al.⁸ found that longer delays were associated with an advanced clinical stage of breast cancer and poor survival. The 5-year survival rate was 7% for delays of more than 90 days and 12% for shorter delays. Longer delays were also associated with a more advanced clinical stage. In a multicenter cohort study of 585 young women (< 40 years old) with breast cancer, Ruddy et al.² found a delay between self-detection of the first signs and seeking medical attention and defined 90 days as a critical point. The delay was more common in women with a lower economic level than women with a higher level ($n = 229$,

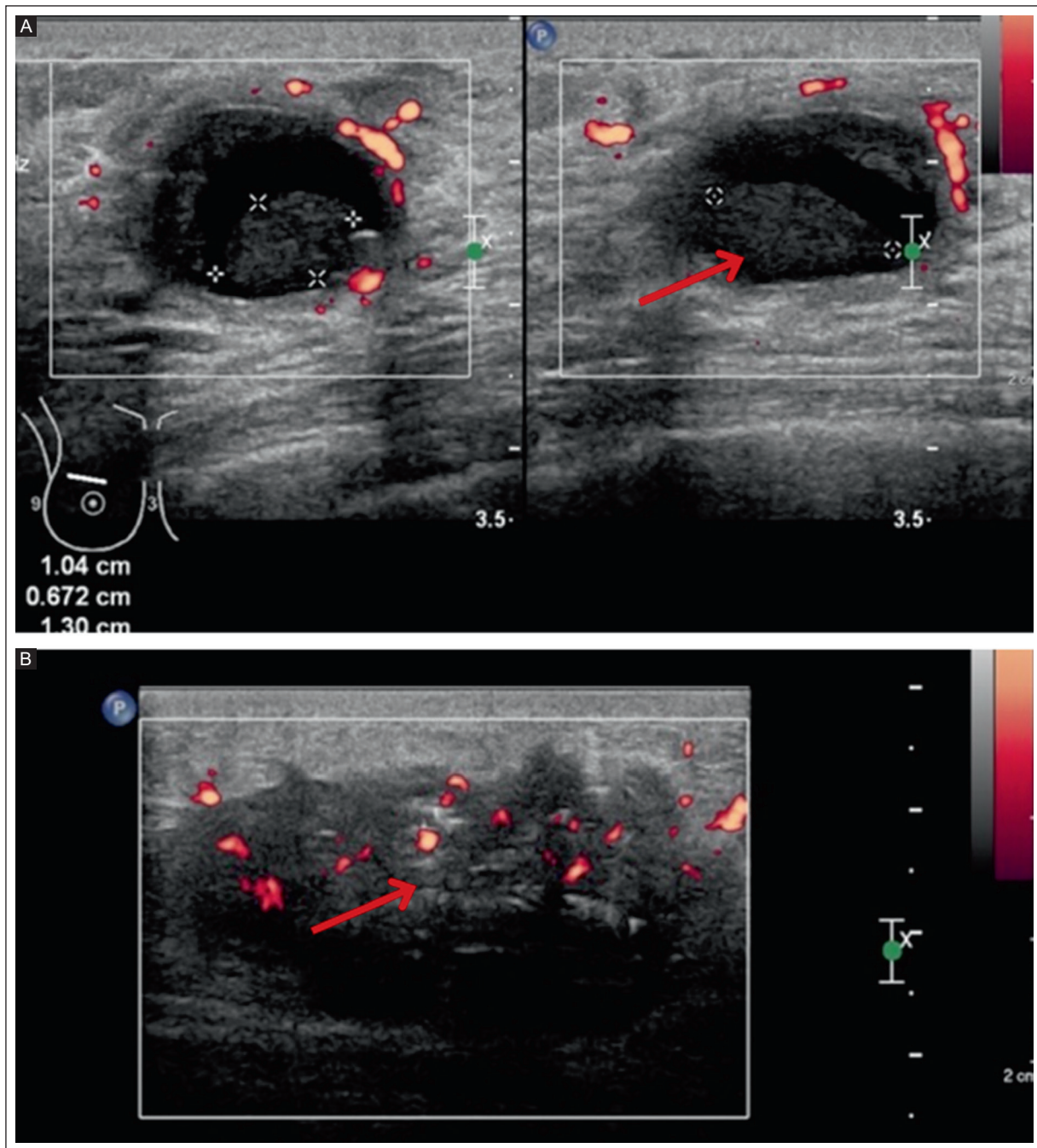


Figure 8. A 39-year-old woman with a palpable lump in the right breast since the first trimester of pregnancy. She was examined by a physician at the end of pregnancy because of an enlarged left breast volume. **A:** US Power Doppler shows a mass in the right breast at 12 o'clock, irregular, parallel, angular, complex (arrow), with rim vascularity. **B:** US Power Doppler shows a mass in the left breast at 3 o'clock, irregular, parallel, spiculated, hypoechoic with calcifications (arrow), and rim vascularity, BI-RADS 5. The histopathologic diagnosis was a bilateral invasive ductal carcinoma with a triple-negative immunohistochemical profile.

BI-RADS: Breast Imaging-Reporting and Data System; US: ultrasound.

Table 5. Immunohistochemical profile (n = 37)^a of young Mexican women (< 40 years old) with breast cancer

Diagnosis	Total ^a	Luminal A	Luminal B ^b	HER 2+	Triple-negative
Invasive ductal carcinoma, n (%)	37	11 (29.7)	15 (40.5)	2 (5.5)	9 (24.3)

^a6 (14.0%) cases were not evaluated by immunohistochemistry: 3 with cancer *in situ*, 2 with phyllodes tumor, and 1 with sarcoma. ^b6 (40.0%) of the 15 patients with luminal B had HER+ receptors overexpression.

22.3% vs. $n = 217$, 11.9%, respectively). In our study, 30 (69.8%) of 43 women had more than 90 days between self-detection and seeking medical attention. On the other hand, the palpable lump was the most common clinical manifestation, comparable with a previous study of 142 young Mexican women (< 40 years old) with breast cancer who had a palpable lump as the most common clinical sign⁹. Despite self-detection of clinical abnormalities during breast self-examination, there was a long delay in seeking medical attention.

The breast cancer imaging in young women (< 40 years old) showed no special findings. These tumors are large and fast-growing, and US examination plays an important role in young women for several reasons, mainly because of breast density. We found an irregular mass on US and mammography. Calcifications with suspicious malignant morphology were also observed. Hu et al.³ reported the most common US, mammography, and MRI findings in a retrospective cohort study of 145 young women (< 40 years old) with breast cancer. Masses ($n = 127$, 87.6%) were the most common finding, followed by suspicious calcifications ($n = 32$, 22.1%) detected on mammography. Most masses were irregularly shaped ($n = 105$, 82.6%), although there were exceptions with radiologic and pathologic discrepancies with round or oval nodules with circumscribed margins ($n = 12$, 9.4%). These results are consistent with our study, in which all patients ($n = 43$) had irregular, non-circumscribed hypoechoic masses with spiculated or angular margins and calcifications ($n = 5$, 16.0%) on US that were suspicious on mammography. US is a valuable tool that can provide relevant information about the size and distribution pattern of masses as well as local disease extension. Unifocal masses were the most common in our study, while multifocality was found in a few patients. A bilateral mass was found in only one patient, related to the prolonged period of seeking medical attention (about 1080 days). The US and mammographic findings of breast cancer in young women (< 40 years old) are comparable with those in older populations.

A multimodality imaging examination may increase diagnostic accuracy in young women with breast abnormalities. A breast MRI can be performed from the age of 25 years⁴. In our study, complementary mammography was performed in three out of four patients. Suspicious calcifications were detected, resulting in carcinoma *in situ* and invasive carcinoma. Perez-Montemayor et al.¹⁰ conducted a study comparing automated breast US (ABUS) with manual US in 140 asymptomatic women aged ≤ 40 years. Abnormal

benign findings were found in 43 (3.7%). ABUS has several advantages in terms of standardization, facilitating on-site and remote interpretation with image storage and post-processing. Large population studies are needed to define the potential utility of ABUS as an imaging screening modality in asymptomatic young women (≤ 40 years old) and its impact on early detection of malignant lesions.

Breast cancer is a group of diseases with a heterogeneous behavior associated with a molecular profile that shows differences in the clinical course, response to treatment, overall survival, and prognosis of individual patients. Young women (< 40 years old) with breast cancer are more likely to have negative prognostic factors associated with their disease. The most common clinical stage in our study was IIB ($n = 14$, 32.5%). Villarreal et al.⁵ found that young Latin American women with clinical stages II and III had more aggressive tumors with a high histologic grade, associated with more aggressive molecular subtypes such as triple-negative and -positive HER2. Terrazas et al.¹¹ found that invasive intraductal was the most common and ductal *in situ* was the second most common carcinoma in 111 biopsies of young women aged < 40 years. This finding is consistent with what is known in the literature, namely, that cancers in young women (< 40 years old) are detected later and are more aggressive. Our study is similar to the results described as we found that the most common molecular profile was the hormone-sensitive subtypes. Luminal B was the most common. This subtype has a lower proportion of ERs, a high expression of cell proliferation genes, and a lower expression of genes or proteins, typical of the luminal epithelium. They are estrogen and progesterone receptor positive or negative with a high proliferation index¹². Based on the findings of previous studies and the consistent results of this study, young women aged < 40 years with breast cancer tend to have an unfavorable histologic grade and molecular profile, in addition to the complexity they face in self-detection and seeking medical care.

The strength of this study is that all young women (< 40 years old) had a confirmed histopathologic diagnosis. The limitations are related to the small sample size and the retrospective design. The study was conducted during the time of the global pandemic from 2020 to 2022, in which we became a center for patients with COVID-19, resulting in a reduction in radiology services in other areas, which may contribute to the longer delay between self-detection of clinical signs and seeking medical attention.

CONCLUSION

Our study showed that there is a long delay between self-detection of clinical signs and seeking medical attention in young Mexican women (< 40 years old) with breast cancer. Therefore, no specific US and mammography findings exist for this age group. The imaging behavior of breast masses in young women is a challenge for radiologists. However, in the presence of a clinical abnormality of the breast, a histopathologic examination is always warranted to avoid delaying the diagnosis of breast cancer with a negative impact on prognosis.

Acknowledgments

The authors thank Professor Ana M. Contreras-Navarro for her guidance in preparing and writing this scientific paper. This original research in the Radiology Specialty field was an awarded thesis at the Primera Convocatoria Nacional 2023, "Las Mejores Tesis de Radiología para Publicar en el JMEXFRI."

Funding

This research received no external funding.

Conflicts of interest

The authors declare that they have no conflicts of interest.

Ethical disclosures

Protection of individuals. This study complied with the Declaration of Helsinki (1964) and its subsequent amendments.

Confidentiality of data. The authors declare that they followed their center's protocol for sharing patient data.

Right to privacy and informed consent. Informed consent was not required for this observational study of information collected during routine clinical care.

Artificial intelligence. The authors declare that they did not use generative artificial intelligence to prepare this manuscript and/or create tables, figures, or figure legends.

REFERENCES

1. Richards MA, Westcombe AM, Love SB, Littlejohns P, Ramirez AJ. Influence of delay on survival in patients with breast cancer: a systematic review. *Lancet*. 1999;353(9159):1119-1126. doi: 10.1016/s0140-6736(99)02143-1.
2. Ruddy KJ, Gelber S, Tamimi RM, Schapira L, Come SE, Meyer ME, et al. Breast cancer presentation and diagnostic delays in young women. *Cancer*. 2014;120(1):20-25. doi: 10.1002/cncr.28287.
3. Hu X, Myers KS, Oluyemi ET, Philip M, Azizi A, Ambinder EB. Presentation and characteristics of breast cancer in young women under age 40. *Breast Cancer Res Treat*. 2021;186(1):209-217. doi: 10.1007/s10549-020-06000-x.
4. Mainiero MB, Moy L, Baron P, Didwania AD, DiFlorio RM, Green ED, et al. ACR Appropriateness Criteria Breast Cancer Screening. *J Am Coll Radiol*. 2017;14(11S):S383-S390. doi: 10.1016/j.jacr.2017.08.044.
5. Villarreal-Garza C, Aguila C, Magallanes-Hoyos MC, Mohar A, Bargalló E, Meneses A, et al. Breast cancer in young women in Latin America: an unmet, growing burden. *Oncologist*. 2013;18 Suppl:26-34. doi: 10.1634/theoncologist.18-S2-26.
6. Mendelson EB, Bühm-Vélez M, Berg W A. 2013 BI-RADS. ACR: Ultrasound: ACR BI-RADS Atlas, Standardized Breast Imaging Reporting System. Reston, VA. American College of Radiology.
7. Sickles EA, D'Orsi CJ, Bassett LW. 2013 BI-RADS. ACR: Mammography. In: ACR's BI-RADS Atlas, Standardized System for Reporting Breast Imaging Studies. Reston, VA. American College of Radiology.
8. Hanna TP, King WD, Thibodeau S, Jalink M, Paulin GA, Harvey-Jones E, et al. Mortality due to cancer treatment delay: systematic review and meta-analysis. *BMJ*. 2020; 371: 4087. doi: 10.1136/bmj.m4087.
9. Robles-Castillo J, Ruvalcaba-Limón E, Maffuz A, Rodríguez-Cuevas S. Breast cancer in Mexican women under 40. *Ginecol Obstet Mex*. 2011; 79(8):482-488. Spanish.
10. Perez-Montemayor DF, Orozco-Licona CA. Automated breast ultrasound (ABUS) in asymptomatic young women: an exploratory study. *J Mex Fed Radiol Imaging*. 2022;1(4):259-264. doi: 10.24875/JMEXFRI.M22000032.
11. Terrazas-Torres E, Magaña-Bou LA, Ferman-Corral HE. Prevalencia de Cáncer de Mama en mujeres menores de 40 años en el centro médico ABC. *An Radiol Mex*. 2020;19(2):96-106. doi:10.24875/ARM.20000018.
12. Łukasiewicz S, Czezelewski M, Forma A, Baj J, Sitarz R, Stanisławek A. Breast Cancer-Epidemiology, Risk Factors, Classification, Prognostic Markers, and Current Treatment Strategies-An Updated Review. *Cancers (Basel)*. 2021;13(17):4287. doi: 10.3390/cancers13174287.

Coronary artery anomalies and normal anatomical variants in coronary computed tomography angiography (CCTA): a pictorial essay

Adriana Parada-Gallardo¹ and Harold Goerne^{2,3*}

¹Imaging Department, Hospital General de Zapopan, Zapopan, Jalisco, Mexico; ²Cardiac Imaging Department, Centro de Imagen y Diagnóstico (CID); ³Hospital de Pediatría, Centro Médico Nacional de Occidente, Instituto Mexicano del Seguro Social, Guadalajara, Jalisco, Mexico

ABSTRACT

It is important to differentiate between coronary artery anomalies and normal anatomical variants. Several imaging modalities, such as echocardiography, invasive coronary angiography (ICA), coronary magnetic resonance imaging (CMRI), and coronary computed tomography angiography (CCTA), are used. The gold standard for assessing coronary artery anomalies and normal anatomical variants is CCTA. CCTA has high spatial and temporal resolution, multiplanar reconstruction, adequate isotropic resolution with a large field of view, and detailed noninvasive visualization of coronary artery anatomy. Normal anatomical variants show no hemodynamic changes and are usually incidental findings. Coronary artery anomalies are rare and classified by origin, origin/course, course, and termination. In many cases, patients with coronary artery anomalies are asymptomatic, and some anomalies have a hemodynamic impact. There are high-risk anatomical features of malignant coronary artery anomalies, which, under stress, can cause ischemia in the areas perfused by the anomalous vessel and are associated with myocardial ischemia, ventricular arrhythmias, heart failure, or sudden death. The radiologist should differentiate coronary artery anomalies and normal anatomical variants to make a correct radiological-clinical correlation and recognize the advantages of CCTA in diagnosis. This pictorial essay shows the CCTA findings of coronary artery anomalies and normal anatomical variants.

Keywords: Coronary computed tomography angiography. Coronary artery anomalies. Coronary artery anatomical variants.

INTRODUCTION

Coronary artery anomalies are congenital anatomical alterations that can present malignant features with a risk of ischemia or sudden death, in contrast to normal variants with a benign clinical behavior and no hemodynamic impact¹⁻³. Most patients with coronary artery anomalies are asymptomatic^{4,5}. Symptomatic patients may present exercise-related or -unrelated chest pain, palpitations, dyspnea, dizziness, syncope, myocardial infarction, or sudden cardiac death^{3,4}.

During embryo development, primitive coronary trunks arise within the developing myocardium. During the first stage of development, the primitive coronary arteries join the aortic root. During this stage, various changes in the communication of the coronary arteries can occur and create an aberrant pathway⁶. The coronary arteries are named according to the ventricle they supply and not by their origin. The right coronary artery always follows the right ventricle, and the left coronary artery follows the left ventricle, regardless of the spatial location of the ventricles.

*Corresponding author:

Harold Goerne
E-mail: haroldgoerne@gmail.com

Received for publication: 13-03-2024

Accepted for publication: 24-04-2024

DOI: 10.24875/JMEXFRI.M24000075

Available online: 10-07-2024

J Mex Fed Radiol Imaging. 2024;3(2):105-114

www.JMeXFRI.com

2696-8444 / © 2024 Federación Mexicana de Radiología e Imagen, A.C. Published by Permanyer. This is an open access article under the CC BY-NC-ND (<https://creativecommons.org/licenses/by-nc-nd/4.0/>).

The assessment of coronary artery anomalies and normal anatomical variants can be performed with various imaging modalities such as transthoracic ultrasound, invasive coronary angiography (ICA), coronary magnetic resonance imaging (CMRI), and coronary computed tomography angiography (CCTA).

CCTA is the gold standard for characterizing coronary artery anomalies and normal anatomical variants with visualization of their origin and course^{7,8}. This pictorial essay shows the features of coronary artery anomalies and normal anatomical variants of CCTA for educational purposes.

CARDIAC IMAGING MODALITIES

Transthoracic ultrasound: the origin of coronary artery anomalies and their proximal course can be assessed, and the coronary ostium visualized^{7,8}. It does not use radiation and is the modality of choice in pediatric patients due to its excellent transthoracic acoustic window, in contrast to adult patients with a limited window⁸. Thus, its diagnostic accuracy in identifying the coronary ostium, visualizing the full course of the coronary arteries, and their relationship to the great vessels and other structures is lower⁷.

ICA, an imaging modality, was important for identifying and classifying coronary artery anomalies⁷, but it is currently recommended only as a complementary examination to CCTA⁸ due to its invasiveness, radiation exposure,⁸ relatively lower spatial resolution, lack of three-dimensional images,⁷ and inability to characterize non-coronary cardiac anatomy surrounding coronary artery anomalies.

CMRI allows visualization of the origin and course of the coronary arteries, including their relationship to adjacent vascular structures⁸. It evaluates ventricular, atrial, and valve function, regional contractility, and myocardial viability with a high spatial resolution, although lower than CCTA. CMRI is an alternative to CCTA with a grade I recommendation for anatomical assessment of coronary artery anomalies to avoid radiation^{8,9}. It is ideal for the pediatric population. CMRI is useful for visualizing prior infarcts with late gadolinium enhancement⁸. However, due to its lower spatial resolution and availability, it has a secondary role compared with CCTA⁷.

CCTA is the gold standard for assessing coronary artery anomalies and normal anatomical variants⁷. A low radiation dose, fast acquisition time, high spatial and temporal resolution, multiplanar reconstruction, adequate isotropic resolution, wide field of view, and detailed noninvasive visualization of coronary anatomy

Table 1. Anatomical variants of the coronary arteries

Description
• Coronary dominance
• Branching variations
• Duplication of the anterior descending artery
• Absence of the left main coronary artery
• Single coronary artery

Adapted from: Ben-Dor et al.¹³ and Perez-Pomares et al.¹⁴.

are the advantages of CCTA, and its 3D information is useful for preoperative planning¹⁰. CCTA provides information about the lumen of the coronary arteries (stenosis), the causes of external compression, adjacent cardiac structures, and great vessels⁷. CCTA is superior to ICA in determining the origin, course, termination, and anatomical pattern of the coronary branches⁶.

CCTA ACQUISITION PROTOCOLS

Prospective ECG-triggering, also called “step-and-shoot” acquisition¹¹, has lower radiation levels than other acquisition types and maintains image quality and accuracy, including High Pitch Helical^{11,12}. Effective radiation is reduced from 20 to 2 to 6 mSv (–70 to –80%) with an average of 4 mSv. The X-ray beam is limited to a preselected cardiac phase, usually the diastolic phase². Compared with the retrospective protocol, radiation exposure is reduced by limiting the number of phases acquired, which is lower than ICA catheterization¹¹.

Retrospective ECG gating provides information on cardiac function with appropriate reconstruction in multiple phases of the cardiac cycle. This protocol is ideal for evaluating cardiac wall motion changes. Its main disadvantage is its higher radiation exposure compared with other protocols. A CT scanner with 64 detectors and a standard voltage tube of 120 kVp generates a higher effective radiation dose with a range of 9-21 mSv (mean 15 mSv) compared with 2-10 mSv for ICA¹¹.

Retrospective ECG gating with dose modulation provides information on the function and myocardial motility. The best quality is limited to one cardiac phase (e.g., mid-diastole) and reduces the radiation exposure of other phases that are not required for good-quality image reconstruction. Compared with the conventional retrospective protocol, the radiation dose is reduced by 30-50%, reducing the risk of cancer¹¹.

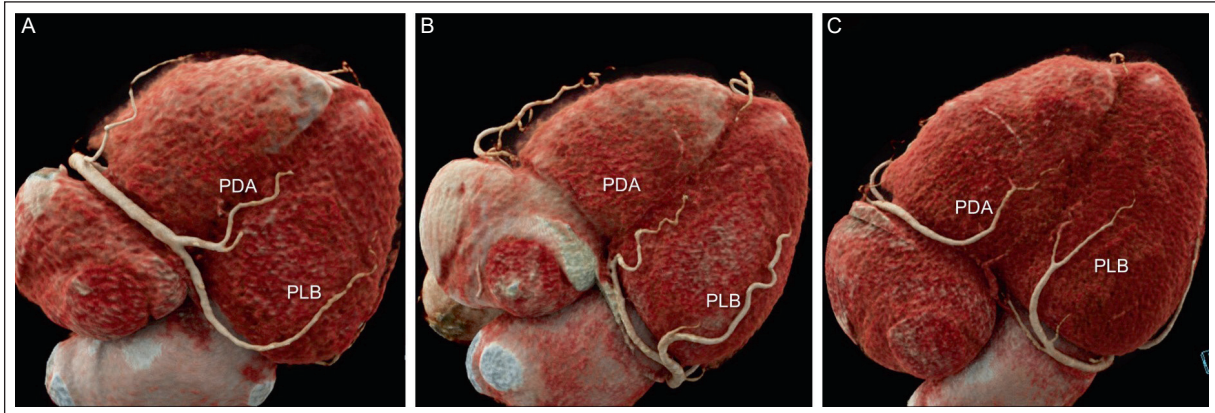


Figure 1. Coronary dominance. CRT reconstructions of the inferior aspect of the heart show the origin of the PDA and the PLB in **A:** coronary right dominance, **B:** coronary left dominance, and **C:** coronary codominance.

CRT: cinematic rendering technique; PDA: posterior descending artery; PLB: posterolateral branch.

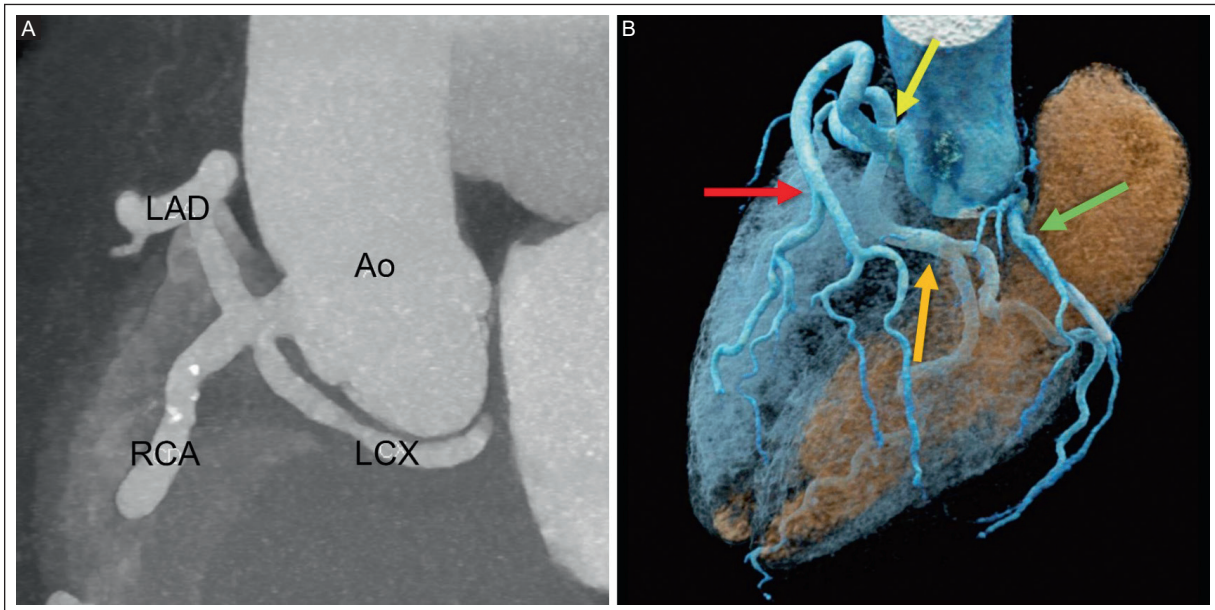


Figure 2. Single coronary artery. **A:** MIP shows a single coronary ostium in the right sinus of Valsalva from which the left anterior descending artery, right coronary artery, and circumflex artery arise. **B:** CRT shows the single coronary ostium (yellow arrow), the pre-pulmonic anterior descending artery (red arrow), the retro-aortic circumflex (green arrow), and the right coronary artery (orange arrow).

AO: ascending aorta; CRT: cinematic rendering technique; LAD: left anterior descending artery; LCX: left circumflex artery; MIP: maximum intensity projection; RCA: right coronary artery.

High Pitch Helical uses a radiation dose of less than 1 mSv¹¹. It is ideal for pediatric patients as it has a shorter exposure time. It requires a dual-source CT scanner. The heart rate of the patient must be less than or equal to 60 or 65 beats per minute (bpm), depending on the protocol of each institution. A tube voltage of 80 kVp and a tube current of 50 mAs with iterative reconstruction are used with a radiation dose

< 0.1 mSv in patients weighing less than 75 kg with a heart rate of 60 bpm¹¹.

NORMAL ANATOMICAL VARIANTS OF THE CORONARY ARTERIES

Table 1 shows the normal anatomical variants of the coronary arteries:

- **Coronary dominance:** it can be right, left, or codominant. Dominance is defined in the artery from which the posterior descending artery and the posterolateral branch arise (Figure 1). In the general population, right dominance is observed in 85%, left dominance in 7-8%, and codominance in 7-8%⁶.
- **Branching variations:** the conal artery is the first branch of the right coronary artery. However, in 50% of individuals, it arises directly from the aorta (separate ostium)⁶. The sinoatrial node artery is the second branch of the right coronary artery in 60% of people, and in 40%, it arises from the circumflex artery⁶. The ramus intermedius arises from a trifurcation of the left main coronary artery between the anterior descending artery and the circumflex artery. The ramus intermedius supplies the anterolateral wall of the left ventricle, similar to a diagonal branch or an obtuse marginal branch⁶.
- **Duplication of the anterior descending artery:** this artery has two distinct vascular segments in the anterior interventricular groove. The left branch may be long, while the right branch is short⁶.
- **Absence of the left main coronary artery:** this is the most common anatomical variant (1 to 2%) in the general population¹³. The anterior descending artery and the circumflex artery arise separately, directly from the aortic left sinus of Valsalva.
- **Single coronary artery** is a rare anatomical variant in which a single coronary ostium arises from the aortic root (Figure 2). It occurs in 0.002-0.044% of the population. The artery may follow the course of a right or left coronary artery and divide after its origin into two or three main coronary branches¹⁴.

CLASSIFICATION OF CORONARY ARTERY ANOMALIES

The incidence of coronary artery anomalies is estimated at 0.9-5.6%¹⁵ and the prevalence at 1%^{8,14,16-18}. Most patients are asymptomatic (80%).⁹ Symptomatic patients may present syncope, myocardial ischemia, infarction, heart failure, or sudden death (0.6% of cases).

Table 2 shows the classification of coronary artery anomalies in terms of their origin, origin/course, course, or termination^{7,10}. There are coronary artery anomalies without a hemodynamic impact (benign)^{1,2} and high-risk or malignant coronary anomalies that can cause ischemia in the areas perfused by the anomalous vessel under stressful conditions, such as exercise³.

Anomalies of the origin of the coronary arteries

DEPENDING ON THE NUMBER OF VESSELS

- **Single:** the coronary artery arises from a single ostium of the aortic root. It is extremely rare (0.0024-0.044%)⁵.
- **Multiple:** it involves more than one coronary artery or branch and can be divided into two types: (a) more than one artery or branch arising at one site and (b) two coronary arteries or branches arising at different ectopic sites¹⁹.

DEPENDING ON THE LOCATION

The anomalous location of the coronary ostium within the aortic root or near the coronary sinus of Valsalva (for each artery) is divided into the following¹⁷:

- **High origin (high takeoff)** (Figure 3): it is the origin of one or two coronary arteries at least 1 cm above the level of the sinotubular junction of the aorta^{6,7}. It occurs more frequently in the right coronary artery and is sometimes associated with a bicuspid aortic valve⁵. It usually has no clinical alterations but it is important in aortic surgery and can cause difficulties in ICA.
- **Anomalous origin from the pulmonary artery** is an anomalous origin of the left coronary artery from the pulmonary artery (ALCAPA) or the right coronary artery from the pulmonary artery (ARCAPA) (Bland-White Garland syndrome)^{8,14} (Figure 4). The prevalence is 1 in 300,000 births¹⁴, and abnormal blood sequestration occurs¹⁴. It is considered a malignant coronary anomaly that can cause myocardial infarction or sudden death¹⁴. If collateral vessels are present, it is called “adult type.” If there are no or very few collaterals, it is called “infant type”¹⁴.
- **From the opposite sinus and the non-coronary sinus:** the most common anomaly is the anomalous origin of the right circumflex sinus with a retroaortic course. It is divided into the right anomalous origin of a coronary artery from the opposite sinus (right ACAOS) and the left coronary artery originating from the right coronary sinus (left ACAOS)⁸. The anomalous origin of the coronary artery from the posterior aortic sinus (non-coronary) is very rare and is associated with sudden death¹⁴.

Table 2. Classification of coronary artery anomalies by origin, origin/course, course and termination

Origin
Number of vessels
Single
Multiple
Location
High origin (high take-off)
Anomalous origin from the pulmonary artery (ALCAPA) (ARCAPA)
Opposite sinus, non-coronary sinus, inverted coronary artery and commissural
Origin/course
Retroaortic
Interarterial
Prepulmonic
Transeptal (subpulmonic)
Course
Myocardial bridging
Intracavitary
Duplication of the coronary artery
Termination
Coronary artery fistula
Coronary arcade
Extracardiac

ALCAPA: left coronary artery from the pulmonary artery; ARCAPA: right coronary artery from the pulmonary artery.

Adapted from: Kim et al.⁶ Gentile et al.⁷ Bigler et al.¹⁰ and Angelini et al.¹⁷.

- **Inverted coronary artery:** it is morphologically referred to as left or right, depending on its distal course and distribution, and the corresponding left or right ventricle²⁰.
- **Commissural:** it is the coronary origin in one of the commissures between the sinuses of Valsalva.

Anomalies of the origin/course of the coronary arteries

- **Retroaortic** (benign): it is most common with a dorsal course to the aortic root without clinical significance²¹ (Figure 5A).
- **Interarterial** (malignant): it is located between the aortic root and the pulmonary artery and causes external coronary compression^{1,8,14} (Figure 5B).

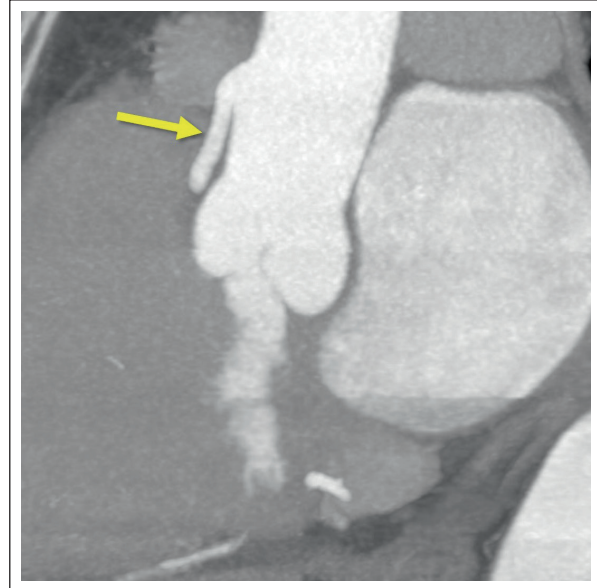


Figure 3. MIP reconstruction shows the high origin of the right coronary artery 2 cm above the sinotubular junction (yellow arrow). MIP: maximum intensity projection.

More commonly, it is due to an anomalous origin of the left coronary artery from the right coronary sinus (ACAOS). Its prevalence in a study of pediatric patients with echocardiography was estimated to be 0.17% and about 0.7% with CMRI, probably due to its better performance²². Myocardial ischemia or sudden death may occur, especially in young adults¹⁸.

- **Prepulmonic** (benign): it is located anterior to the pulmonary artery²¹ (Figure 5C). Although it has no clinical relevance, its identification is important for planning surgical procedures involving the right ventricular outflow tract and the pulmonary artery trunk, such as the transannular patch, in the correction of the tetralogy of Fallot.
- **Transeptal** (subpulmonic) (benign): it runs through the interventricular septum and below the pulmonary valve at the level of the right ventricular outflow tract (Figure 5D). It is not usually associated with high-risk features^{8,21,22}.

Anomalies of the course of the coronary arteries

- **Myocardial bridge:** it is an epicardial coronary artery with an intramyocardial course (Figure 6). The mean depth is 2.5 mm, and the mean length is 19.3 mm²¹. It is most commonly located in the

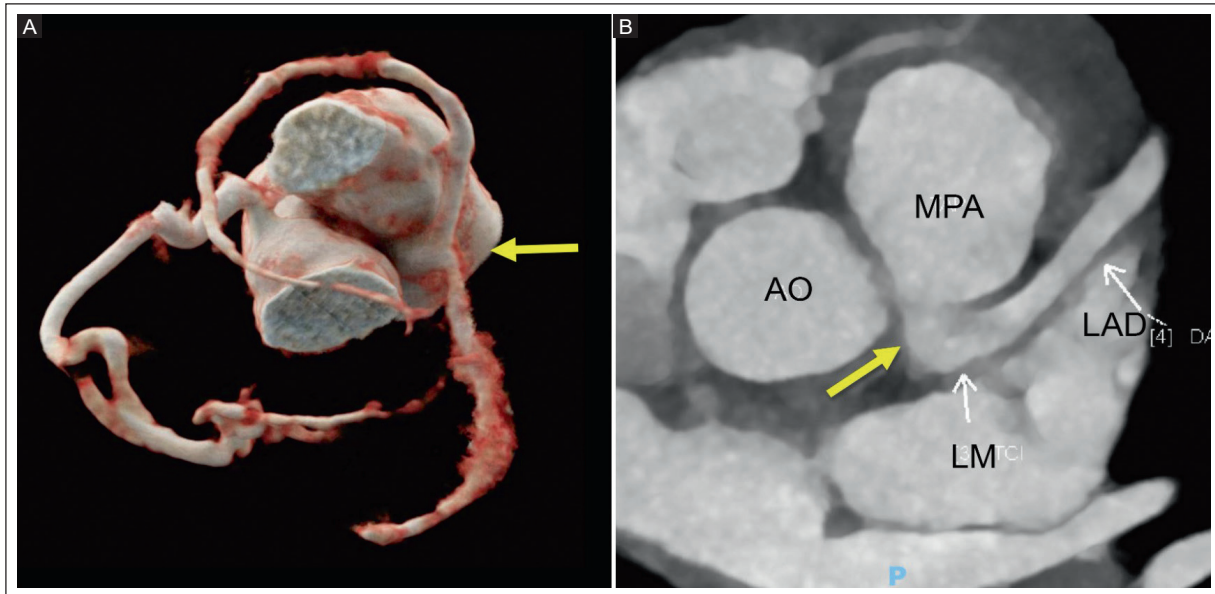


Figure 4. Anomalous origin of the left coronary artery from the pulmonary artery (ALCAPA). **A:** CRT showing anomalous origin of the left coronary artery from the pulmonary artery (ALCAPA) (yellow arrow). **B:** MIP showing anomalous origin of the left coronary artery from the pulmonary artery (ALCAPA) (yellow and white arrows).

AO: aorta; MPA: main pulmonary artery; CRT: cinematic rendering technique; LAD: left anterior descending artery; LM: left main coronary artery; MIP: maximum intensity projection.

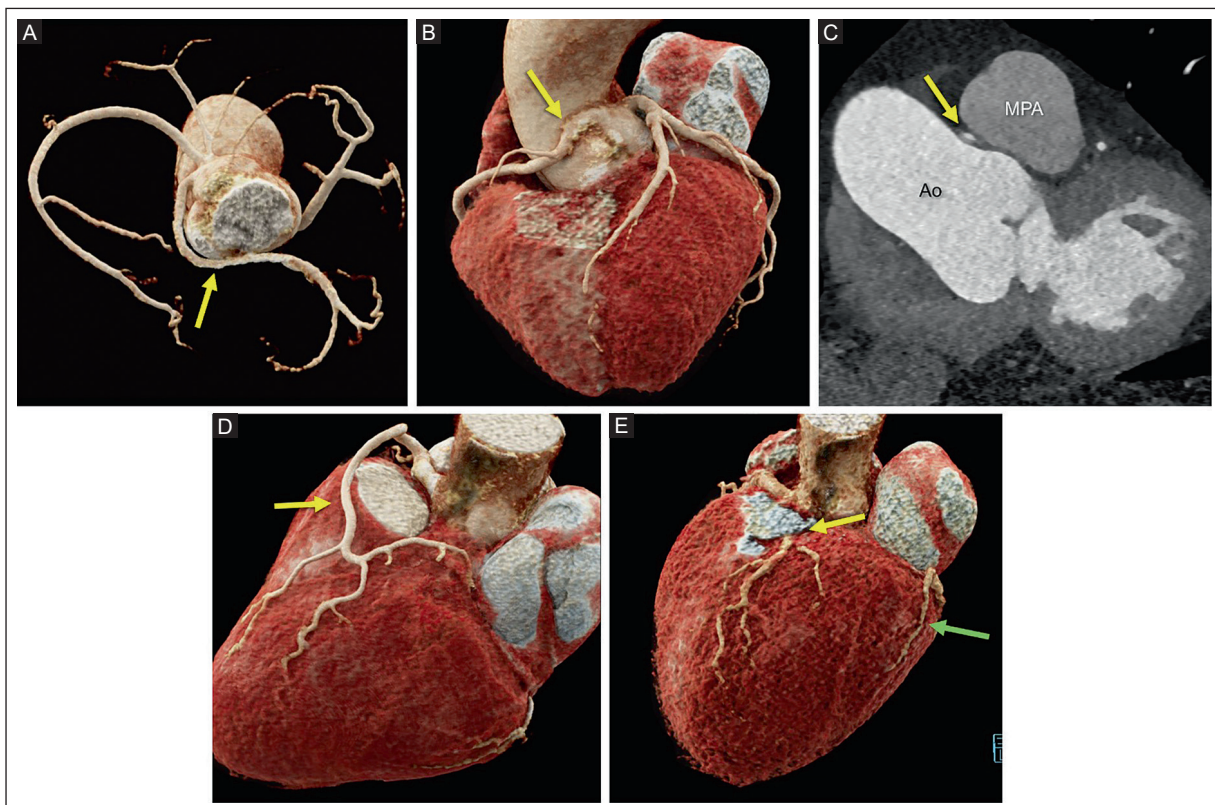


Figure 5. A: retroaortic course. CRT shows the anomalous origin of the circumflex artery from the right sinus of Valsalva and its retroaortic course (arrow). **B:** interarterial course. CRT shows the anomalous origin of the right coronary artery from the left sinus of Valsalva with an interarterial course (arrow). **(C)** MPR shows the course of the right coronary artery (arrow) between the AO and the MPA. **D:** prepulmonic course. CRT shows the anomalous origin of the left coronary artery from the right sinus of Valsalva and its prepulmonic course (arrow). **E:** transseptal course. CRT shows the transseptal course of the anterior descending artery (yellow arrow). Note the absence (agenesis) of the circumflex artery with a superdominant right coronary artery (green arrow) compensating for this coronary anomaly.

AO: aorta; CRT: cinematic rendering technique; MPA: main pulmonary artery; MPR: multiplanar reformation.

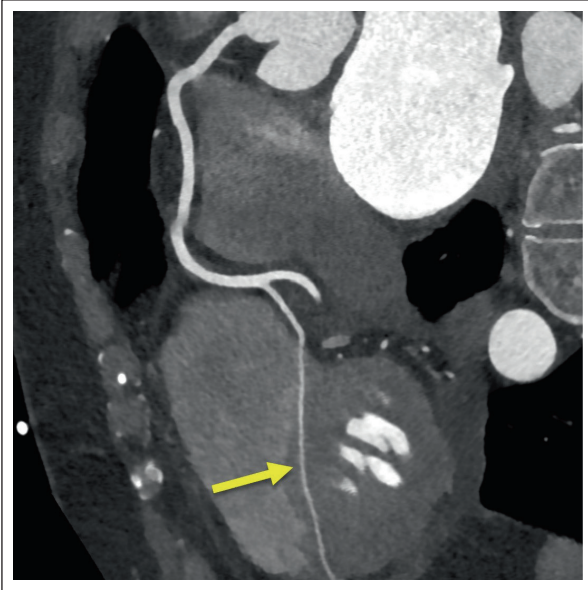


Figure 6. Myocardial bridge. Curved planar reformation of the right coronary artery shows the long intramyocardial course of the posterior descending artery (arrow).

middle segment of the anterior descending artery. It is usually asymptomatic, so there is a discrepancy in prevalence. In ICA, it is reported to be from 0.5% to 2.5%, and in autopsy, it is reported to be from 15% to 85%.^{6,23}

The coronary anomaly of very superficial myocardial bridging (incomplete bridging) does not cause hemodynamic alterations and is undetectable in ICA due to the “milking effect”¹⁴. Compression occurs during systole; in most cases, there are no significant clinical alterations. Patients with deep and long bridges may have symptoms of ischemia or infarction due to the restriction in coronary flow. Functional tests are required to detect ischemia in the affected area in these cases. The distal segment of the vessel and at the level of the bridge is hemodynamically protected from atherosclerosis, while the proximal segment shows an increase in atherosclerosis.

- **Intracavitary** (benign): it is the course of the right coronary artery within the right atrium (Figure 7) or the anterior descending artery in the right ventricle. It is usually asymptomatic, although damage to the right coronary artery may occur during cannulation/instrumentation of the right heart²².
- **Duplication of the coronary artery** (benign): it occurs in up to 1% of the population and consists of a duplicate coronary artery running anterior to the interventricular groove. Any of the three major

coronary arteries may be duplicated, although more commonly, the anterior interventricular artery^{6,24}. The short right coronary artery ends in the interventricular groove without reaching the apex, and the long right coronary artery re-enters the groove of the anterior wall of the left ventricle and runs to the apex⁶. It is important to distinguish duplication of the coronary arteries from the coronary artery and the diagonal branch, which runs parallel⁶.

Anomalies of the termination of the coronary arteries

- **Coronary artery fistula:** communication between one or two coronary arteries and a ventricle, the coronary sinus (Figure 8), the superior vena cava, or the pulmonary artery. It is observed in 0.1-0.2% of all patients undergoing selective ICA^{6,14}. The affected coronary artery is dilated and tortuous due to increased blood flow. Coronary fistulas may have single or multiple communications at the outflow site or fine vessels forming a diffuse network or plexus⁶. The most common drainage site is the right ventricle (45% of cases), followed by 25% in the right atrium and 15% in the pulmonary artery. In less than 10% of cases, the coronary fistula drains into the left atrium or ventricle⁶.

The hemodynamic implications depend on resistance, which is determined by the size, tortuosity, and length of the fistula, as well as the drainage site¹⁴. If the shunt leads to a right-sided ventricle, the hemodynamic alteration is similar to an extracardiac left-to-right shunt. If the connection is to a left-sided ventricle, the hemodynamic alteration resembles aortic insufficiency⁶. Myocardial perfusion may decrease in the portion of the myocardium supplied by the abnormally connecting coronary artery, representing a hemodynamic steal phenomenon that can lead to myocardial ischemia⁶. A small fistula has a good prognosis without treatment. A medium or large fistula is associated with long-term complications, such as angina, myocardial infarction, arrhythmia, heart failure, or endocarditis²⁵.

- **Coronary arcade:** it is a rare communication between the right and left coronary arteries when there is no stenosis⁶. If this anastomosis is sufficiently large, it is identified in the ICA. It can be distinguished from the collateral vessels based on the prominent straight communication between the two unobstructed main arteries⁶.

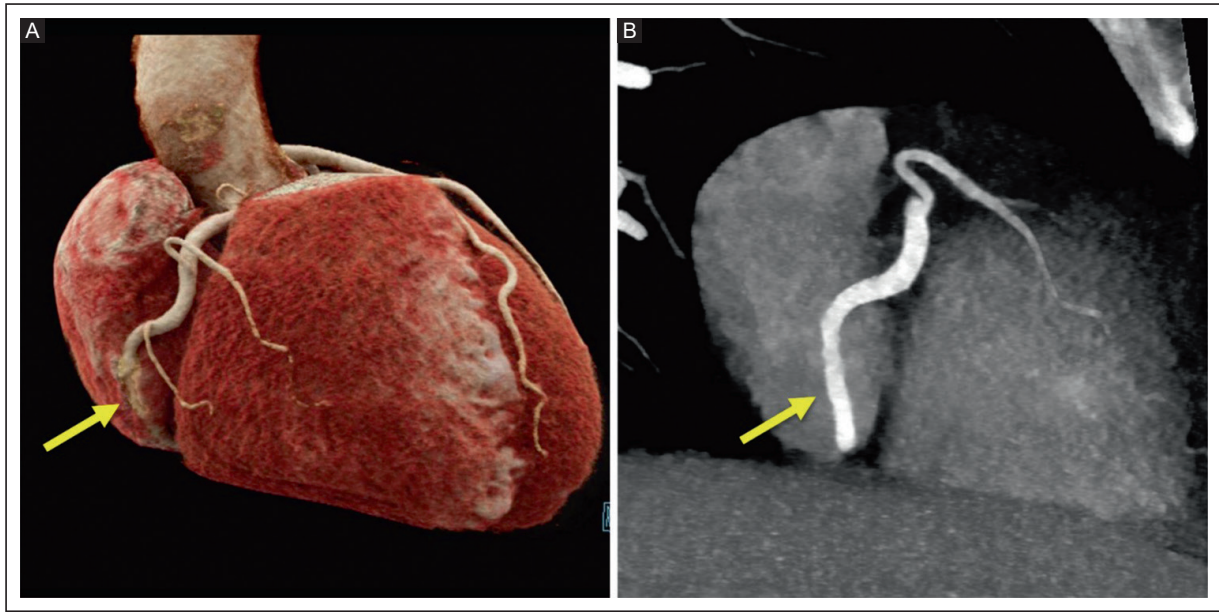


Figure 7. Intracavitary course. **A:** CRT and **B:** MIP show the intracavitary middle segment of the right coronary artery into the right atrium (arrows). CRT: cinematic rendering technique; MIP: maximum intensity projection.

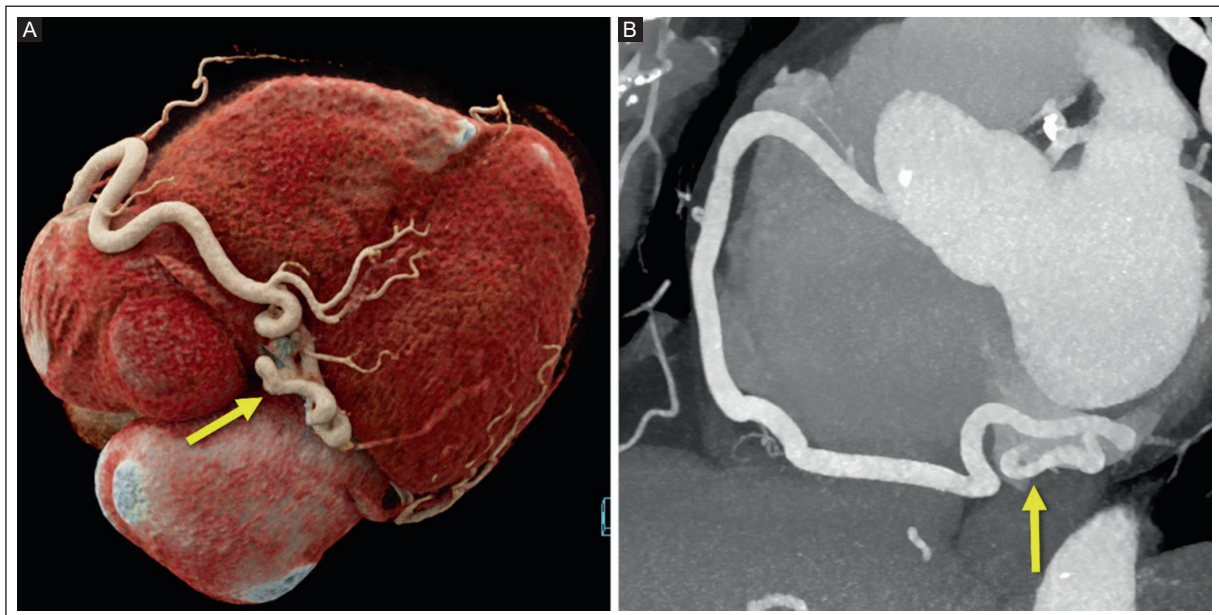


Figure 8. Coronary fistula. **A:** CRT shows the tortuous and ectatic course of the right coronary artery (yellow arrow). **B:** MIP shows a right coronary artery fistula to the coronary sinus (yellow arrow). CRT: cinematic rendering technique; MIP: maximum intensity projection.

– **Extracardiac termination:** it is the communication between coronary arteries and extracardiac vessels such as bronchial, internal mammary, pericardial, esophageal, diaphragmatic, and/or pericardial arteries. This communication only becomes functionally

significant if a pressure gradient exists between the two arterial systems⁶. This coronary anomaly is associated with atherosclerotic coronary artery disease, which causes blood flow from the bronchial to the coronary arteries⁶.

Table 3. High- risk anatomical features of coronary artery anomalies

Description
– Interarterial course: abnormal course of the coronary artery between the aorta and the pulmonary artery
– Slit-like ostium: narrowing > 50% of proximal vessel
– Acute take-off angle: tangential vessel course < 45°
– Intramural course (into the aortic wall)
– Elliptical luminal vessel shape: height/ width ratio > 1.3 and segmental hypoplasia
– Proximal vessel narrowing by hypoplasia
– Anomalous vessels with > 50% of the vessel cross-sectional area compared to the distal portion

Adapted from: Cheezum *et al.*² Kim *et al.*⁶ Gräni *et al.*⁸ and Bigler *et al.*¹⁰.

CHARACTERISTICS OF HIGH-RISK CORONARY ANOMALIES

Table 3 shows the anatomical features of high-risk for malignant coronary anomalies, which, under stress, can cause ischemia in the areas perfused by the anomalous vessel and are associated with myocardial ischemia, ventricular arrhythmias, heart failure, or sudden death^{1,2,6,8,10,17,21}.

Anatomical features of high-risk include: an interarterial course, which is the anomalous course of the coronary artery between the aorta and the pulmonary artery; a slit-like ostium with narrowing > 50% of the proximal vessel; an acute takeoff angle with a tangential vessel course < 45°; an intramural course of the anomalous vessel within the tunica media of the aortic wall; an elliptical luminal vessel shape with a height/width ratio > 1.3 and segmental hypoplasia; proximal vessel narrowing by hypoplasia; and anomalous vessels with > 50% of the vessel cross-sectional area compared with the distal portion^{1,2,6,8,10,17,21}.

CONCLUSION

This pictorial essay presents the CCTA findings of coronary artery anomalies and normal anatomical variants. For differential diagnosis, it is important to consider the history and evolution of clinical manifestations to correlate the imaging and clinicopathological findings. CCTA is a first-line noninvasive cardiac imaging modality for assessing the origin, course, and termination of the coronary arteries. CCTA shows the origin and course of the coronary arteries, their anatomical relationship to other cardiac structures, and luminal stenoses with better quality and accuracy than ICA.

CCTA has advantages in assessing coronary artery anomalies, especially in preoperative planning and postoperative follow-up for detecting complications. CCTA requires less acquisition time and less radiation. This pictorial essay can be useful for radiologists to become familiar with the CCTA findings of the coronary arteries and correctly diagnose coronary artery anomalies and normal anatomical variants.

Acknowledgments

The authors thank Professor Ana M. Contreras-Navarro for her guidance in preparing and writing this scientific paper.

Funding

This research received no external funding.

Conflicts of interest

The authors declare no conflicts of interest.

Ethical disclosures

Protection of individuals. This study complied with the Declaration of Helsinki (1964) and its amendments.

Confidentiality of data. The authors declare that they followed their center's protocol for sharing patient data.

Right to privacy and informed consent. The authors declare that there are no ethical disclosures since humans' confidential information was not presented.


Use of artificial intelligence. The authors did not use generative artificial intelligence to prepare this manuscript and/or create tables, figures, or figure legends.

REFERENCES

1. Tso JV, Cantu SM, Kim JH. Case Series of Coronary Artery Anomalies in Athletes: Challenges in Clinical Management and Sports Eligibility. *JACC Case Rep.* 2022;4(17):1074-1079. doi: 10.1016/j.jaccas.2022.06.014.
2. Cheezum MK, Liberthson RR, Shah NR, Villines TC, O'Gara PT, Landzberg MJ, et al. Anomalous Aortic Origin of a Coronary Artery From the Inappropriate Sinus of Valsalva. *J Am Coll Cardiol.* 2017;69(12):1592-1608. doi: 10.1016/j.jacc.2017.01.031.
3. Locatelli E, Lisi C, Monti L, Catapano F, Francone M. Advanced cardiac imaging in preventing sudden cardiac death in athletes. *J Mex Fed Radiol Imaging.* 2023;2(4):226-237. doi: 10.24875/JMEXFRI.M23000061.
4. Bigler MR, Kadner A, Rüber L, Ashraf A, Windecker S, Siepe M, et al. Therapeutic Management of Anomalous Coronary Arteries Originating From the Opposite Sinus of Valsalva: Current Evidence, Proposed Approach, and the Unknowing. *J Am Heart Assoc.* 2022;11(20):e027098. doi:10.1161/JAHA.122.027098.
5. Neves PO, Andrade J, Monção H. Coronary anomalies: what the radiologist should know. *Radiol Bras.* 2015;48(4):233-241. doi: 10.1590/0100-3984.2014.0004.

6. Kim SY, Seo JB, Do KH, Heo JN, Lee JS, Song JW, et al. Coronary artery anomalies: classification and ECG-gated multi-detector row CT findings with angiographic correlation. *Radiographics*. 2006;26(2):317-333. doi:10.1148/rg.262055068.
7. Gentile F, Castiglione V, De Caterina R. Coronary Artery Anomalies. *Circulation*. 2021;144(12):983-996. doi:10.1161/CIRCULATIONAHA.121.055347.
8. Gráni C, Buechel RR, Kaufmann PA, Kwong RY. Multimodality Imaging in Individuals With Anomalous Coronary Arteries. *J Am Coll Cardiol Img*. 2017;10(4):471-481. doi: 10.1016/j.jcmg.2017.02.004.
9. Stout KK, Daniels CJ, Aboulhosn JA, Bozkurt B, Broberg CS, Colman JM, et al. 2018 AHA/ACC Guideline for the Management of Adults with Congenital Heart Disease: Executive Summary: A Report of the American College of Cardiology/American Heart Association Task Force on Clinical Practice Guidelines. *J Am Coll Cardiol*. 2019;73(12):1494-1563. doi:10.1016/j.jacc.2018.08.1028.
10. Bigler MR, Ashraf A, Seiler C, Praz F, Ueki Y, Windecker S, et al. Hemodynamic Relevance of Anomalous Coronary Arteries Originating From the Opposite Sinus of Valsalva-In Search of the Evidence. *Front Cardiovasc Med*. 2021;7(591326):1-15. doi: 10.3389/fcvm.2020.591326.
11. Machida H, Tanaka I, Fukui R, Shen Y, Ishikawa T, Tate E, et al. Current and Novel Imaging Techniques in Coronary CT. *Radiographics*. 2015;35(4):991-1010. doi: 10.1148/rg.2015140181.
12. Fuchs TA, Stehli J, Bull S, Dougoud S, Clerc OF, Herzog BA, et al. Coronary computed tomography angiography with model-based iterative reconstruction using a radiation exposure similar to chest X-ray examination. *Eur Heart J*. 2014;35(17):1131-1136. doi:10.1093/eurheartj/ehu053.
13. Ben-Dor I, Weissman G, Rogers T, Slack M, Pichard A, Ben-Dor N, et al. Catheter Selection and Angiographic Views for Anomalous Coronary Arteries: A Practical Guide. *JACC Cardiovasc Interv*. 2021;14(9):995-1008. doi: 10.1016/j.jcin.2021.01.054.
14. Pérez-Pomares JM, de la Pompa JL, Franco D, Henderson D, Ho SY, Houyel L, et al. Congenital coronary artery anomalies: a bridge from embryology to anatomy and pathophysiology—a position statement of the development, anatomy, and pathology ESC Working Group. *Cardiovasc Res*. 2016;109(2):204-216. doi: 10.1093/cvr/cvv251.
15. Ludhwani D, Woo V. Anomalous origin of left main coronary artery from right coronary artery in a patient presenting with inferior wall myocardial infarction: a case report and literature review. *Eur Heart J Case Rep*. 2019;3(4):1-6. doi: 10.1093/ehjcr/ytz169.
16. Davis JA, Cecchin F, Jones TK, Portman MA. Major coronary artery anomalies in a pediatric population: incidence and clinical importance. *J Am Coll Cardiol*. 2001;37(2):593-597. doi: 10.1016/s0735-1097(00)01136-0.
17. Angelini P. Coronary artery anomalies: an entity in search of an identity. *Circulation*. 2007;115(10):1296-1305. doi:10.1161/CIRCULATIONAHA.106.618082.
18. Lee HJ, Hong YJ, Kim HY, Lee J, Hur J, Choi BW, et al. Anomalous origin of the right coronary artery from the left coronary sinus with an interarterial course: subtypes and clinical importance. *Radiology*. 2012;262(1):101-108. doi: 10.1148/radiol.11110823.
19. Yuan SM. Anomalous origin of coronary artery: taxonomy and clinical implication. *Rev Bras Cir Cardiovasc*. 2014;29(4):622-9. doi:10.5935/1678-9741.20140109.
20. Mawson JB. Congenital heart defects and coronary anatomy. *Tex Heart Inst J*. 2002;29(4):279-289.
21. Abbara S, Achenbach S & Rajiah P. CT and MR in Cardiology. 1st edition. ELSEVIER. Manitoba, Canada. 2019.
22. Agarwal PP, Dennie C, Pena E, Nguyen E, LaBounty T, Yang B, et al. Anomalous Coronary Arteries That Need Intervention: Review of Pre- and Postoperative Imaging Appearances. *Radiographics*. 2017;37(3):740-757. doi: 10.1148/rg.2017160124.
23. Möhlenkamp S, Hort W, Ge J, Erbel R. Update on myocardial bridging. *Circulation*. 2002;106(20):2616-2622. doi:10.1161/01.cir.0000038420.14867.7a.
24. Hlavacek A, Loukas M, Spicer D, Anderson RH. Anomalous origin and course of the coronary arteries. *Cardiol Young*. 2010; 20 Suppl 3:20-25. doi:10.1017/S1047951110001058.
25. Baumgartner H, De Backer J, Babu-Narayan SV, Budts W, Chessa M, Diller GP, et al. 2020 ESC Guidelines for the management of adult congenital heart disease. *Eur Heart J*. 2021;42(6):563-645. doi:10.1093/eurheartj/ehaa554.

Intraobserver and interobserver agreement of US findings in suspected lymph node metastasis in papillary thyroid carcinoma

Marco G. Vivas-Baizabal¹ ^{*}, Patricia B. Bolado-Garcia², Mary Y. Ortega-Aranda¹
and Jessica D. Chi-Cauich¹

¹Diagnostic and Therapeutic Imaging Department; ²Research Department. Hospital de Especialidades del Centro Medico Nacional "Ignacio Garcia Tellez"; Instituto Mexicano del Seguro Social, Merida, Yucatan, Mexico

ABSTRACT

The reproducibility of ultrasound findings of suspected neck lymph node (LN) metastases in patients with papillary thyroid carcinoma (PTC) has not been sufficiently addressed. This prospective cohort study evaluated the intra- and interobserver agreement of ultrasound findings of suspected malignancy in neck LNs in patients with PTC. The US images were evaluated twice in a blinded, randomized, and independent manner by radiologists. Round morphology, absence of fatty hilum, echogenicity looking like thyroid tissue, microcalcifications, and peripheral vascularity were evaluated. Cohen's kappa and Light's kappa were used to determine intraobserver and interobserver agreement, respectively. Three radiologists with a mean experience of 6.7 ± 4.7 years in interpreting neck US assessed 114 ultrasound LN images. The ultrasound features with the highest intraobserver agreement were round morphology ($\kappa = 0.63$) and peripheral vascularity ($\kappa = 0.67$), both of which showed substantial agreement. Interobserver agreement was slight for round morphology ($\kappa = 0.16$), absence of fatty hilum ($\kappa = 0.09$), and echogenicity looking like thyroid tissue ($\kappa = 0.09$). There was moderate agreement for microcalcifications ($\kappa = 0.43$) and peripheral vascularity ($\kappa = 0.49$). The range of interobserver and intraobserver agreement of ultrasound findings suggestive of PTC metastasis to LNs was wide, even unacceptable, in the same radiologist and between radiologists.

Keywords: Malignant lymphadenopathy. Neck ultrasound. Papillary thyroid carcinoma. Intraobserver agreement. Interobserver agreement.

INTRODUCTION

Papillary thyroid carcinoma (PTC) is the most common histological thyroid malignancy (90%). Due to abundant cervical lymphatic drainage, the incidence of neck lymph node (LN) metastases is approximately 60–70%¹. Ultrasound is the most widely accepted initial imaging modality for preoperative detection of metastatic LN due to its accessibility, lack of radiation, and low cost. Ultrasound is more specific for central, lateral, and whole cervical LN assessment². Several ultrasonographic

features associated with metastatic LN, such as round morphology, loss of fatty hilum, hyperechogenicity, microcalcifications, peripheral vascularity, and cystic appearance, have been defined³.

Ultrasound examination has limitations as it depends on the operator's experience. Reproducibility is an important element of its diagnostic performance, but reports in the field of radiology are scarce. This study evaluated the intraobserver and interobserver agreement of ultrasound findings of suspected malignancy in neck LNs in patients with PTC.

*Corresponding author:

Marco G. Vivas-Baizabal
E-mail: genarobaizabal85@gmail.com

Received for publication: 30-10-2023

Accepted for publication: 17-01-2024

DOI: 10.24875/JMEXFRI.M24000071

Available online: 10-07-2024

J Mex Fed Radiol Imaging. 2024;3(2):115-121

www.JMeXFRI.com

2696-8444 / © 2024 Federación Mexicana de Radiología e Imagen, A.C. Published by Permanyer. This is an open access article under the CC BY-NC-ND (<https://creativecommons.org/licenses/by-nc-nd/4.0/>).

MATERIALS AND METHODS

This prospective cohort study was conducted between October and November 2022 in the Department of Radiology and Imaging of the Hospital de Especialidades of the Centro Medico Nacional “Ignacio García Tellez” of the Instituto Mexicano del Seguro Social in Merida, Yucatan, Mexico. A convenience sample of radiologists with the following characteristics was selected: current certification by the Mexican Council of Radiology and Imaging, affiliation with the hospital where the study was conducted, three or more years of experience in US neck examination, and training in interventional radiology. The institutional ethics and health research committees approved the study, and participants signed an informed consent form.

Study development and variables

Sex, age, and years of experience performing US neck examinations and training in interventional radiology were recorded.

Five ultrasonographic features suggestive of malignant LNs were assessed³:

Round shape: the relationship between the long and short axis of the LN less than 2 obtained in a longitudinal section⁴⁻⁶.

Absence of fatty hilum: absence or non-visualization of the echogenic hilum⁴⁻⁶.

Echogenicity looking like thyroid tissue: determined by comparison with thyroid parenchyma⁴⁻⁶.

Microcalcifications: punctate echogenic foci with or without posterior acoustic shadowing⁴⁻⁶.

Peripheral vascularity: Doppler flow signal in the periphery of the LN⁴⁻⁶.

US image samples

We selected static US grayscale and color Doppler images of neck LNs from patients with PTC diagnosed with neck LN metastases by preoperative FNA and confirmed by surgery. The minimum resolution was 300 dots per inch (DPI). Images with incomplete visualization of the LN of interest were excluded. Images were selected according to the following criteria: acquired with Acuson S3000 ultrasound equipment (Siemens Medical Solutions, Philadelphia, PA. USA) by a radiologist certified by the Mexican Council of Radiology and Imaging (MVB) with 12 years of experience in radiology and 6 years of experience in obtaining neck biopsies. The radiologist was the reference standard based on

Table 1. Intraobserver agreement of US LN findings suggestive of papillary thyroid carcinoma metastasis

Description	Reader	Cohen's kappa (95% CI)	Parameter
Round morphology	1	0.63 (0.49-0.77)	Substantial
	2	0.50 (0.33-0.66)	Moderate
	3	0.04 (0.01-0.07)	Slight
Absence of fatty hilum	1	0.27 (0.06-0.48)	Fair
	2	0.50 (0.28-0.71)	Moderate
	3	0.31 (0.15-0.48)	Fair
Echogenicity looking like thyroid tissue	1	0.36 (0.14-0.57)	Fair
	2	0.16 (0.02-0.30)	Slight
	3	0.47 (0.11-0.83)	Moderate
Microcalcifications	1	0.40 (0.16-0.63)	Moderate
	2	0.60 (0.30-0.89)	Moderate
	3	0.44 (0.15-0.73)	Moderate
Peripheral vascularity	1	0.56 (0.41-0.70)	Moderate
	2	0.60 (0.45-0.74)	Moderate
	3	0.67 (0.51-0.83)	Substantial

CI: confidence interval; LN: lymph node; US: ultrasound.

the highest experience of the evaluators. The images were selected by a radiologist (MVB) from the PACS WebServex Archiving and Communication System (Compañía Mexicana de Radiología, Queretaro, Qro. México).

Structure of the questionnaire

A multiple-choice questionnaire (Table 1, Supplementary Material) was used. The readers selected ultrasound finding(s) with suspected malignancy identified in the image³. Round morphology, fatty hilum, thyroid-like echogenicity, microcalcifications, and peripheral vascularity were assessed and recorded on each image. Images were static, and observers made no measurements or changes to the imaging parameters.

Procedure for assessing intraobserver and interobserver agreement

Readers were informed that the images were of patients diagnosed with PTC. No additional information about the histopathological LN findings was provided. Participants selected each of the suspicious features for malignancy on the displayed LN findings of the randomly

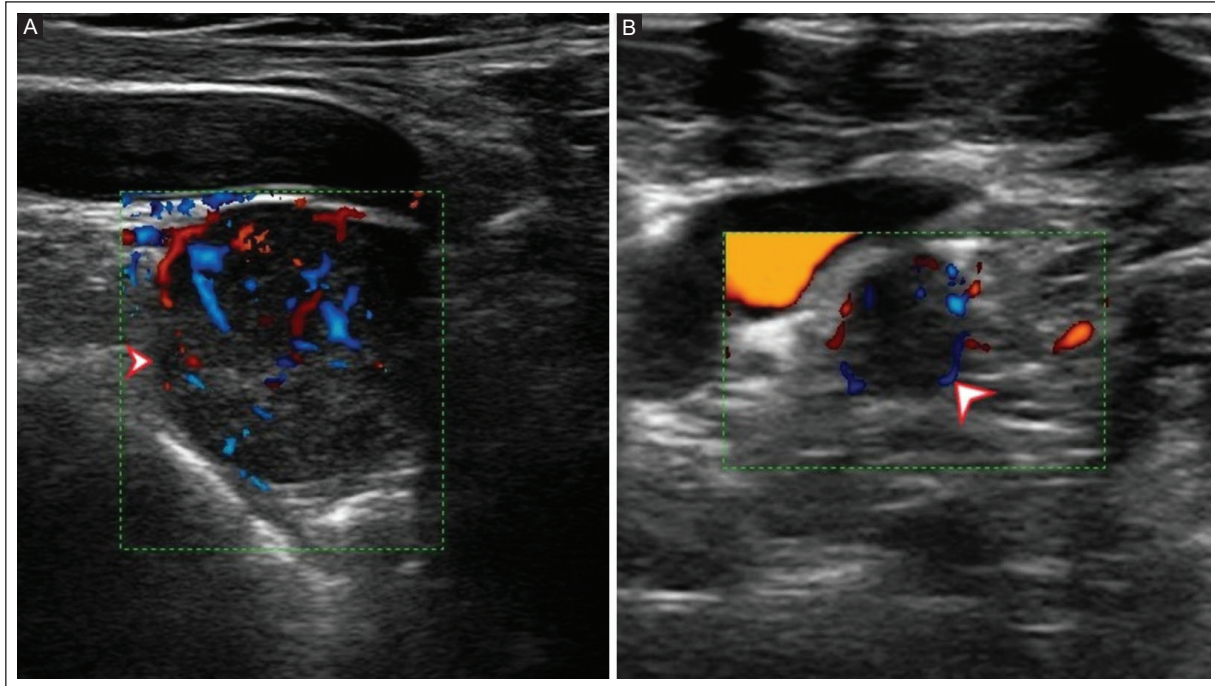


Figure 1. US grayscale and color Doppler examination of a 46-year-old woman with a diagnosis of PTC. **A-B:** LN with **round morphology** (arrowheads), absent fatty hilum, and transcortical and peripheral vascularity.

LN: lymph node; PTC: papillary thyroid carcinoma; US: ultrasound.

presented US images on a conventional computer via a web-based questionnaire in approximately 120 min. Each participant answered the questionnaire individually in a booth without interruption.

Two weeks after the first evaluation, each participant repeated this activity with the same images in a randomized order that differed from the first evaluation. In this second evaluation, the radiologists examined the images individually and independently without knowing the results of their first evaluation. The evaluation conditions were the same.

Statistical analysis

Descriptive statistics of central tendency and dispersion were performed. Cohen's kappa was calculated for intraobserver agreement and Light's kappa for interobserver agreement with 95% confidence interval (CI). Kappa coefficients were classified as follows: less than 0.00 = poor agreement; 0.00-0.20 = slight; 0.21-0.40 = fair; 0.41-0.60 = moderate; 0.61-0.80 = substantial; and 0.81-1.00 = almost perfect. A p -value ≤ 0.05 was statistically significant. The R version 4.2.3 statistical software (R Core Team, Vienna, Austria) and the "irr" package version 0.84.1 were used.

RESULTS

Three readers were included: two men and one woman. The mean age was 39.7 ± 1.5 years, and the mean experience interpreting neck US was 6.7 ± 4.7 years. Each reader evaluated 114 LN images of 114 patients with a PTC diagnosis in a blinded, randomized, and independent manner. Figures 1 through 4 show LNs from patients with a histopathological diagnosis of PTC with ultrasound findings suggestive of malignancy: round morphology, absence of fatty hilum, echogenicity looking like thyroid tissue, microcalcifications, and peripheral vascularity.

Intraobserver agreement

Table 2 shows the intraobserver agreement of the three readers.

Reader 1, a 40-year-old man with 12 years of experience in US examination of the neck and 1 year of training in interventional radiology, showed fair to substantial agreement in the five US findings assessed. There was substantial agreement ($\kappa = 0.63$, 95% CI 0.49-0.77) with round morphology, while microcalcifications ($\kappa = 0.40$, 95% CI 0.16-0.63) and peripheral vascularity ($\kappa = 0.56$, 95% CI 0.41-0.70) showed

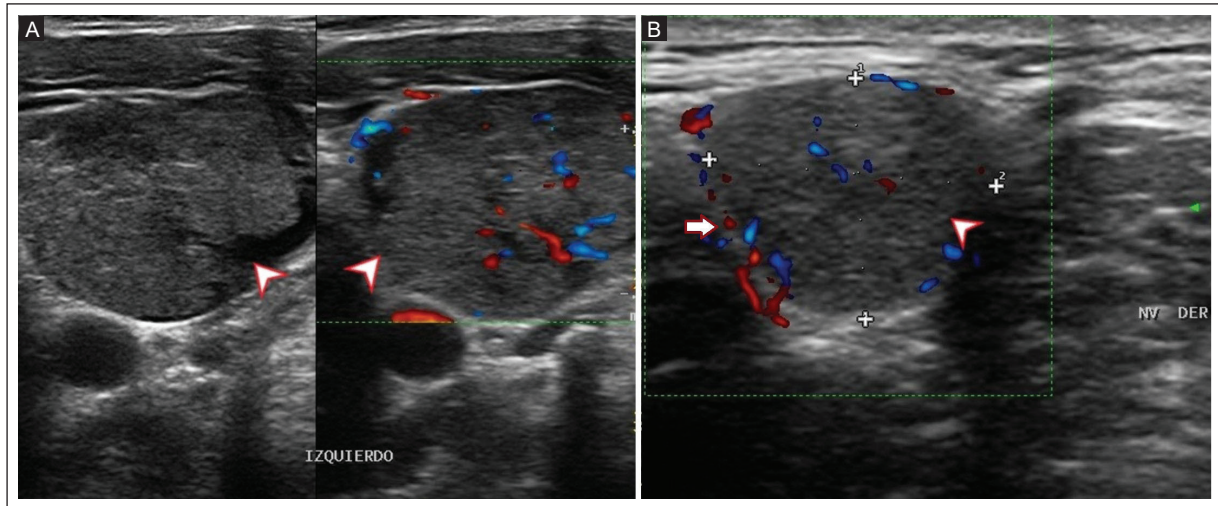


Figure 2. US in grayscale and color Doppler. **A:** a 48-year-old woman diagnosed with PTC; LN with round morphology, **absent fatty hilum** (arrowhead), and transcortical and peripheral vascularity. **B:** a 52-year-old woman with a diagnosis of PTC; LN with round morphology (arrowhead), hypoechogenic, absent fatty hilum, and transcortical and **peripheral vascularity** (arrow).
LN: lymph node; PTC: papillary thyroid carcinoma; US: ultrasound.

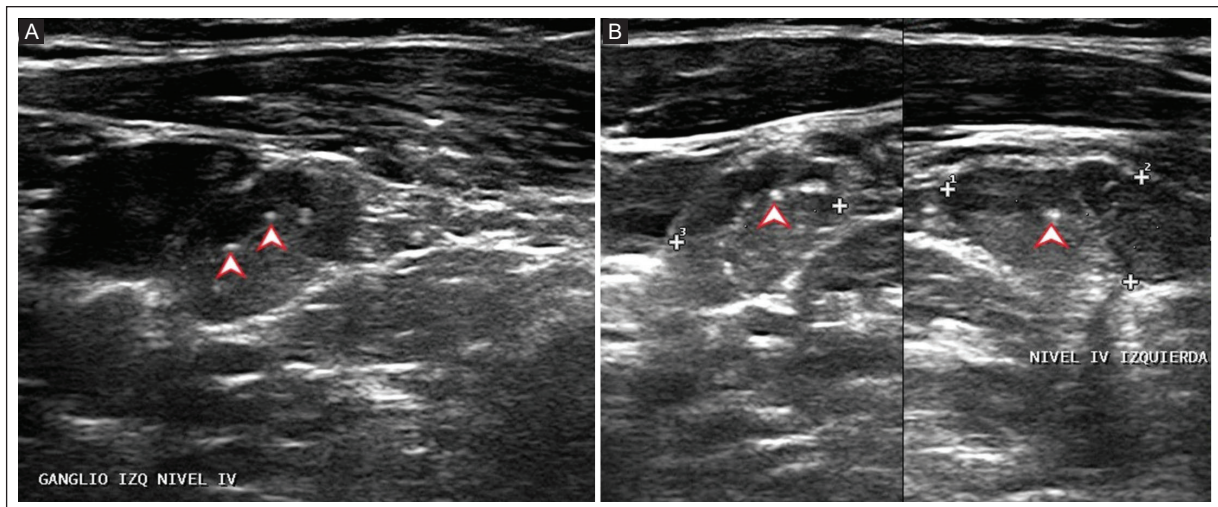


Figure 3. US in grayscale, longitudinal, and transverse view in a 49-year-old woman with a diagnosis of PTC. **A-B:** LN with ovoid morphology, hyperechogenic, and **microcalcifications** inside (arrowheads).
LN: lymph node; PTC: papillary thyroid carcinoma; US: ultrasound.

moderate agreement. Absence of fatty hilum ($\kappa = 0.27$, 95% CI 0.06-0.48) and echogenicity looking like thyroid tissue ($\kappa = 0.36$, 95% CI 0.14-0.57) showed fair agreement.

Reader 2, a 41-year-old woman with 5 years of experience in US neck examination and 1 year of training in interventional radiology, showed slight to moderate agreement in the five US findings assessed. There was slight agreement for echogenicity looking like thyroid

tissue ($\kappa = 0.16$, 95% CI 0.02-0.30), while agreement was moderate for round morphology ($\kappa = 0.50$, 95% CI 0.33-0.66), absence of fatty hilum ($\kappa = 0.50$, 95% CI 0.28-0.71), microcalcifications ($\kappa = 0.60$, 95% CI 0.30-0.89), and peripheral vascularity ($\kappa = 0.60$, 95% CI 0.45-0.74).

Reader 3, a 38-year-old man with 7 years of experience in neck US and 3 years in interventional radiology training, showed variable agreement on the five US

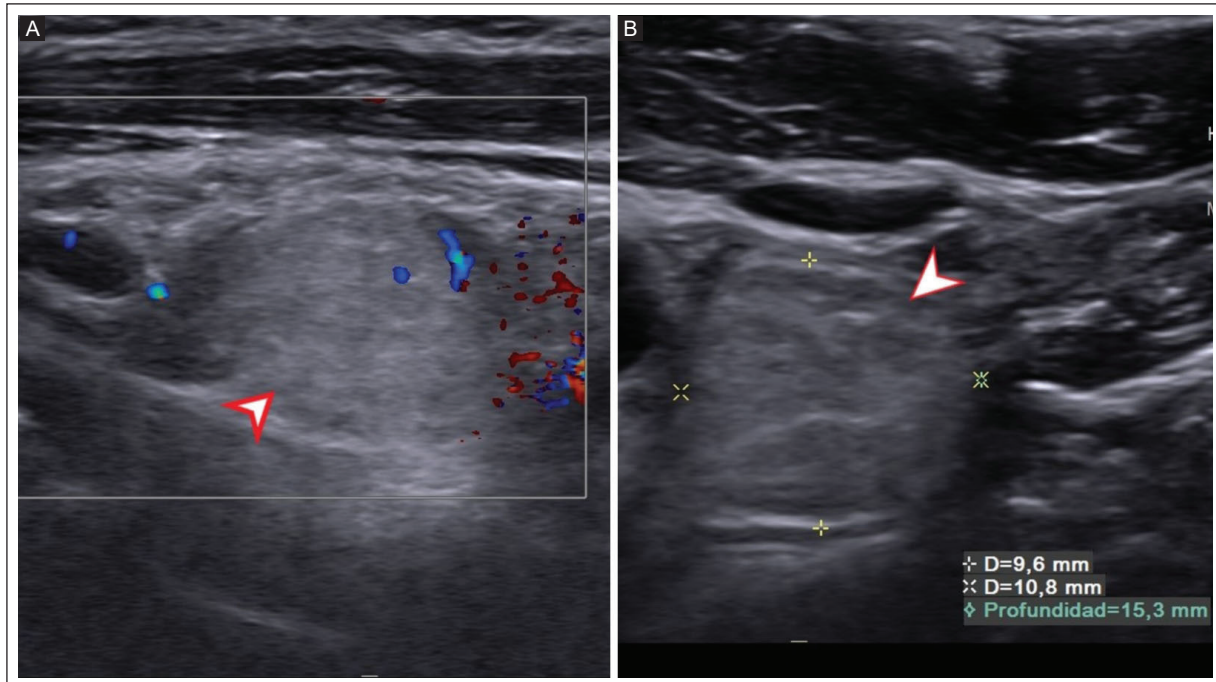


Figure 4. US grayscale and color Doppler, transverse and longitudinal view of a 42-year-old man diagnosed with PTC. **A-B:** LN with round morphology, and **echogenicity looking like thyroid tissue** (arrowheads), absent fatty hilum, and without peripheral vascularity.

LN: lymph node; PTC: papillary thyroid carcinoma; US: ultrasound.

Table 2. Interobserver agreement of LN US findings suggestive of papillary thyroid carcinoma metastasis

Description	Light's kappa (95% CI)	Parameter
Round morphology	0.16 (0.10-0.24)	Slight
Absence of fatty hilum	0.09 (0.01-0.30)	Slight
Echogenicity looking like thyroid tissue	0.09 (0.02-0.16)	Slight
Microcalcifications	0.43 (0.22-0.66)	Moderate
Peripheral vascularity	0.49 (0.37-0.59)	Moderate

CI: confidence interval; LN: lymph node; US: ultrasound.

findings assessed. Substantial agreement was found for peripheral vascularity ($\kappa = 0.67$, 95% CI 0.51-0.83), while moderate agreement was found for echogenicity looking like thyroid tissue ($\kappa = 0.47$, 95% CI 0.11-0.83) and microcalcifications ($\kappa = 0.44$, 95% CI 0.15-0.73). Slight agreement was found for round morphology ($\kappa = -0.04$, 95% CI 0.01-0.07).

There was no direct correlation between years of experience in neck US examination and intraobserver agreement of the three readers; therefore, more years of experience was not related to greater agreement between the first and second assessments.

Interobserver agreement

Table 2 shows the interobserver agreement of the three readers. Agreement was slight for round morphology ($\kappa = 0.16$, 95% CI 0.10-0.24), absence of fatty hilum ($\kappa = 0.09$, 95% CI -0.01 to 0.30), and echogenicity looking like thyroid tissue ($\kappa = 0.09$, 95% CI 0.02-0.16), while there was moderate agreement for microcalcifications ($\kappa = 0.43$, 95% CI 0.22-0.66) and peripheral vascularity ($\kappa = 0.49$, 95% CI 0.37-0.59). No substantial agreement was reached between the three readers regarding any US feature.

DISCUSSION

In this study, intraobserver agreement of US findings with suspected LN metastasis in patients with PTC was variable, ranging from slight to substantial. In contrast, interobserver agreement varied from slight to moderate. This report showed a wide range, even unacceptable, of agreement between the same radiologist and between radiologists. Therefore, reporting suspicious findings of LN malignancy in PTC patients may be of less help in the decision to perform an LN biopsy.

Intraobserver agreement of US findings suspicious for LN metastasis has not been described. The features

with the highest intraobserver agreement in our study were round morphology ($\kappa = 0.63$, 95% CI 0.49-0.77) and peripheral vascularity ($\kappa = 0.67$, 95% CI 0.51-0.83), which showed substantial agreement. In 2 out of 3 readers, the intraobserver agreement was slight to fair in three assessed features. Our results may be concerning in clinical practice and related to unclear definitions, leading to different interpretations by the same radiologist and unrelated to years of experience in US neck examination. The use of artificial intelligence in the evaluation of LNs with suspected malignancy may increase diagnostic accuracy. However, its application requires a high learning curve for personnel to familiarize themselves with the formulas and algorithms. Clinical studies are needed to validate the results to determine precision and reproducibility⁷.

Few studies have reported interobserver agreement of ultrasound findings for suspicious LN metastases of PTC^{8,9}. In a study by Ryu et al.⁸, 291 patients from a single institution, with ultrasound features suspicious for LN malignancy were retrospectively evaluated by two board-certified radiologists with 11 and 4 years of experience in head and neck ultrasound. Images were assessed for seven ultrasound features. The mean interobserver agreement for margin, echogenicity, echogenic hilum, macroscopic necrosis, and intranodal vascular pattern was moderate ($\kappa = 0.58, 0.49, 0.51, 0.54,$ and 0.47 , respectively), and for shape and calcifications, it was substantial ($\kappa = 0.72$ and 0.73 , respectively). In our study, only five LN features were evaluated. Our results were comparable only for microcalcifications and vascular patterns, showing moderate interobserver agreement. On the other hand, the images in the study by Ryu et al.⁸ were analyzed in real-time, in contrast to our study, where only static images were available.

It has been proposed that a scoring system that weighs various ultrasound findings for suspected malignancy may be more accurate in predicting malignant LN than a single feature^{9,10}. Interestingly, Flores et al.⁹ showed substantial interobserver agreement ($\kappa = 0.71$) between two radiologists with 10 and 11 years of experience using the Ultrasound Neck Node Reporting and Data System (UNN-RADS)¹⁰. by combining seven ultrasound descriptors (round or lobulated shape, noncircumscribed margin, hyperechogenicity, echogenic hilum < 25% or absent, cystic degeneration, presence of calcification, and non-hilar vascular pattern) that are suspicious for malignancy and increase the predictability of metastatic LN, with scores ranging from 0 to 3 points, allowing categorization into five different risk

categories. The sum of the scores determines the UNN-RADS category according to the total score of the ultrasonographic descriptors that are suspicious for LN malignancy: Category 1 – benign with a score of 3 or less; Category 2 – probably benign with 4 to 5 points; Category 3 – mildly suspicious for malignancy with 6 to 8 points; Category 4 – moderately suspicious for malignancy with 9 to 11 points, and Category 5 – highly suspicious of malignancy with 12 or more points¹⁰. In contrast, in our study, the highest level of agreement was moderate for two individual features of LN malignancy, namely, microcalcifications and peripheral vascularity. One of the possible reasons for the lower interobserver agreement in our study could be that we assessed fewer characteristics (5 versus 7) as single qualitative features and the unclear definitions of the terms used.

The strengths of this study are the prospective design and the sufficient sample size to determine intraobserver and interobserver agreement. The limitations are related to the analysis of static images. On the other hand, it was performed at a single center. Other suspicious features for malignancy, such as cortical or cystic changes, were not considered, as only one patient in the study population had this US feature.

CONCLUSION

In our study, intraobserver and interobserver agreement of ultrasound findings suggestive of LN metastasis in patients with PTC was variable, ranging from slight to substantial. Our results show wide variability and poor reproducibility of ultrasound assessment of metastatic LN in patients with PTC. US of the neck is commonly used to detect LN metastasis, and suspicious findings have been widely described but the results of this study suggest that reproducibility is poor. We recommend that reproducibility analyses be included in the quality assessment of diagnostic imaging and evaluation of the impact of standardized terminology to describe suspicious findings of LN metastasis in PTC, such as the UNN-RADS classification¹⁰.

Acknowledgments

The authors thank Professor Ana M. Contreras-Navarro for her guidance in preparing and writing this scientific paper. This original research in the Radiology Specialty field was an awarded thesis at the Primera Convocatoria Nacional 2023, "Las Mejores Tesis para Publicar en el JMeXFRI."

Funding

This research received no external funding.

Conflicts of interest

The authors declare that they have no conflicts of interest.

Ethical disclosures

Protection of Individuals. This study complied with the Declaration of Helsinki (1964) and its subsequent amendments.

Confidentiality of Data. The authors declare they followed their center's protocol for sharing patient data.

Right to privacy and informed consent. Informed consent was obtained from the participants.

Use of artificial intelligence. The authors did not use generative artificial intelligence to prepare this manuscript and/or create tables, figures, or figure legends.

Supplementary data

Supplementary data are available in the Journal online DOI: 10.24875/JMEXFRI.M24000071. These data are provided by the corresponding author and published online for the reader's benefit. The contents of supplementary data are the sole responsibility of the authors.

REFERENCES

1. Li QL, Ma T, Wang ZJ, Huang L, Liu W, Chen M et al. The value of contrast-enhanced ultrasound for the diagnosis of metastatic cervical lymph nodes of papillary thyroid carcinoma: A systematic review and meta-analysis. *J Clin Ultrasound*. 2022;50(1):60-69. doi:10.1002/jcu.23073.
2. Xing Z, Qiu Y, Yang Q, Yu Y, Liu J, Fei Y, et al. Thyroid cancer neck lymph nodes metastasis: Meta-analysis of US and CT diagnosis. *Eur J Radiol*. 2020;129:109103. doi:10.1016/j.ejrad.2020.109103.
3. Haugen BR, Alexander EK, Bible KC, Doherty GM, Mandel SJ, Nikiforov YE, et al. 2015 American Thyroid Association Management Guidelines for Adult Patients with Thyroid Nodules and Differentiated Thyroid Cancer: The American Thyroid Association Guidelines Task Force on Thyroid Nodules and Differentiated Thyroid Cancer. *Thyroid*. 2016;26(1):1-133. doi:10.1089/thy.2015.0020.
4. Leenhardt L, Erdogan MF, Hegedus L, Mandel SJ, Paschke R, Rago T, et al. 2013 European thyroid association guidelines for cervical ultrasound scan and ultrasound-guided techniques in the postoperative management of patients with thyroid cancer. *Eur Thyroid J*. 2013;2(3):147-159. doi:10.1159/000354537.
5. Durante C, Hegedüs L, Czarniecka A, Paschke R, Russ G, Schmitt F, et al. 2023 European Thyroid Association Clinical Practice Guidelines for thyroid nodule management. *Eur Thyroid J*. 2023;12(5):e230067. doi:10.1530/ETJ-23-0067.
6. Chung SR, Baek JH, Rho YH, Choi YJ, Sung TY, Song DE et al. Sonographic Diagnosis of Cervical Lymph Node Metastasis in Patients with Thyroid Cancer and Comparison of European and Korean Guidelines for Stratifying the Risk of Malignant Lymph Node. *Korean J Radiol*. 2022;23(11):1102-1111. doi: 10.3348/kjr.2022.0358.
7. Liang XW, Cai YY, Yu JS, Liao JY, Chen ZY. Update on thyroid ultrasound: a narrative review from diagnostic criteria to artificial intelligence techniques. *Chin Med J*. 2019;132(16):1974-1982. doi: 10.1097/CM9.0000000000000346.
8. Ryu KH, Lee KH, Ryu J, Baek HJ, Kim SJ, Jung HK et al. Cervical Lymph Node Imaging Reporting and Data System for Ultrasound of Cervical Lymphadenopathy: A Pilot Study. *AJR Am J Roentgenol*. 2016; 206(6):1286-1291. doi: 10.2214/AJR.15.15381.
9. Flores-Palomares O, Macias-Cervantes H, Maya-Martinez O, Hernandez-Gonzalez M, Velazquez-Fernandez L. Validation of the Ultrasound Neck Node Reporting and Data System (UNN-RADS) for predicting lymph node metastases in thyroid cancer patients. *J Mex Fed Radiol Imaging*. 2024;3(1):17-26. doi:10.24875/JMEXFRI.23000025.
10. Sarda-Inman ED, Valdez-Rojas AM. Ultrasound Neck Node Reporting and Data System (UNN-RADS) for lymphadenopathy: A structured report. *J Mex Fed Radiol Imaging*. 2022;1(3):151-163. doi:10.24875/JMEXFRI.M22000020.

Interobserver agreement between radiologists and artificial intelligence in mammographic breast density classification

Claudia M. Delsol-Perez^{1,2} , Alix D. Reyes-Mosqueda^{1,2}, Tania A. Rios-Rodriguez^{1,2},
David F. Perez-Montemayor^{1,2*} 

¹Centro de Imagenología Integral IMAX; ²Instituto de Estudios Superiores de Tamaulipas, Universidad Anahuac. Tampico, Tamaulipas, Mexico

ABSTRACT

Artificial intelligence (AI) has been proposed as a tool for assessing mammographic breast density (MBD). This study aimed to evaluate the agreement of MBD classification between four radiologists (human readers [HRs]) with different years of experience in breast imaging and the AI Lunit INSIGHT MMG. This cross-sectional study was conducted with a convenience sample of radiologists trained in breast imaging who assessed MBD screening mammograms of asymptomatic women 35 years or older using BI-RADS descriptors. Cohen's kappa determined the agreement between the HRs and AI. A total of 192 women with a mean age of 55.4 ± 31.8 years (range 37-82 years) were included. Interobserver agreement between HRs and AI varied in Category a but was substantial in Category b (HR1 $k = 0.729$, HR2 $k = 0.718$, HR3 $k = 0.768$, and HR4 $k = 0.672$) and in Category c, HR1, HR2, and HR3 had substantial agreement ($k = 0.728$, $k = 0.697$, and $k = 0.738$, respectively) and HR4 had moderate agreement ($k = 0.578$), while in Category d, it was mostly moderate. HRs and AI agreements varied from fair to substantial. HRs with more years of experience in breast image interpretation had a lower agreement with AI for MBD classification than HRs with less time.

Keywords: Artificial intelligence. Digital mammography. Mammography breast density. Human readers.

INTRODUCTION

Mammographic breast density (MBD) is assessed visually in clinical practice¹⁻³. The Breast Imaging Reporting and Data System (BI-RADS) is a commonly used method for assessing MBD. However, it is subjectively based on the examiner's perception and is time-consuming^{3,4}. The reproducibility of the MBD classification is important because hyperdense breasts are a risk factor for breast cancer⁵. Variable interobserver agreement has been reported, with kappa values ranging from 0.27 to 0.94^{5,6}. Therefore, the European guidelines for mammography screening recommend double reading of the mammogram by two radiologists⁶.

The performance of artificial intelligence (AI) in interpreting mammograms has recently been evaluated⁷⁻⁹. AI's performance is comparable with human readers (HRs), and a synergistic combination of radiologists and AI has been deemed possible¹⁰. AI can reduce the interpretation volume of mammography screening by replacing one of the two HRs in double readings or triaging mammograms from different risk groups that do not need assessment by one HR⁴. As of December 2021, more than 15 AI software have been approved by the FDA for mammography screening¹¹. The AI Lunit INSIGHT MMG is a computer-aided diagnostic device that assists radiologists in interpreting mammograms¹². This study aimed to evaluate the

*Corresponding author:

David F. Perez-Montemayor
E-mail: dfperez@prodigy.net.mx

Received for publication: 07-01-2024

Accepted for publication: 13-03-2024

DOI: 10.24875/JMEXFRI.M24000074

Available online: 10-07-2024

J Mex Fed Radiol Imaging. 2024;3(2):122-127

www.JMeXFRI.com

2696-8444 / © 2024 Federación Mexicana de Radiología e Imagen, A.C. Published by Permanyer. This is an open access article under the CC BY-NC-ND (<https://creativecommons.org/licenses/by-nc-nd/4.0/>).

agreement of MBD classification between four radiologists (HRs) with different years of experience in breast imaging and the AI Lunit INSIGHT MMG.

MATERIALS AND METHODS

This cross-sectional study was conducted from November 2023 to January 2024 at the Centro de Imagenología Integral IMAX in Tampico, Tamaulipas, Mexico. A convenience sample of radiologists trained in breast imaging was included. The Institutional Research Ethics Committee and the Research Committee approved the study, and participants signed written informed consent.

Study development and variables

The sex and age of the participants and the specialist radiologist’s years of experience and performance of breast imaging examinations were recorded. The MBD of screening mammograms of asymptomatic women 35 years or older was assessed using BI-RADS descriptors¹³, and the agreement on MBD classification between HRs and the AI was recorded.

Image acquisition and analysis protocol

Digital mammography was performed with Lorad Selenia equipment (HOLOGIC, Bedford, MA, USA). Four images stored in the PACS system (SecureView, Diagnostic Workstation Bedford, MA, USA) were analyzed for each case. These images included two oblique mediolateral (OML) and craniocaudal two (CC) views of the right and left breast. Four HRs with high breast specialization evaluated the images. MBD was classified according to BI-RADS lexicon¹³ based on the percentage of fibroglandular tissue: (a) almost entirely fat; (b) scattered fibroglandular tissue; (c) heterogeneously dense; and (d) extremely dense¹⁴.

Artificial intelligence

The mammogram images were analyzed with AI Lunit INSIGHT MMG (version 1.1.1.8, Lunit Inc., Gangnam-Gu, Seoul, RK). The AI LUNIT INSIGHT system classifies MBD on a 10-point scale, where 1 indicates fatty tissue and 10 extremely dense breast tissue¹². Scores of 1 or 2 correspond to Category a; 3, 4, or 5 to Category b; 6, 7, or 8 to Category c; and 9 or 10 to Category d. The score was calculated according to the MBD composition.

Table 1. Characteristics of four radiologists (HRs)

HR	Sex	Age (years)	Years of experience in imaging examination	Years of experience in breast imaging examination
1	Female	31	5	1
2	Female	48	16	1
3	Female	30	7	2
4	Male	64	34	31

HRs: human readers.

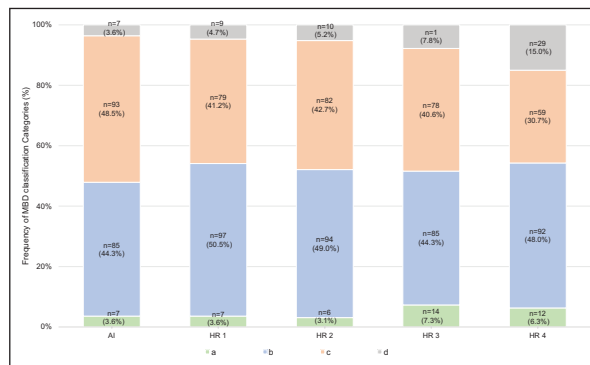


Figure 1. Comparison of MBD classification by AI and four HRs using BI-RADS: Category a, almost entirely fat; Category b, scattered fibroglandular tissue; Category c, heterogeneously dense; and Category d, extremely dense.

AI: artificial intelligence; BI-RADS: Breast Imaging Reporting and Data System; HRs: human readers; MBD: mammography breast density.

Statistical analysis

Qualitative variables are presented as frequencies and percentages. Cohen’s kappa determined the agreement between the HRs and AI. The *k* agreement scores were interpreted using the following scale: slight = 0.00-0.20; fair = 0.21-0.40; moderate = 0.41-0.60; substantial = 0.61-0.80; and almost perfect = 0.81-1.00. SPSS version 25 (IBM Corp., Armonk, NY, USA) was used.

RESULTS

Table 1 shows the characteristics of the HRs, which included three women and one man. The years of experience interpreting breast images varied and ranged from 1 to 31 years. A total of 192 mammography images were analyzed.

The MBD classification results by AI and the four HRs are shown in Figure 1.

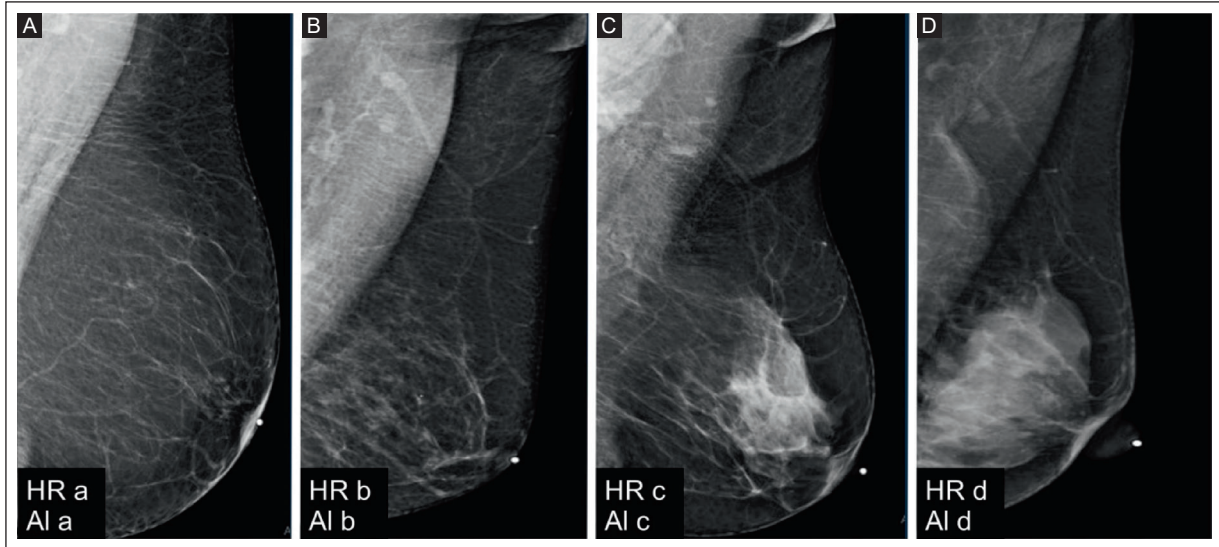


Figure 2. Mammography showed MBD classification between HRs and AI using BI-RADS. **A:** MLO view of the left breast where HR and AI agree on breast density in Category a. **B:** MLO view in which HR and AI agree on breast density in Category b. **C:** MLO view in which HR and AI agree on breast density in Category c. **D:** MLO view in which HR and AI agree on breast density in Category d.

AI: artificial intelligence; BI-RADS: Breast Imaging Reporting and Data System; MBD: mammography breast density; HRs: human readers; MLO: mediolateral oblique.



Figure 3. Mammography showed MBD classification between HR and AI using BI-RADS. **A:** MLO view where HR classified breast density as Category a and AI as Category b. **B:** MLO view in which HR classified breast density as Category b and AI as Category a. **C:** MLO view in which HR classified breast density as Category c and AI as Category d. **D:** MLO view in which HR classified breast density as Category d and AI as Category c.

AI: artificial intelligence; BI-RADS: Breast Imaging Reporting and Data System; HR: human reader; MBD: mammography breast density; MLO: mediolateral oblique.

In Category a, the AI (n = 7), HR1 (n = 7), and HR2 (n = 6) results were comparable, while HR3 and HR4 reported a higher number of patients in this category (14 and 12, respectively).

Category b was variable, with a range of 85-97 patients. The lowest number of cases reported was from AI and HR3 (n = 85), while HR1 reported the highest (n = 97).

Table 2. Interobserver agreement for MBD classification^a by BI-RADS between HRs and AI Lunit INSIGHT MMG.

	HR1 a	HR2 a	HR3 a	HR4 a
AI a, <i>k</i>	0.407	0.444	0.650	0.393
95% CI	(0.281-0.520)	(0.322-0.554)	(0.615-0.762)	(0.288-0.521)
Agreement	Fair	Moderate	Substantial	Fair
	HR1 b	HR2 b	HR3 b	HR4 b
AI b, <i>k</i>	0.729	0.718	0.768	0.672
95% CI	(0.662-0.791)	(0.652-0.782)	(0.701-0.829)	(0.593-0.752)
Agreement	Substantial	Substantial	Substantial	Substantial
	HR1 c	HR2 c	HR3 c	HR4 c
AI c, <i>k</i>	0.728	0.697	0.738	0.578
95% CI	(0.661-0.796)	(0.623-0.774)	(0.683-0.803)	(0.528-0.702)
Agreement	Substantial	Substantial	Substantial	Moderate
	HR1 d	HR2 d	HR3 c	HR4 d
AI d, <i>k</i>	0.479	0.447	0.522	0.351
95% CI	(0.373-0.582)	(0.332-0.562)	(0.462-0.653)	(0.341-0.572)
Agreement	Moderate	Moderate	Moderate	Fair

HR: human reader; AI: artificial intelligence; BI-RADS: Breast Imaging Reporting and Data System; CI: confidence interval; *k*: agreement scores; MBD: mammographic breast density. ^aMBD classification: Category a, almost entirely fat; Category b, scattered fibroglandular tissue; Category c, heterogeneously dense; and Category d, extremely dense.

In Category c, the greatest variability between HRs was observed with a range of 59-82 cases; HR4 reported the lowest number of cases ($n = 59$), while AI reported 93 cases.

In Category d, the results varied, ranging from 7 to 29 cases. AI reported the lowest number ($n = 9$, 3.6%). The number of cases reported was directly related to years of experience interpreting breast images, with HR4 reporting the highest ($n = 29$, 15.0%).

Figure 2 shows the agreement of MBD between HRs and AI using BI-RADS Categories a, b, c, and d, and Figure 3 shows no agreement of MBD between HRs and AI.

Table 2 shows the interobserver agreement between HRs and AI for MBD classification. The agreement was variable in Category a, ranging from fair for HR1 ($k = 0.407$, 95% CI 0.281–0.520) to substantial for HR3 ($k = 0.650$, 95% CI 0.615–0.762).

The agreement between four HRs and AI in Category b was substantial (HR1 $k = 0.729$, 95% CI 0.662-0.791, HR2 $k = 0.718$, 95% CI 0.652–0.782, HR3 $k = 0.768$, 95% CI 0.701-0.829, and HR4 $k = 0.672$, 95% CI 0.593-0.752).

HR1, HR2, and HR3 showed substantial agreement in Category c (HR1 $k = 0.728$, 95% CI 0.661–0.791, HR2

$k = 0.697$, 95% CI 0.623–0.774, and HR3 $k = 0.738$, 95% CI 0.683–0.803, respectively), while HR4 showed moderate agreement ($k = 0.578$, 95% CI 0.528-0.72).

HR1, HR2, and HR3 showed moderate agreement in breast density d (HR1 with $k = 0.470$ and 95% CI 0.373-0.582, HR 2 with $k = 0.447$ and 95% CI 0.332-0.562, and HR 3 with $k = 0.522$ and 95% CI 0.462-0.653) and HR4 fair agreement ($k = 0.351$, 95% CI = 0.341-0.572).

DISCUSSION

The interobserver agreement between HRs and AI for MBD classification varied from fair to substantial in our study. The more years of experience in interpreting breast images, the lower the agreement between AI and HRs. We hypothesize that this may be related to the longer time they had spent interpreting mammograms using the qualitative BI-RADS. In contrast, HRs with less years of experience interpreting mammography images showed higher agreement with the AI. We believe that AI can add value to the interpretation of breast density by HRs.

The interobserver agreement between HRs and AI in MBD classification has been insufficiently addressed.

Alomaim et al.¹⁵ conducted a study with HRs from the United States (US) and the United Kingdom (UK). A total of 250 mammograms were MBD classified according to the BI-RADS system by 49 breast radiologists; 25 with more than 10 years of experience in interpreting breast images were from the US, while 24 were from the UK; 29% (n = 7) had 3 years of experience or less, 33% (n = 8) had 4-9 years of experience, and only 38% (n = 9) had more than 10 years of experience. The MBD classification agreement between US and UK radiologists was substantial ($k = 0.760$). The agreement between the US and UK HRs related to years of experience ranged from fair to substantial for breast density Category a ($k = 0.374$), Category b ($k = 0.501$), Category c ($k = 0.684$), and Category d ($k = 0.635$). These results are compared with those of our study, which showed variable agreement. The interobserver agreement between HRs and AI was substantial and indirectly related to seniority in interpreting mammography images, i.e., the lower the experience in breast imaging, the higher the interobserver agreement. HRs with more seniority with lower agreement may be biased due to the nature and longer time spent interpreting mammograms using the BI-RADS qualitative system. They may benefit from relying on the MBD classification by AI to support their interpretation.

The diagnostic performance of mammography is limited in high breast density (Categories c and d). Therefore, additional imaging examinations are recommended for dense breasts. In our study, there was substantial agreement between four HRs and AI in Category b of MBD (HR1 $k = 0.729$, HR2 $k = 0.718$, HR3 $k = 0.768$, and HR4 $k = 0.672$), whereas in Category c, HRs 1, 2, and 3 had a substantial agreement (HR1 $k = 0.728$, HR2 $k = 0.697$, and HR3 $k = 0.738$), while HR4 had a moderate agreement ($k = 0.578$). Magni et al.¹ reported results comparable with our study. They showed substantial agreement between HRs and AI in 197 mammograms ($k = 0.807$, 95% CI, 0.667-0.947) in non-dense breasts (Categories a and b) and dense breasts (Categories c and d). Interestingly, this agreement in the distinction between non-dense breast and dense breast may benefit patients, as the distinction allows the categorization of suspicious malignant lesions and using complementary imaging studies.

The strength of this study was that we used AI software¹² based on the assessment of a large number of patients. The study has limitations, such as the small number of mammograms evaluated from a single center. In addition, there is no standard reference to validate

MBD classification by HRs and AI, and automation bias due to overconfidence in MBD classification supported by AI was not assessed.

CONCLUSION

The interobserver agreement of MBD classification in our study between four HRs and AI varied from fair to substantial. There was lower agreement between AI and HRs with more years of experience in using the parameters based on conventional BI-RADS qualitative interpretation, while HRs with less years of experience in reading mammograms showed higher agreement with AI. In an ideal scenario, radiologists should correctly integrate the information provided by AI, benefit from the cases where AI makes a better suggestion, ignore cases where AI makes an incorrect prediction, and perform better diagnostic reports than without AI¹⁰. There is growing evidence of the benefits of AI as an aid to radiologists in interpreting mammograms. Prospective cohort studies with a large population are needed.

Acknowledgments

The authors thank Professor Ana M. Contreras-Navarro for her guidance in preparing and writing this scientific paper.

Funding

This research received no external funding.

Conflicts of interest

The authors declare no conflicts of interest.

Ethical disclosures

Protection of Individuals. This study complied with the Declaration of Helsinki (1964) and its amendments.

Confidentiality of Data. The authors declare that they followed their center's protocol for sharing patient data.

Right to privacy and informed consent. Informed consent was obtained from prospectively enrolled participants and waived for retrospectively enrolled patients.

Use of artificial intelligence. The authors did not use generative artificial intelligence to prepare this manuscript and/or create tables, figures, or figure legends.

REFERENCES

1. Magni V, Interlenghi M, Cozzi A, Ali M, Salvatore C, Alcide AA. Development and Validation of an AI-driven Mammographic Breast Density Classification Tool Based on Radiologist. *Radiology Artif Intell.* 2022; 4(2):e210199. doi:10.1148/ryai.210199.
2. PROSPR Consortium. Sprague BL, Conant EF, Onega T, Garcia MP, Beaber EF, Herschorn SD, et al. Variation in Mammographic Breast Density Assessments Among Radiologists in Clinical Practice: A Multicenter Observational Study. *Ann Intern Med.* 2016;165(7):457-464. doi: 10.7326/M15-2934.
3. Moshina N, Roman M, Sebuødegård S, Waade GG, Ursin G, Hofvind S. Comparison of subjective and fully automated methods for measuring mammographic density. *Acta Radiol.* 2018; 59(2):154-160. doi:10.1177/0284185117712540.
4. Larsen M, Olstad CF, Lee CI, Hovda T, Hoff S, Marinuisen M. Performance of an AI System for Breast Cancer Detection on Screening Mammograms from Breast Screen Norway. *Radiology: Artif Intell.* 2024; 1:19. doi.org/10.1148/ryai.230375.
5. Damases CN, Hogg P, McEntee MF. Intercountry analysis of breast density classification using visual grading. *Br J Radiol.* 2017;90(1076): 20170064. doi:10.1259/bjr.20170064.
6. Lee SE, Yoon JH, Son NH, Han K, Moon HJ. Screening in Patients with Dense Breasts: Comparison of Mammography, Artificial Intelligence, and Supplementary Ultrasound. *AJR Am J Roentgenol.* 2024;222(1):1-12. doi:10.2214/AJR.23.29655.
7. Lee JH, Kim KH, Lee EH, Ahn JS, Ryu JK, Park YM et al. Improving the Performance of Radiologist Using Artificial Intelligence-Based Detection Support Software of Mammography: A Multi-Reader Study. *Korean J Radiol.* 2022;23(5):505-516. doi:10.3348/kjr.2021.0476.
8. Kim HJ, Kim HH, Kim KH, Choi WJ, Chae EY, Shin HJ et al. Mammographically occult breast cancers detected with AI-based diagnosis supporting software: clinical and histopathologic characteristics. *Insights Imaging.* 2022;3(1):57. doi:10.1186/s13244-022-01183-x.
9. Yoon JH, Han K, Suh HJ, Youk JH, Lee SE, Kim EK. Artificial intelligence-based computer-assisted detection/diagnosis (AI-CAD) for screening mammography: Outcomes of AI-CAD in the mammographic interpretation workflow. *Eur J Radiol Open.* 2023;11(11):100509. doi: 10.1016/j.ejro.2023.100509.
10. Dratsch T, Chen X, Rezazade Mehrizi M, Kloeckner R, Mähringer-Kunz A, Püsken M, et al. Automation Bias in Mammography: The Impact of Artificial Intelligence BI-RADS Suggestions on Reader Performance. *Radiology.* 2023;307(4): e222176. doi: 10.1148/radiol.222176.
11. Lamb RL, Lehman CD, Gastouniotti A, Conant EF, Bahl, M. Artificial Intelligence (AI) for Screening Mammography, From the AJR Special Series on AI Applications. *AJR.* 2022;219:369-380. doi: 10.2214/AJR.21.27071.
12. Lunit INSIGHT MMG. <https://www.lunit.io/en/products/mmg>. Accessed February 18, 2024.
13. D'Orsi C, Sickles EA, Mendelson EB, Morris EA. Breast Imaging Reporting and Data System: ACR BI-RADS breast imaging atlas. 5th Edition. Reston: American College of Radiology. 2013.
14. American College of Radiology. ACR BI-RADS Atlas: Breast Imaging Reporting and Data System. 5th. Reston, VA: American College of Radiology; 2013. ACR BI-RADS® - Mammography.
15. Alomaim W, O'Leary D, Ryan J, Rainford L, Evanoff M, Foley S. Variability of Breast Density Classification Between US and UK Radiologists. *J Med Imaging Radiat Sci.* 2019; 50(1):53-61. doi: 10.1016/j.jmir.2018.11.002.

Fallopian tube decidualosis with massive hemoperitoneum in a second-trimester pregnancy: a case report of ultrasound findings

Diana Camorlinga-Ornelas^{1,2}* and David Garza-Cruz³

¹Department of Radiology, High Specialty Medical Unit 71, Mexican Social Security Institute; ²School of Medicine, Autonomous University of Coahuila; ³Diagnostic and Therapeutic Imaging Department, Hospital Angeles, Torreon. Coahuila, Mexico

ABSTRACT

Deciduosis is a decidual reaction outside the uterus that typically occurs during pregnancy. It is usually asymptomatic, but several life-threatening complications have been reported. Imaging features of this condition are lacking. This case report describes the ultrasound and clinical findings in a pathologically confirmed case of decidualosis. A 28-year-old primigravida with 23 weeks of gestation was referred to our department with severe abdominal pain. Pelvic ultrasound showed a left-sided, oval, well-circumscribed, solid, heterogeneous, predominantly hypoechoic pelvic mass without vascularity. There was abundant free fluid in the perihepatic and perisplenic spaces. The patient went into hypovolemic shock, leading to emergency surgery. Active bleeding from the left fallopian tube and a large hemoperitoneum of 1500 ml were found in this area and evacuated. A congestive fallopian tube with an arborescent zone and bleeding near the fimbria was removed. The histopathological features of the left salpingeal mass were consistent with decidual tissue surrounded by a hematoma. This case report is the first in Mexico to emphasize the imaging findings of this entity. It is presented as an educational tool that highlights decidualosis as a potential differential diagnosis in the emergency abdominopelvic ultrasound of pregnant patients.

Keywords: Decidua. Fallopian tube. Pregnancy complications. Ultrasonography. Hemoperitoneum. Case report.

INTRODUCTION

Deciduosis is the presence of an ectopic decidual reaction outside the uterus. It consists of a metaplastic change in submesothelial mesenchymal cells¹ induced by progesterone or progesterone-like substances released by the corpus luteum or adrenal cortex^{2,3}. Deciduosis has been reported at gynecological, gastrointestinal, renal, lymph node, diaphragmatic, surgical scar, and omentum sites^{2,4,5}. The etiology of decidualosis is unclear, and there are two main theories. One is that decidual cells are already outside the uterus, and the other is that the superficial coelomic stroma undergoes metaplasia. The latter is the most widely accepted^{3,5,6}.

Although decidualosis was first described by Walker von Solothurn in 1864⁵, knowledge of the imaging features, particularly ultrasonography, is limited. The available literature provides no specific information, with reported ultrasound findings related primarily to free fluid detection (usually without debris) or bowel distension, particularly in the context of reactive ileus or bowel obstruction due to complications¹. There are no ultrasound diagnostic or prognostic criteria, and histopathological examination remains the gold standard for diagnosis⁵.

Although decidualosis is usually asymptomatic, its clinical manifestations may include abdominal pain, obstructive ileus^{2,4}, hematuria², recurrent pneumothorax, obstructed labor, or hemoperitoneum⁷. The main

*Corresponding author:

Diana Camorlinga-Ornelas
E-mail: dra.camorlinga@gmail.com

Received for publication: 06-04-2024

Accepted for publication: 25-04-2024

DOI: 10.24875/JMEXFRI.24000016

Available online: 10-07-2024

J Mex Fed Radiol Imaging. 2024;3(2):128-131

www.JMeXFRI.com

2696-8444 / © 2024 Federación Mexicana de Radiología e Imagen, A.C. Published by Permanyer. This is an open access article under the CC BY-NC-ND (<https://creativecommons.org/licenses/by-nc-nd/4.0/>).

contribution of imaging in abdominal pain is to rule out other causes of acute abdomen⁸. No specific findings for deciduosis have been described by any imaging method, implying that it could be dismissed due to its similar density to the surrounding tissues⁸. This case report describes the clinical and ultrasound findings in a 28-year-old primigravida with 23 weeks of gestation, severe abdominal pain, and a pathologically confirmed diagnosis of deciduosis.

CASE DESCRIPTION

Our patient was a 28-year-old Caucasian female, gravida 1, para 0, with 23 weeks of pregnancy, referred to the imaging department because of diffuse abdominal pain radiated to the anal region and persistent nausea and vomiting. Before this event, her pregnancy had been carefully screened and was uneventful. Physical examination revealed pallor, drowsiness, stable cardio-pulmonary function, a distended abdomen secondary to pregnancy, and generalized abdominal pain with tenderness, guarding, and a positive rebound sign. Vital signs and laboratory values were normal. She was initially treated with indomethacin for early preterm labor with a poor response. An ultrasound was requested.

Imaging findings

Abdominopelvic and obstetric ultrasounds were performed with an ACUSON Sequoia VA25 SW Ultrasound System (Siemens Medical Solutions, Inc., Mountain View, CA, USA) with a 5-MHz curved transducer. The obstetric ultrasound showed no significant abnormalities (Figure 1). The upper abdominal examination revealed no abnormal findings in the solid organs. Pelvic ultrasound showed a left-sided, oval, well-circumscribed, solid, heterogeneous, predominantly hypoechoic pelvic mass with no vascularity detected on color Doppler examination. Abundant free fluid was noted in the perihepatic and perisplenic spaces and the right lower quadrant (Figures 2 and 3).

Clinical course

The patient eventually presented hypovolemic shock, and an emergency laparotomy was performed. During the procedure, a hemoperitoneum of 1500 ml was evacuated. Active bleeding from the left fallopian tube and a large hematoma were observed; therefore, a left salpingectomy was performed, and hemostasis was achieved. An emergency cesarean section was not required. An arborescent

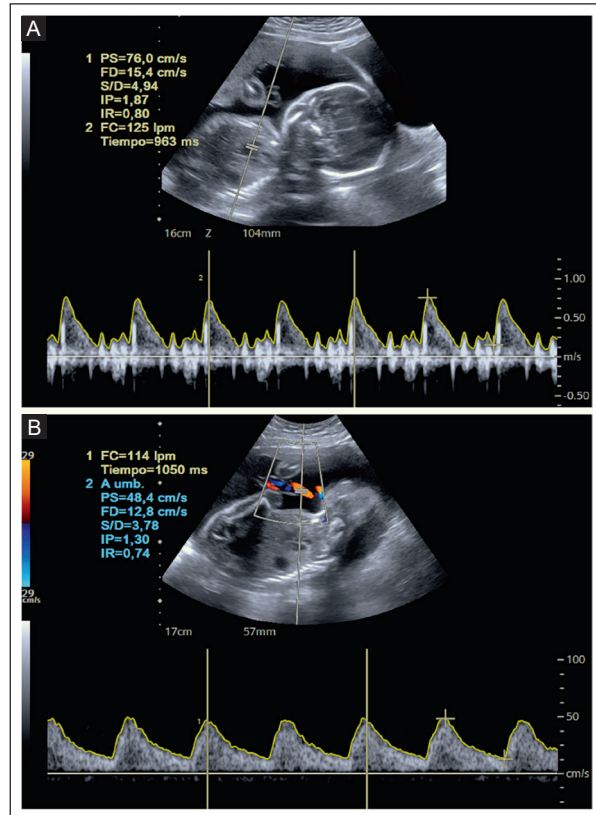


Figure 1. Ultrasound examination of the fetus at 23 weeks gestation. **A:** the fetal heart rate is normal, and the fetus is in a cephalic position. **B:** color Doppler duplex ultrasound image along the umbilical cord showing a typical flow pattern with a pulsatility index in the 46th percentile for gestational age (normal).

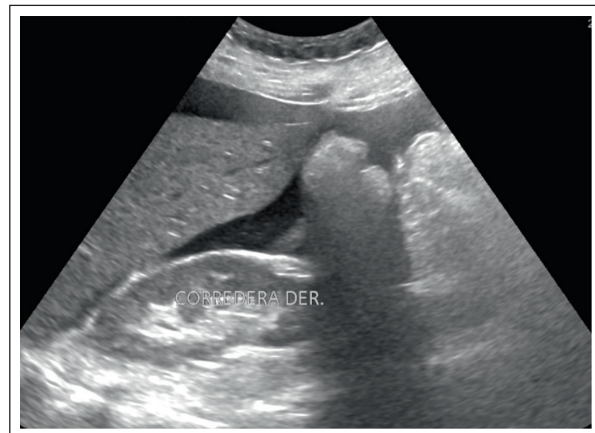


Figure 2. Longitudinal ultrasound of the right upper quadrant of the abdomen in a pregnant 28-year-old female shows abundant free fluid around the liver.

zone and a bleeding area near the fimbria were found on the excised congested fallopian tube. The patient was discharged with an ongoing pregnancy.

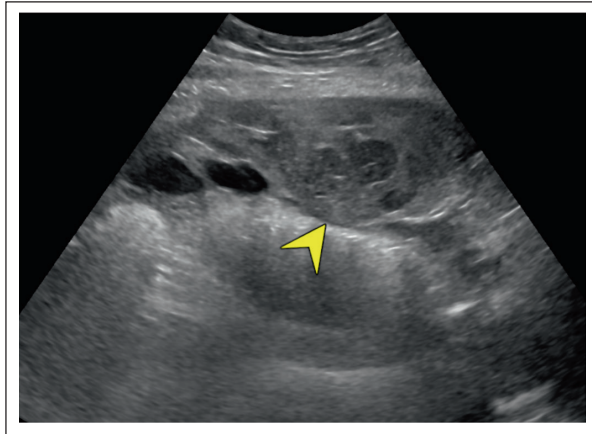


Figure 3. Longitudinal ultrasound of the left flank in a pregnant 28-year-old female shows a left mass adjacent to the uterus (arrowhead). It is oval and well-circumscribed with a predominantly hypoechoic heterogeneous pattern. Color Doppler examination showed no flow (data not shown).

Histopathological findings

The wall and mucosa of the left fallopian tube were undamaged and showed typical histological characteristics. Tissue with a decidual appearance was found on the serosa with extensive areas of fresh hemorrhage alternating with lakes of erythrocytes, fibrin, and polymorphonuclear debris in a diffuse distribution. These findings were consistent with focal peritoneal deciduosis with hemorrhage and acute inflammation (Figure 4).

DISCUSSION

We present the case of a 28-year-old primigravida diagnosed with hemorrhagic salpingeal deciduosis with ultrasound findings of a left, oval, well-circumscribed, predominantly hypoechoic pelvic mass in the left fallopian tube, attributed to a large hematoma with active bleeding and typical histological characteristics. This is the first case report from Mexico of deciduosis localized in the fallopian tube, which is presented for educational purposes to highlight the importance of ultrasound examination.

We found that information on ultrasound findings in deciduosis is lacking in the literature. In four cases documented by Chai *et al.*⁹, three underwent ultrasound examination. Two of these had a nondiagnostic ultrasonography, while the third had a nonspecific mass and free fluid. These findings suggest that ultrasound is of limited use in diagnosing deciduosis or there is a lack of knowledge on the subject. A case report by Jeong *et al.*¹⁰ described an ovarian mass with a heterogeneous

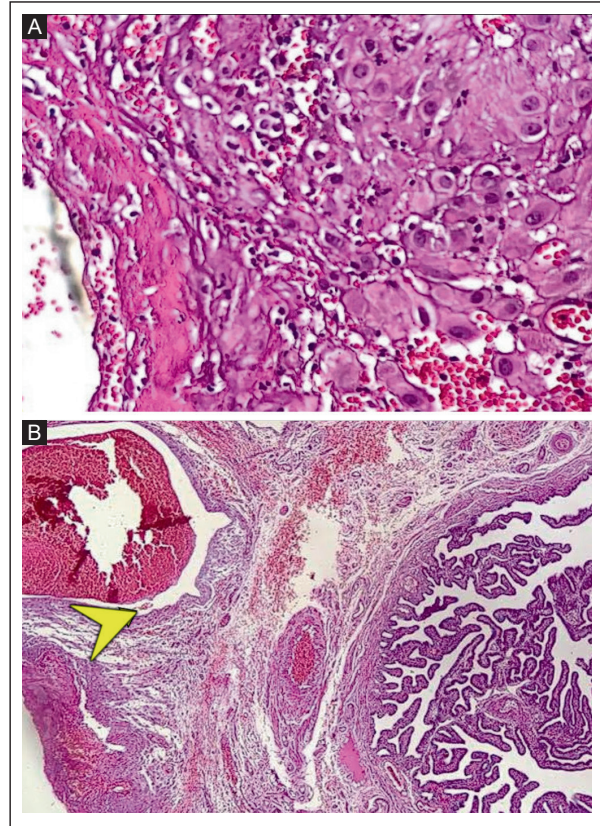


Figure 4. A: a microscopic examination of the resected tissue shows several foci of atypical decidual reaction consisting of a cluster of polygonal cells with abundant homogeneous eosinophilic cytoplasm, large nuclei, and some areas of vacuolar degeneration. No cellular atypia or mitotic areas were detected; hematoxylin and eosin stain 40x. **B:** the adjacent blood vessels are damaged (arrowhead); hematoxylin and eosin stain 10x.

cystic pattern, solid components, and vascularization on Doppler examination. These findings were similar to those of ours. Furthermore, Wong *et al.*¹¹ documented a case of intracystic vegetations in ovarian deciduosis that appeared as a multilocular mass with nodular thickening of its septa and internal vascularization, which are features not identified in our case.

Deciduosis is usually avascular on Doppler examination, although it may show some vascularity, as mentioned in previous cases. Complications can be accompanied by free fluid, especially in case of hemoperitoneum. No additional features, such as calcifications, acoustic shadowing, or lymphadenopathy, have been reported. The reported cases demonstrate the wide variety of findings associated with deciduosis and emphasize the importance of a comprehensive imaging study.

Although specific imaging findings in deciduosis remain elusive, available reports indicate a wide spectrum in size, border definition, sonographic pattern,

echogenicity, and inner characteristics. Our imaging findings are consistent with the literature and showing nonspecific mass features. Some authors report multiple nodules at different sites^{6,7}. They can be isolated or coalescent⁶ and tend to be millimeter-sized nodules but they also occur as large masses⁶ appearing as predominantly cystic and well-circumscribed lesions with vascularity^{6,7}. There is one documented case of a large intrauterine mass consisting of an ectopic decidua with high internal vascularity on Doppler (known as a deciduooma)⁶. We infer a wide spectrum of findings and deciduoosis may present as a single or multiple solid masses¹², localized at any site with submesothelial mesenchymal cells¹, including the salpinges, as in our case.

The symptoms of deciduoosis are non-specific and they mimic other pathologies. Although the clinical course is usually benign, complications such as massive hemoperitoneum can occur, compromising maternal and fetal life. In some cases, emergency surgery may be required. Macroscopically, they appear as whitish-yellow nodules with or without hemorrhagic areas that can be mistaken for carcinomatosis². The final diagnosis of deciduoosis was confirmed by immunohistopathology after surgery in all the reported cases. This tissue must be differentiated from the decidual variant of mesothelioma, metastatic malignant melanoma⁷, carcinomatosis, and granulomas^{1,8}. The main limitation of this report is the lack of immunochemical correlation.

CONCLUSION

The possibility of deciduoosis should be considered for pregnant women with acute abdominal pain and free fluid, especially when other causes of spontaneous hemoperitoneum have been ruled out. A complementary study of the imaging findings with detailed ultrasound descriptions is crucial to increasing our knowledge of this topic. Therefore, this case report serves as a valuable basis for discussion and future research.

Acknowledgments

The authors thank Alexis Zúñiga, MD, Radiologist in Hospital Angeles Torreon, for his help in obtaining representative ultrasound images, and Luis Vitiénez, MD, Department of Pathology, Hospital Angeles Torreon, for his support with pathological data. They also extend their sincere thanks to Professor Ana M. Contreras-Navarro for her guidance in preparing and writing this scientific paper.

Funding

This research received no external funding.

Conflicts of interest

The authors declare no conflicts of interest.

Ethical disclosures

Protection of human and animal subjects. The procedures of this case report were conducted in agreement with the Declaration of Helsinki (1964) and its amendments.

Confidentiality of data. The authors followed the protocols of their work center for the publication of patient data.

Right to privacy and informed consent. Informed consent was not required for this case report of routinely collected clinical data.

Use of artificial intelligence. The authors did not use generative artificial intelligence to prepare this manuscript or create figures or figure legends.

REFERENCES

1. Khajuria R, Sharma S, Singh K, Neelam. Peritoneal Deciduoosis: A Case Report. *JK Science*. 2015;17(2):102-103.
2. Jadhav T, Doshetty R. Deciduoosis in a cesarean scar. *Autops Case Rep*. 2022;12:e2021383. doi: 10.4322/acr.2021.383.
3. Shukla S, Pujani M, Singh SK. Ectopic decidual reaction mimicking peritoneal tubercles: A report of three cases. *Indian J Pathol Microbiol*. 2008;51(4):519-520. doi: 10.4103/0377-4929.43746.
4. Van Diepen DA, Hellebrekers B, van Haften AM, Natté R. Cervical deciduoosis imitating dysplasia. *BMJ Case Rep*. 2015;01-03. doi: 10.1136/bcr-2015-210030.
5. Torres-Ugalde B, Mendoza-Reyes E, Sandoval-Mejía A, Reyes-Hernández MU. Deciduoosis peritoneal que en el embarazo simula carcinomatosis: reporte de caso. *Ginecol Obstet Mex*. 2021;89(9):721-726. Spanish. doi: 10.24245/gom.v89i9.5093.
6. Dasani M, Jeong Lee H, Rijhsinghani A. Deciduooma. A Large Intrauterine Mass of Deciduoosis. *AJP Rep*. 2019;9:e337-e340. doi: 10.1055/s-0039-1697647.
7. Spitale LS, Piccinni DJ, Cabalier LR, Dionisio de Cabalier ME. Deciduoosis peritoneal. Un hallazgo incidental. Poster presentation at IV Congreso Virtual Hispano Americano de Anatomía Patológica; 2000 Dec 1-5. Córdoba, Spain.
8. Sorokin P, Nikiforichin A, Panin A, Zhukov A, Gushchin V, Kurtser M. Diffuse Ectopic Deciduoosis Imitating Peritoneal Carcinomatosis with Acute Abdomen Presentation: A Case Report and Literature Review. *Case Rep Obstet Gynecol*. 2020;8847082:01-08. doi: 10.1155/2020/8847082.
9. Chai D, Wijesuriya R. Deciduoosis of the appendix: diagnostic dilemma continues despite MRI evidence. *Ann R Coll Surg Engl*. 2016;98:e200-e202. doi: 10.1308/rcsann.2016.0242.
10. Kim KH, Nam KY, Kwon JY, Kim YH, Park YW. A case of ovarian deciduoosis in pregnancy. *Korean J Obstet Gynecol*. 2011;54(7):373-376. doi:10.5468/KJOG.2011.54.7.373.
11. Wong L, Botolahy V, Carteret T, Marty M, Brun JL. Decidualized ovarian mass mimicking malignancy. *Case Rep Obstet Gynecol*. 2015;2015: 217367. doi: 10.1155/2015/217367.
12. Lier M, Brosens I, Mijatovic V, Habiba M, Benagiano G. Decidual Bleeding as a Cause of Spontaneous Hemoperitoneum in Pregnancy and Risk of Preterm Birth. *Gynecol Obstet Invest*. 2017;(82):313-321. doi:10.1159/000468933.

The transmante sign: a characteristic MRI finding of focal cortical dysplasia type II

Rebeca de J. Ramos-Sanchez^{ID*}, Jose M. Curiel-Zamudio, and Roger A. Carrillo-Mezo

Neuroimaging Department, Instituto Nacional de Neurología y Neurocirugía “Manuel Velasco Suarez”, Mexico City, Mexico

A 45-year-old man with drug-resistant epilepsy since the age of 3 years was evaluated. He experienced focal onset seizures that progressed to bilateral seizures that occurred up to five times a day. The HARNESS magnetic resonance imaging (MRI) protocol was

performed using SIGNA™ Explorer 1.5T equipment (GE Healthcare, Chicago, IL, USA). A zone of cortical thickening with hyperintensity on T2/FLAIR and hypointensity on T1 was seen in the juxtacortical white matter of the left inferior parietal lobe (Figure 1).

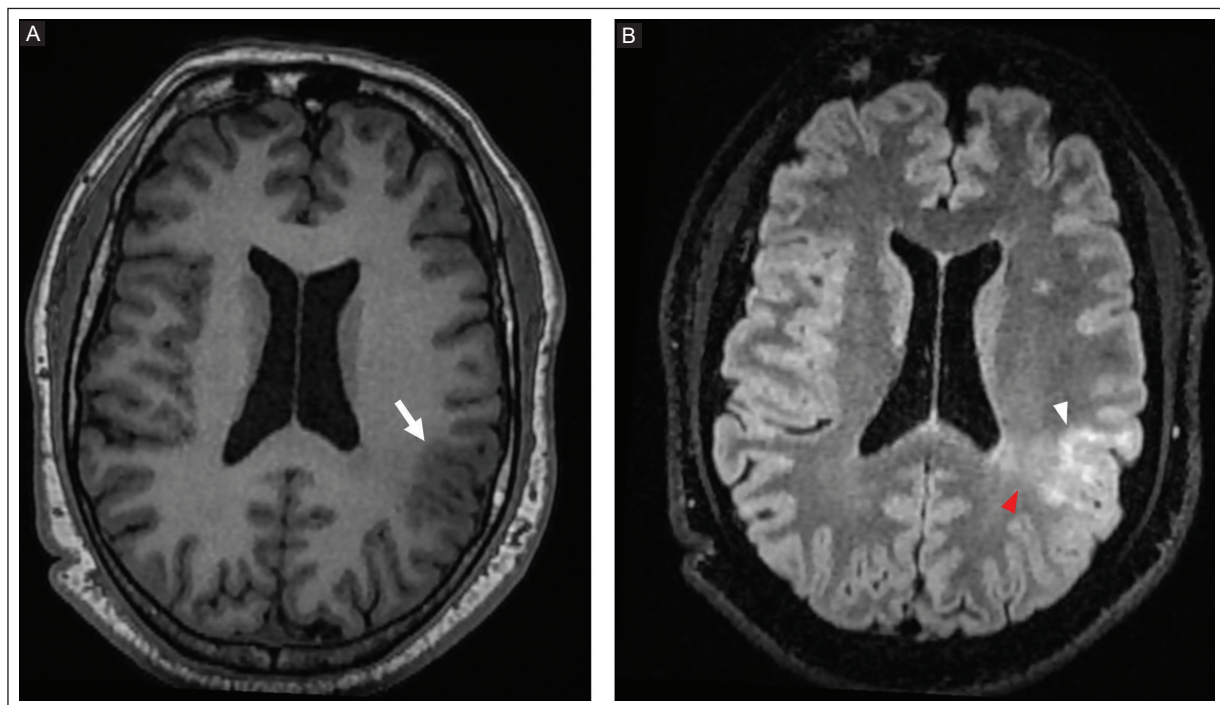


Figure 1. MRI of a 45-year-old man with drug-resistant epilepsy since the age of 3 years, secondary to FCD. **A:** axial T1-weighted with thickening of the left parietal cortex (white arrow). **B:** axial FLAIR showing cortical thickening, diffused cortico-subcortical interface (white arrowhead), and hyperintensity of the subcortical white matter, associated with a triangle-shaped hyperintensity (red arrowhead) extending from the described area to the ependymal surface of the lateral ventricle indicating the transmante sign.

FCD: focal cortical dysplasia; FLAIR: fluid-attenuated inversion recovery; MRI: magnetic resonance imaging.

Corresponding author:

*Rebeca de J. Ramos-Sanchez

E-mail: rramossanchez25@gmail.com

2696-8444 / © 2024 Federación Mexicana de Radiología e Imagen, A.C. Published by Permanyer. This is an open access article under the CC BY-NC-ND (<https://creativecommons.org/licenses/by-nc-nd/4.0/>).

Received for publication: 20-10-2023

Accepted for publication: 13-04-2024

DOI: 10.24875/JMEXFRI.23000022

Available online: 10-07-2024

J Mex Fed Radiol Imaging. 2024;3(2):132-133

www.JMeXFRI.com

This observation indicated a loss of the gray–white matter interface, which was consistent with focal cortical dysplasia (FCD). A triangle-shaped area was found to be extended from the affected cortex to the lateral ventricle on the same side, indicating the presence of the transmantle sign.

FCD is a localized cerebral cortical malformation associated with drug-resistant focal epilepsy¹. Typical MRI features of FCD include blurring in the gray and white matters, cortical thickening, white matter hypointensity in T1WI, and hyperintensity in T2WI and FLAIR². The transmantle sign is present when white matter hyperintensity covers the cerebral mantle from the ventricle to the cortical surface. This sign is a distinctive imaging marker for FCD type II and is particularly evident in FLAIR sequences³.

Funding

This study received no external funding.

Conflicts of interest

The authors declare no conflicts of interest.

Ethical disclosures

Protection of individuals. This study complied with the Declaration of Helsinki (1964) and subsequent amendments.

Data confidentiality. The authors declare that they followed their center’s protocol for sharing patient data.

Right to privacy and informed consent. Informed consent was not required to analyze and publish routinely acquired clinical data.

Use of artificial intelligence. The authors state that they did not use generative artificial intelligence in preparing this manuscript or creating figures or figure legends.

REFERENCES

1. Kimura Y, Shioya A, Saito Y, Oitani Y, Shigemoto Y, Morimoto E, et al. Radiologic and Pathologic Features of the Transmantle Sign in Focal Cortical Dysplasia: The T1 Signal Is Useful for Differentiating Subtypes. *AJNR Am J Neuroradiol.* 2019;40(6):1060-1066. doi: 10.3174/ajnr.A6067.
2. Mellerio C, Labeyrie MA, Chassoux F, Dumas-Duport C, Landre E, Turak B, et al. Optimizing MR imaging detection of type 2 focal cortical dysplasia: best criteria for clinical practice. *AJNR Am J Neuroradiol.* 2012;33(10):1932-1938. doi: 10.3174/ajnr.A3081.
3. Kokkinos V, Kallifatidis A, Kapsalaki EZ, Papanikolaou N, Garganis K. Thin isotropic FLAIR MR images at 1.5T increase the yield of focal cortical dysplasia transmantle sign detection in frontal lobe epilepsy. *Epilepsy Res.* 2017;132:1-7. doi: 10.1016/j.epilepsyres.2017.02.018.